STUDY OF COLD-MASS SUPPORT SYSTEM OF SUPERCONDUCTING MAGNETS FOR ACCELERATOR APPLICATIONS

By
ANJAN DUTTA GUPTA
Enrolment No. ENGG04201104001

Variable Energy Cyclotron Centre, Kolkata

A thesis submitted to the
Board of Studies in Engineering Sciences
In partial fulfillment of requirements
for the Degree of

DOCTOR OF PHILOSOPHY

of

HOMI BHABHA NATIONAL INSTITUTE

August, 2018

Homi Bhabha National Institute[1]

Recommendations of the Viva Voce Committee

As members of the Viva Voce Committee, we certify that we have read the dissertation prepared by Anjan Dutta Gupta entitled "Study of cold-mass support system of superconducting magnets for accelerator applications" and recommend that it may be accepted as fulfilling the thesis requirement for the award of Degree of Doctor of Philosophy.

Alok Chakrabarti	08-08-2018
Chairman – Prof. Alok Chakraborti	**Date:**
P. Mukherjee	08/08/18
Guide / Convener – Prof. Paramita Mukherjee	**Date:**
Swarnendu Sen	8/8/18
Co-guide – Prof. Swarnendu Sen (JU)	**Date:**
V. Vasudeva Rao	8/8/2018
Examiner – Prof. V. Vasudeva Rao (IIT-KGP)	**Date:**
Indranil Das	8/8/2018
Member 1- Prof. Indranil Das (SINP)	**Date:**
	13/08/2018
Member 2- Prof. M.K. Mitra (JU)	**Date:**

Final approval and acceptance of this thesis is contingent upon the candidate's submission of the final copies of the thesis to HBNI.

I/We hereby certify that I/we have read this thesis prepared under my/our direction and recommend that it may be accepted as fulfilling the thesis requirement.

Date: 8/8/18

Place: Kolkata

Swarnendu Sen
Co-guide

P. Mukherjee
Guide

[1] This page is to be included only for final submission after successful completion of viva voce.

STATEMENT BY AUTHOR

This dissertation has been submitted in partial fulfillment of requirements for an advanced degree at Homi Bhabha National Institute (HBNI) and is deposited in the Library to be made available to borrowers under rules of the HBNI.

Brief quotations from this dissertation are allowable without special permission, provided that accurate acknowledgment of source is made. Requests for permission for extended quotation from or reproduction of this manuscript in whole or in part may be granted by the Competent Authority of HBNI when in his or her judgment the proposed use of the material is in the interests of scholarship. In all other instances, however, permission must be obtained from the author.

ANJAN DUTTA GUPTA

DECLARATION

I, hereby declare that the investigation presented in the thesis has been carried out by me. The work is original and has not been submitted earlier as a whole or in part for a degree / diploma at this or any other Institution / University.

Anjan Dutta Gupta

ANJAN DUTTA GUPTA

List of Publications arising from the thesis

Journal

1. "Optimization of Support System for FAIR Energy Buncher Dipole Magnet", Anjan Dutta Gupta, Sundeep Ghosh, Pranab Bhattacharyya, Gautam Pal, Paramita Mukherjee, and Swarnendu Sen, *IEEE Transactions on Applied Superconductivity*, **2016**, *Vol. 26*, pp. 4900505.

2. "Proton Irradiation Study on pure Ti and Ti-6Al-4V", A. Dutta Gupta, P. Mukherjee, N. Gayathri, P. Bhattacharyya, M. Bhattacharya, Apu Sarkar, S. Sen, M.K. Mitra, *Nuclear Instruments and Methods in Physics Research B*, **2016,** *Vol. 387*, pp. 63-72.

3. "Cryostat Suspension System Analysis during Cool-Down and its Validation", Subrata Saha, Anjan Dutta Gupta & Manir Ahammed, *Journal of the Institution of Engineers (Indian): Series C (Springer)*, **2017**, *Vol. 98, No. 2*, pp. 179-184

Conferences

1. "Design of Magnets for Energy Buncher of FAIR project", Anjan Dutta Gupta, P.R. Sharma, Chinmay Nandi, Subrata Saha, *Theme Meeting on Unveiling Future with Cyclotrons*, **2012**.
2. "Irradiation Effects on Ti and Ti-alloys characterized by XRD techniques", A Dutta Gupta, S. Roychoudhury, P.Bhattacharya, N.Gayathri, S.Sen, M.K.Mitra and P.Mukherjee, *National Conference on Current Trends in Advanced Materials (CTMat-2014)*, **2014**.
3. "Development of Large Aperture Superferric Magnets for Energy Buncher of FAIR", *DAE-BRNS Workshop on Superconductivity and its Application in Electrical Systems (SAES-2015)*, **2015**.

ANJAN DUTTA GUPTA

DEDICATIONS

Dedicated to my mother, Malati Dutta Gupta

ACKNOWLEDGMENTS

I would like to express my heartiest gratitude to Dr. Paramita Mukherjee, my supervisor, for her continuous support, guidance, and persuasion to the work. I also express my sincere gratitude to Prof. Swarnendu Sen for his direction with the analysis work. My sincere thanks go to Prof. M.K. Mitra, JU for his help throughout the tenure of this work. I am indebted to all members of the team involved in building the superconducting cyclotron at VECC. Measurements presented in the thesis would not have been possible without the contribution from my colleagues of Accelerator Physics Group, Mechanical Engineering Group, Accelerator Technology Group and Computer & Information Group. I am grateful to all the members of the Mechanical Engineering Group, VECC for their cooperation and help during data taking. Special thanks go to Shri Tamal K. Bhattacharyya, who made the MMI of the Cryogen Delivery System that monitors the support link forces. The scientific discussion with my colleagues, Shri Subrata Saha and Shri Sundeep Ghosh, helped me a lot and special thanks go to them. Thanks to Shri Pranab Bhattacharyya for always reminding me about the deadlines during this work. I sincerely thank the operational staffs of the *K*130 cyclotron for their help during the irradiation of samples. I'm indebted to Dr. Gaythri N. Banerjee for helping in the irradiation of samples, taking XRD data and analysis. I'm also grateful to Dr. Tapati Kundu Roy for helping with the micro-hardness measurement. My sincere thanks go to Shri Jayanta Chaudhuri and Shri Gautam Pal for allowing me for this work and encouraging me with the publications. I would also like to thank Dr. J. Pradhan and Dr. N.K. Das for their encouragement and help with the editing. I'm thankful to the Chairman and Members of the Doctoral Committee for their review in every stage of the work, suggestions, and encouragement given during the tenure of this work. My sincere thanks to the Ex-Directors of this Centre, Dr. R.K. Bhandari, Dr. D.K. Srivastava and present Director, Shri A. Roy for their inspiration. Finally, I thank my wife, Debasmita for her constant support and encouragement that helped me in completing my thesis.

Contents

List of abbreviations

AFC	Absorber Focus Coil
APDL	ANSYS Parametric Design Language
ATLAS	A Toroidal LHC ApparatuS
BESIII	Beijing Spectrometer III
BigRIPS	In-flight RI beam separator at RIKEN
CFRP	Carbon Fiber Reinforced Plastic
CG	Center of Gravity
CMS	Compact Muon Solenoid
EBSD	Electron Backscatter Diffraction
ELI	Extra Low Interstitials
FAIR	Facility for Antiproton and Ion Research
FEM	Finite Element Methods
FE-SEM	Field Emission Scanning Electron Microscope
GFRP	Glass Fiber Reinforced Plastic
HCP	Hexagonal Close Packed
HERA	Hadron-Electron Ring Accelerator
HISS	Heavy Ion Superconducting Spectrometer
IHEP	Institute of High Energy Physics
IPF	Inverse Pole Figure
ISABELLE	Intersecting Storage Accelerator + "belle"
LHC	Large Hadron Collider
MAUD	Material Analysis Using Diffraction
MICE	Muon Ionization Cooling Experiment
MRI	Magnetic Resonance Imaging
MSU	Michigan State University
NSCL	National Superconducting Cyclotron Laboratory
PODS	Passive Orbital Disconnect Struts
RHIC	Relativistic Heavy Ion Collider
RIA	Rare Isotope Accelerator
RIS	Radiation-Induced Segregation

SMES	Superconducting Magnetic Energy Storage
SNS	Spallation Neutron Source
SQUID	Superconducting Quantum Interference Devices
SRIM	Stopping and Range of Ions in Matter
SSC	Superconducting Super Collider
SST-1	Steady-state Superconducting Tokamak
Super-FRS	Super-Fragment Separator
TF	Toroidal Field
Tokamak	Transliteration of the Russian word - Toridal chamber with magnetic coils
UDM	Uniform Deformation Model
VECC	Variable Energy Cyclotron Centre
XRD	X-ray Diffraction
XRDLPA	X-Ray Diffraction Line Profile Analysis

Synopsis

Superconducting magnets are used in the devices like accelerators, Tokamaks, Magnetic Resonance Imaging (MRI), etc. for producing high magnetic field. High energy accelerators use superconducting magnets to their advantage for bending or resolving charge particle beams. Superconducting magnets have several advantages over the resistive magnets owing to their capacity for producing a high magnetic field in compact size and less weight. The high magnetic field is created using the superconducting properties of the conductor at cryogenic temperature, mostly at 4 K.

In superconducting magnets, in general, the coils are placed inside a helium chamber and suspended from the outer vacuum chamber using supports. The helium chamber along with the coil is called as cold-mass of the magnet. The design of the cold-mass support system of the magnet needs to consider two essential requirements; firstly, it is to be made of high strength material with a high cross-section. Secondly, it must conduct less heat load to the coil, which requires materials with low thermal conductivity with a lesser cross-section. It is therefore needed to optimize the design of the support system under thermal and magnetic loadings to choose the right cross-section and stiffness of the support. The support system for large superconducting magnets, required for spectrometry, also needs to provide excellent alignment of the coils with respect to the yoke after cool-down and magnet energization to achieve high magnetic field accuracies.

The superconducting magnets use various kinds of support systems, starting from support links, tie-rods, support posts, etc. and use varied materials of supports to fulfill the requirements of the individual magnets. In general, the supports can be divided into two categories, one that takes axial load only, like links, tie-rods and the other one that takes the axial load as well as moments, like support posts.

Diverse types of support systems are used for superconducting magnets to suspend the cold-mass, i.e., coil and its former, inside the outer vacuum chamber. Several authors have reported about several types of supports designed for the superconducting magnets. Niemann et al. [1] presented tension member supports made of epoxy-fiberglass for superconducting magnet and discussed on the minimization of heat leak to the magnet cold-mass [1]. Kai Zhang et al. reported about the cold-mass support structure made of CFRP tie rods for MRI superconducting magnet and conductive heat leak, structure strength and mechanical vibration properties were discussed [2]. The alternate design concept for the SSC dipole magnet cryogenic support post shows a reentrant post design to meet the structural and thermal requirements and reduce the overall cost [3].

Cold-mass is supported by several supports to restrain its movement during cool-down and energization. The support system provides stability against magnetic force in the expense of small conduction heat load to the helium. Large superconducting magnets, like MICE AFC magnets [4] and dipole magnets of Energy Buncher of the FAIR Super-FRS [5], are also required to have excellent alignment of the coils. MICE magnets are designed to have self-centered supports [6].

Self-centered supports are possible with the symmetrical magnets like solenoids. In many cases, the coils are unsymmetrical structure, e.g., superconducting spectrometer magnets [7], [8] and the supports need to be designed to minimize the coil movement [9].

The primary objective of this thesis is to study in detail the entire support structure analytically. The analysis includes temperature dependent thermal properties. The analysis of the system also considers the Lorentz forces on the coil that are dependent on the coil current and the force due to the interaction of the coil with an iron yoke that varies with the coil shift. As a result, the stress developed in the support system and the coil positions both changes with the increase of current and both are a function of the current in the coil. The primary focus of this study is to find out design methodology of link type of support system for superconducting dipole and solenoid magnets considering all the possible loadings.

Chapter 1 starts with the general introduction of the support structure, description of various kinds of support structures being used by the superconducting magnets and objective of this study in details.

Chapter 2 deals with the link type support systems for superconducting dipole magnets for predicting the support stresses and coil movement under thermal as well as magnetic loading. An analytical model was developed considering the thermal load on the coil and support system and combined with the effect of magnetic force. The model assumes that the thermal and magnetic effects can be superimposed if the stresses are within the elastic limit. The coil and the support links together were modeled for the equilibrium of forces and deformation. Since the system of equations is indeterminate, deformation equations were needed for finding out the support stresses and deformations. Castigliano's theorem was applied for finding out the stiffness of the system and used in the equations. All the equilibrium equations were solved numerically for finding out the support forces, stresses, and coil position after cool-down and energization. It was found that the support stresses and the movement of the coil can be predicted from this analysis.

Movement of the coil takes place due to the following reasons:

(a) Due to differential thermal contraction, if any asymmetry in the coil or support system geometry is present

(b) Due to the action of magnetic force

Since the magnetic force is dependent on the position of the coil within the iron yoke, it is also possible that any movement of the coil results in higher magnetic force resulting continuous movement of the coil towards the direction of the magnetic force if support system design does not offer enough stiffness against it. The movement of the coil may result in complete instability and coil movement under magnetic force and may lead to failure of the support system. This analytical method could also determine the region of the instability of the coil and support system and was able to predict the minimum support stiffness required to restrict the uncontrollable movement of the coil.

Higher stiffness of the support system, in general, causes in less movement of the coil but higher heat load due to conduction. This analytical study suggests the way to find out the most suitable values of support stiffness that ensures both the desired conditions – less movement of the coil and less conduction heat load.

Two generalized magnet geometries - bending and solenoid magnets were studied. The FAIR Energy Buncher Dipole solenoid magnet geometry was taken as an example for dipole magnet, and the study is presented in Chapter 2.

Chapter 3 extended the study to the solenoid magnets and detailed the movement of the coil further. The analytical methodology to find the effect of thermal and magnetic forces on the coil and the support structure have been described in detail in this chapter. It has been found out that the coil shift will happen for K500 superconducting cyclotron after the cool-down due to asymmetry in its support system. The superconducting magnets not only require stability of its support structure but also needs centering of the coil with respect to its iron core to achieve the desired magnetic field shape and accuracies at different excitations of the magnet. As an example, the FAIR Energy Buncher dipole magnets need an accuracy of placement of the coil by ± 1 mm to achieve the desired magnetic field accuracy. The coil centering is also crucial for the high field solenoid magnets like superconducting cyclotron magnet at VECC so that the support links do not break during the energization of the magnet. The coil centering is thus an essential part of the design of the magnets as well as an important activity during the first energization of the magnet. It has been seen that the coil centering is greatly influenced by the coil, iron yoke and the support system geometry. A simple model of a high field solenoid magnet was made, and resultant force on the coil was found out analytically as a function of current in the coil and its radial position with respect to the iron yoke. The image-current method was used to approximate the effect of the iron yoke and the magnetic force as a function of current and its radial position was calculated. It was seen that the magnetic force was directly proportional to the square of the coil current and the radial displacement of the coil from the iron central axis. The support links for K500 superconducting cyclotron are equipped with load sensing studs to measure the cool-down force as well as the magnetic force on the coil. The resultant of all the support system force is the reaction force against the consequent thermal and magnetic force.

Detailed theoretical and experimental study has been carried out to find the coil shift during cool-down of the magnet coil and energization of the magnet. The coil centering is conventionally done using a trial-error method measuring [10] the support forces during the first energization of the magnet. The reason behind is that the magnetic stiffness is a strong current dependent parameter and is not known beforehand during coil centering. This study aimed to calculate the resultant forces of the support system under magnetic loading for coil shift. The method described here may be used for reducing the steps of the trial error method and center the coil using the measured force data from the support system. The methodology was applied for the superconducting cyclotron magnet at Variable Energy Cyclotron Centre, and the results are compared with the experimental data measured during the coil centering. It has been seen that the coil shift predicted by this analysis is not in good agreement with the physical movement given to the coil. This disagreement may be attributed to the fact that the given displacement of support links may not have translated to the same movement of the coil.

The materials of the support systems, when used in the accelerators, likely to undergo irradiation damage over the years (25-30 years lifetime of the accelerator) by the neutron-induced activity. It has been seen that the designers of superconducting magnets have used Ti and its alloys (Ti, Ti-6Al-4V and Ti-5Al-2.5V) due to their high strength to thermal conductivity ratio [11]. It is therefore required to study the effect of irradiation on the microstructure which primarily governs the mechanical properties of these support structure as they will be used in the accelerators during its lifetime of operation. **Chapter-4** describes in detail the irradiation study experiment and the results of X-ray diffraction line profile analysis [12]. Post irradiated microstructural characterization study on pure Ti and Ti-6Al-4V materials have been carried out as a function of dose using different model-based techniques of X-ray diffraction line profile analysis (XRDLPA). This study shows that Ti-6Al-4V can be considered as radiation resistant for applications to the support structure of magnets for accelerators during its lifetime.

The thesis concludes in **Chapter 5** with a note that the analytical methodology described here could be a useful tool for the design and optimization of support systems in general and particularly for link type of support system. It has also made it clear that the Ti-6Al-4V is a suitable candidate alloy from the point of irradiation damage in accelerator applications.

Bibliography

[1] R.C. Niemann, J.D. Gonczy, K.F. Mataya and P. Smelser, "An epoxy fiberglass tension member support for superconducting magnet," Advances in Cryogenic Engineering, vol. 24, pp. 283-289, 1978.

[2] Kai Zhang, Zian Zhu, Ling Zhao, Zhilong Hou, Meifen Wang, Guoquing Zhang, Weichao Yao, Feipeng Ning, Zhoujie Wang, and Xiaotao Zhang, "Cold-mass Support Structure Design of MRI Superconducting Magnet Developed by IHEP," IEEE Transactions on Applied Superconductivity, vol. 25, No. 2, April 2015.

[3] A. Lipiski, T.H. Nicol, R. Richardson, “Alternative design concept for the SSC dipole magnet cryogenic support post,” Supercollider 3, pp. 301 – 312, 1991.
[4] S.Q. Yang, M.A. Green, W.W. Lau, R.S. Senanayake, B. Strauss, and H. Witte, “The Cold-mass Support System and the Helium Cooling System for the MICE Focusing Solenoid,” IEEE Transactions on Applied Superconductivity, vol. 17, No. 2, 2006, LBNL-61384.
[5] R. K. Bhandari, M. Ahammed, P. Bhattacharya, S. Bhattacharya, S. Chattopadhyay, T. K. Bhattacharya, U. Bhunia, J. Chaudhuri, M. K. Dey, A. Dutta, A. Dutta Gupta, C. Mallik, B. Mandal, B. Manna, C. Nandi, G. Pal, S. Roy, S. Saha and P. R. Sarma, (10 March 2011), “Superconducting magnets for Energy Buncher at FAIR,” Current Science, [Online], vol. 100 (5), pp. 674-681, Available: http://www.currentscience.ac.in/Volumes/ 100/05/0674.pdf
[6] H. Wu, X.K. Liu, L. Wang, S.Y. Li, X.L. Guo, H. Pan, F.Y. Xu and M.A. Green, “Structural design and analysis for a double-band cold-mass support of MICE coupling magnet,” Advances in Cryogenic Engineering, vol. 55. MICE Note 277, 2010.
[7] A.F. Zeller, J.C. DeKamp, J. Wagner, D. Capelli, “Construction and testing of superferric dipoles for the A1900 Fragment Separator,” IEEE Transaction of Applied Superconductivity, vol. 04, 2001, DOI: 10.1109/77.920116
[8] P.R. Sarma, A. Dutta Gupta, C. Nandi, S. Chattopadhyay, G. Pal. 21 November, “Unconventional Purcell filter in superferric magnets in the Facility for Antiproton and Ion Research,” Nuclear Instruments and Methods in Physics Research Section A: Accelerators, Spectrometers, Detectors and Associated Equipment, vol. 729. pp. 718-724, 2013
[9] L. Wang, H. Wu, S.Y. Li, X.L. Guo, H. Pan, S.X. Zheng, M.A. Green, (August 2010), “Design and Analysis of a Self-centered Cold-mass Support for MICE Coupling Magnet,” MICE Note 0344, [Online], August 2010. 5LPD-02, Available: mice.iit.edu/micenotes/public/pdf/MICE0344/MICE0344.pdf.
[10] M. K. Dey, A. Dutta Gupta, J. Debnath, J. Pradhan, A. Dutta, S. Saha, M. Ahammed, P. Bhattacharjee, U. Bhunia, Z. Naser, S. Paul, J. Chaudhuri, C. Mallik and R.K.Bhandari, “Coil Centering of the Kolkata Superconducting Cyclotron

Magnet," in Proceedings of Eighteenth International Conference on Cyclotrons and Their Applications, 2007, pp. 438-440, 2007

[11] The Titanium Information Group, "DATA SHEET No 1: Titanium Alloy Ti-6Al-4V High Stress Applications in Sea Water," [Online], Available: http://www.titaniuminfogroup.co.uk/

[12] P. Mukherjee, A. Sarkar, P. Barat, S. Bandyopadhyay, P. Sen and S. Chattopadhyay, *Acta Mater.,* vol. 52, pp. 5687-5696, 2004.

Keywords

Superconducting magnets, cold mass, support system, accelerator magnets, coil centering.

List of variables

B_{max}	The maximum magnetic field at the center
F_m	Resultant magnetic force
T	Temperature in Kelvin
ΔT	The difference of coil operating temperature and room temperature
R_{H1}	Horizontal reaction force on XZ plane at point B
R_{H2}	Horizontal reaction force on XZ plane at point A
R_V	Vertical reaction force on XY plane
$\alpha_b(T)$	Temperature-dependent linear thermal contraction coefficient of the helium chamber material
$K_{1,2}$	System stiffness of the coil and support for a force applied on support #1, support #2
K_s	Support stiffness
$\theta_{1,2}$	The angle of support #1 (or support #2) with respect to X-axis
θ	The half angle between the legs of the trapezoid coil
a	Length of smaller base of trapezoid coil
b	Length of longer base of trapezoid coil
c	Length of one leg of trapezoid coil
L_s	Length of one support
A_b	Cross-sectional area of helium chamber
E_b	Young's Modulus of material of helium chamber/coil
A_s	Cross-sectional area of support link
E_s	Young's Modulus of material of support link
$\overrightarrow{P_t}$	Coil shift (in X-direction) due to thermal load
x_t	Magnitude of coil shift in X-direction due to thermal load
$F_{1,2}$	Force in support #1 (support #2) due to thermal contraction
F_v	Force in vertical support due to thermal contraction
α	Angle of support #1 with respect to X-axis after cooldown
β	Angle of support #2 with respect to X-axis after cooldown
$\alpha_s(T)$	Temperature-dependent linear thermal contraction coefficient of support material
H	Height of helium chamber from symmetry plane (XY plane)
$\overrightarrow{L_{11}}$	Vector between points D′ and G
$\overrightarrow{L_{22}}$	Vector between points E′ and F

$\overrightarrow{P_m}$	Coil shift due to magnetic force
x_m	Magnitude of coil shift due to magnetic force
F_1'	Force in support #1 due to magnetic force
F_2'	Force in support #2 due to magnetic force
$\overrightarrow{L_1}$	Vector lengths of the support #1 after cool-down
$\overrightarrow{L_2}$	Vector lengths of the support #2 after cool-down
T_o	Operating temperature of coil and helium chamber
$S_{1,2}$	Stress in support #1 (or support #2)
x_f	Total magnitude of coil shift including shift due to thermal contraction and magnetic force
$K(T)$	Temperature-dependent thermal conductivity of the support material
Q	Heat in-leak through a support
x_i	Initial positioning error of the coil
w	Lorentz force acting on coil
F_{mv}	Resultant vertical magnetic force
F_{mr}	Resultant radial magnetic force
L_i	Length of support from coil end to the thermal intercept
L_o	Length of support from the thermal intercept to the room temperature end
T_a	Support temperature at ambient end
T_b	Support temperature at bobbin end
T_n	Support temperature at thermal intercept point
ΔL_k	Thermal contraction of the length of the k^{th} support link due to decrease in temperature
$T_{L_i}(x)$	Temperature of support at any point x in-between length L_i
$T_{L_o}(x)$	Temperature of support at any point x in-between length L_o
R_b	Mean radius of bobbin
H_b	Height of bobbin
ΔR_b	Contraction of mean radius of bobbin due to cool-down
ΔH_b	Contraction of height of bobbin due to cool-down
$\Delta L_k'$	Change of k^{th} support link length due to thermal force
F_k	Reaction force in k^{th} support
L_k	Length of k^{th} support
A_{sk}	Cross-sectional area of k^{th} support
$\Delta R_b'$	Change in bobbin mean radius due to thermal force

K_b	Stiffness of bobbin against support link force
I_b	Moment of inertia of bobbin cross-section
α	Angle between support #2 and #3
β	Angle between support #3 and #1
γ	Angle between support #1 and #2
d	Solenoid coil shift due to cool-down
ϕ	Direction of coil shift due to cool-down
mg	Weight of coil and bobbin
$F_k(T)$	Fitting equation of reaction force in k^{th} horizontal support as a function of cooldown temperature
$\overrightarrow{J_\theta}$	Coil current density
$\overrightarrow{B_z}$	Magnetic field in Z-direction
a_p	Pole radius
N	Number of turn in coil
I	Current in the coil
$\overrightarrow{M_c}$	Dipole moment of coil
$\vec{M}$	Dipole moment of image coil
r	Radius of position of image coil
$\overrightarrow{B_{r,\theta,\phi}}$	Radial or azimuthal or spherical component of magnetic field
$F_{L,R}$	Magnetic force on left -side (or right-side) image coil
Δr	Coil shift due to magnetic force
w	Net Lorentz force acting on a coil cross-section per unit perimeter of the coil
$F_{7,8,9}$	Magnitude of reaction force of horizontal link #7(or link #8 or link #9) against magnetic force
ΔR	Radial expansion of coil and bobbin under Lorentz Force
θ	Direction of net radial magnetic force acting on the coil
$K_{7,8,9}$	Stiffness of support #7, #8, #9
U^*	Complimentary potential energy of the system
δ	Deformation of the system
HV	Vickers pyramid number
F	Applied force in hardness measurement in kgf
d	Average value of diagonals of the impression of the indenter
d_1, d_2	Two diagonals of the impression of indenter
ω	Full Width at Half Maxima of the XRD peak

β	Integral breadth of the XRD peak
ϕ	Shape factor of Voigt function
D_v	Volume weighted domain size
ϵ	Microstrain
λ	Wavelength of CuK_α
β_c	Cauchy component of the integral breadth
β_G	Gauss component of the integral breadth
2θ	Diffraction angle
$\langle \varepsilon_L^2 \rangle^{1/2}$	r.m.s. microstrain
P	Preferred orientation parameter
M_2 (q)	Second order restricted moments of a single XRD peak in q-space
M_4 (q)	Fourth order restricted moments of a single XRD peak in q-space
D_s	Average column length or area weighted domain size measured in the direction of the diffraction vector
L	Taper parameter
K	Scherrer constant
$\langle \rho \rangle$	Average dislocation density
$\langle \rho^2 \rangle$	Average of the square of the dislocation density
q_0, q_1	Fitting parameters in MAUD programme
Λ	Geometrical constant describing the strength of the dislocation contrast

List of Figures

List of tables

Chapter 1
Introduction

Chapter 1

1. Introduction

1.1 Historical survey

In a superconducting state, some materials show no electrical resistance against direct current (DC), i.e., $R_{DC} = 0$. Critical temperature (T_c), critical magnetic field (H_c) and critical current density (J_c) define a critical surface, below which the superconducting state of a material can exist [Figure 1.1].

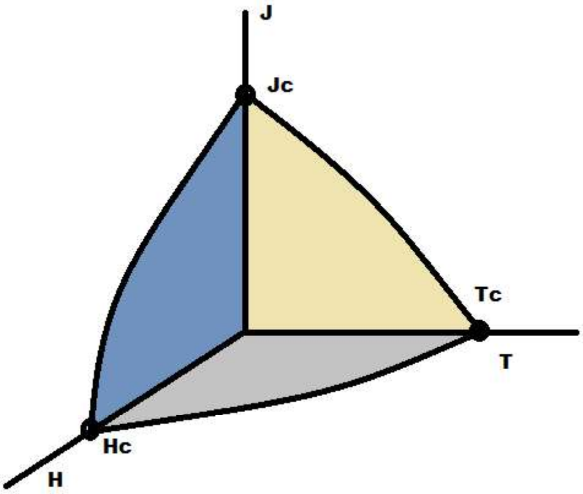

Figure 1.1 The critical surface of a typical superconducting material. Distinct color planes show the variation of any two parameters when the other one is zero.

This property of the materials is used in different applications, like motors, generators, transformers, ultrasensitive magnetic field sensor (SQUIDs), magnetic resonance imaging (MRI), high field magnets for accelerators & detectors, etc. These materials also show very low resistance against alternating currents (AC) and thus suitable for radio-frequency (RF) cavities of very high frequencies (GHz).

The superconductivity, discovered by K.H. Onnes in 1911 [1], made people think about the possibility of very high field magnets. Since then, it took a long time to realize the superconducting magnet technology till the discovery of superconducting materials that could reach large current densities at high magnetic fields. With the development of Nb_3Sn in 1961 and NbTi materials in 1962, the construction of high field superconducting magnets became viable [2]. Towards the end of 1970, superconducting magnet technology took off [2].

Superconducting magnets have several advantages over the resistive magnets owing to their capacity for producing a high magnetic field in compact size and less weight. They can generate magnetic fields that are much stronger (~20 T) than the iron core magnets, which are limited to a magnetic field of less than 2 T. Moreover, they consume less power compared to resistive magnets. They can also fit into smaller space due to the high current density of the superconductors (>100 times than that of resistive windings).

High field magnets (> 2T) are preferred to be superconducting not only owing to low operational cost than resistive magnets, but also for its compactness, for instance, SMES magnet, large accelerator magnets, and so on. However, many medium field magnets are also designed superconducting to take the advantages of their compactness for many applications, such as MRI magnets, accelerator magnets, etc. Superconducting magnets can also be designed to produce homogenous magnetic fields. Spectrometer magnets, MRI magnets, ion-trap magnets, etc. use this to their advantage.

The high magnetic field is produced using the superconducting properties of the conductor (to allow high current density under high magnetic fields) at a cryogenic temperature of around 4.2 K. High energy Particle accelerators use superconducting magnets to their advantage for bending or resolving charge particle beams. The first demonstration of the use and operability of large scale superconducting magnets for accelerators was seen in Tevatron [2], a synchrotron that accelerated proton and antiprotons to 1 TeV (10^{12} eV) energy and was operational in 1983.

Superconducting magnet technology has seen applications in large particle accelerators like HERA in 1991, RHIC, SSC, and LHC [2]. They also find applications in cyclotron magnets for heavy ion acceleration, cyclotron magnets for isotope production and therapy, synchrocyclotron magnets, etc.

In superconducting magnets, in general, the coils are placed inside a helium chamber and suspended from the outer vacuum chamber using supports. The helium chamber along with the coil is called as cold-mass of the magnet. The design of the cold-mass support system needs to consider two essential requirements; one is to have high strength material with a high cross-section. The second is less heat load to the helium, which requires materials with low thermal conductivity with lesser cross-sections. It is therefore necessary to optimize the design of the support system under thermal and magnetic loadings to choose the right stiffness of the support. The support system for large superconducting magnets, required for spectrometry, also needs to provide excellent alignment of the coils with respect to the iron yoke after cool-down and magnet energization to achieve high magnetic field accuracy.

A typical superconducting solenoid magnet configuration is schematically shown in Figure 1.2. The main components consist of the superconducting coil, thermal radiation shield, outer vacuum chamber, support system and magnet iron. While the coil is at cryogenic temperature, the magnet iron may be kept at room temperature or cryogenic temperature depending upon the design requirement.

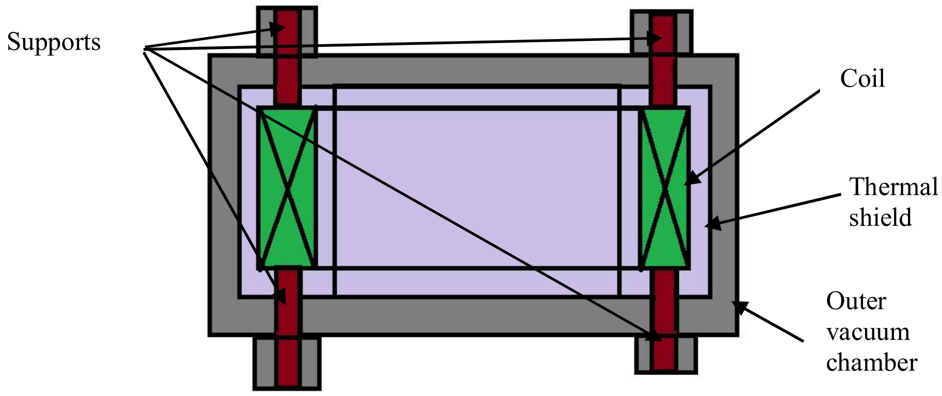

Figure 1.2 A typical cross-section of a superconducting magnet

(magnet iron yoke is not shown)

1.2 Type of magnets

1.2.1 Solenoid magnet

Solenoid magnets are the most widely used magnets. It consists of conductors tightly packed into a helix with or without an iron core. Figure 1.3 shows the coil configuration. High energy cyclotrons and large particle detectors use superconducting solenoid magnets.

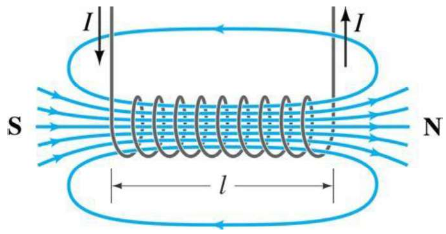

Figure 1.3 Solenoid magnet

1.2.2 Dipoles Magnet

Dipoles magnets are designed to create homogeneous magnetic fields over a distance. The particle motion in the field will be circular in the perpendicular plane to the field. A particle inserted between the pole of a dipole magnet will travel on a circular or helical trajectory [Figure 1.4]. The radial bending effect of the beam can be increased by many numbers of dipoles added on the same plane.

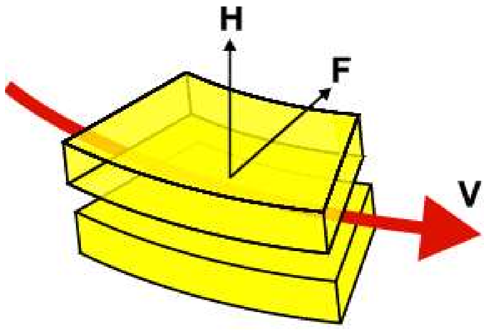

Figure 1.4 Dipole Magnet

1.2.3 Quadrupoles Magnet

Quadrupole magnets consist of groups of four poles [shown in Figure 1.5] designed in a way that the field is quadrupole in nature when a multiple expansion of the field is taken. These magnets are used in particle beam focusing.

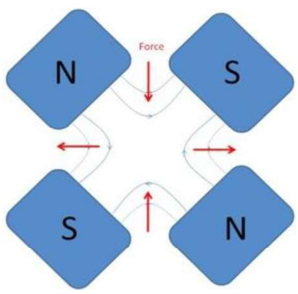

Figure 1.5 Quadrupoles Magnet

1.2.4 Toroid Magnet

The toroid is a useful device and is used in Superconducting Magnetic Energy Storage to tokamaks. Figure 1.6 shows a typical configuration of a toroid.

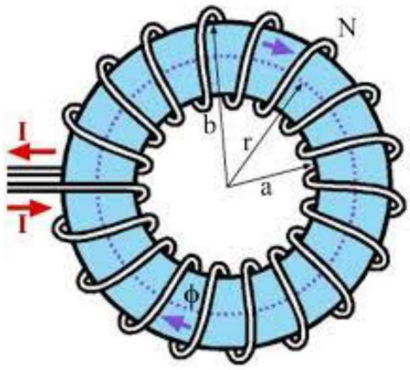

Figure 1.6 Toroid Magnet

1.3 Support system for superconducting magnets

Superconducting magnets use various kinds of support systems, like struts, links/straps, tie-rods, support posts, etc. [see Figure 1.7, Figure 1.8, Figure 1.9] and use different materials of construction to fulfill the requirements of the individual magnets. In general, the supports can be divided into two categories, one that takes axial load only, like links, tie-rods and one that takes the axial load as well as moments, like support posts.

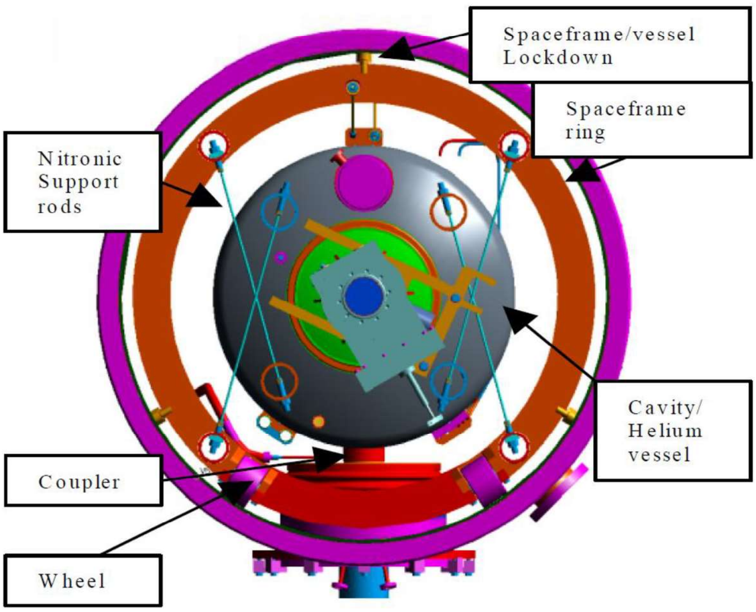

Figure 1.7 SNS cryomodule end view, showing rod type of support [3]

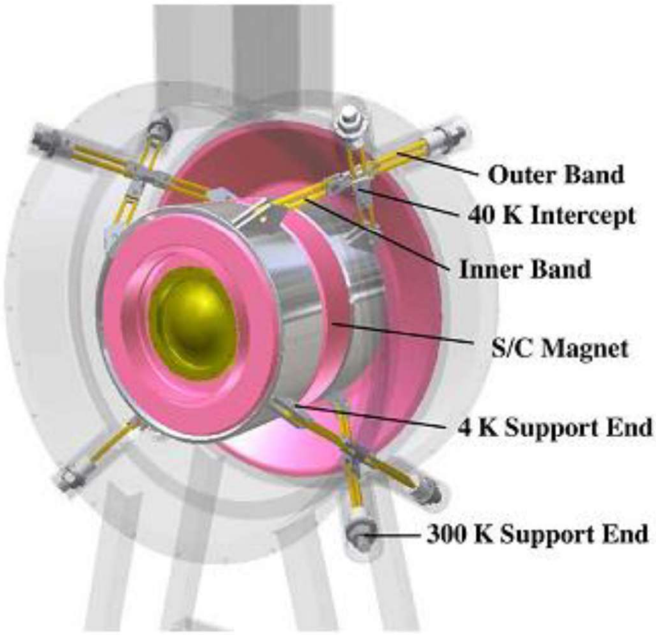

Figure 1.8 Cold-mass Support System for the MICE Focusing Solenoid, showing link type of support [4]

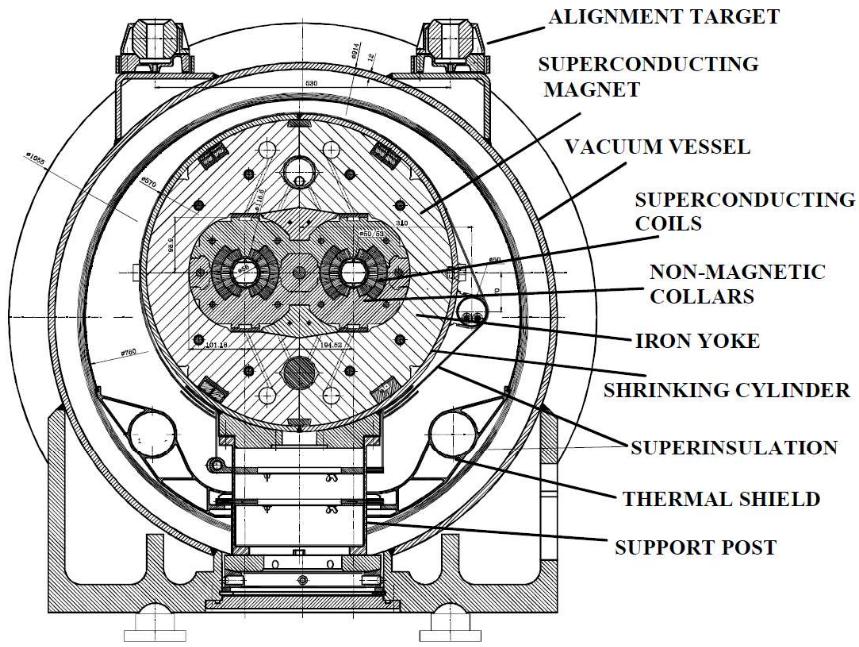

Figure 1.9 Cross-section of LHC cryodipole, using post type of support [5]

In superconducting magnets, the coils are placed inside a cryostat. An outer vacuum chamber surrounds that the coils to reduce convection heat-transfer. The coils are attached to a former that holds the coil in place resisting the conductor movement against magnetic force. The coils, along with its former together, are called as cold-mass. The cold-mass is suspended from the outer vacuum chamber using the support system.

The cold-masses, operating at cryogenic temperature, must be supported and connected to ambient temperature by the support system. A strong support system is required to bear the weight of the cold-mass, the thermal stress due to cold shrinkage, the magnetic force during coil energization and transportation loads. Because the support system would increase the thermal pass between the cryogenic and warm environment, low thermal conductivity and high mechanical strength materials are required [6].

Several authors have reported about diverse kinds of supports designed for the superconducting magnets. Race-track-shaped straps of GFRP have been used to support the cold-mass of superconducting magnets in particle accelerators, high-energy particle detectors [7] and MRI [8]. Materials such as CFRP [8] and titanium alloys are also used as tie rod materials because of their high strength and low thermal conductivity [9]. CFRP hollow tie rods were used in quadrupole magnets [10] and mid-infrared instrument (MIRI) [11] as longitudinal support and mounting struts, respectively, while the tie rods made of Ti5Al2.5Sn extra-low-interstitial grade titanium alloy were selected to support the cold-mass of the Barrel Toroid of ATLAS detector [12] and the solenoid of a CMS detector [13].

The design of the cold-mass support system of the magnet needs to consider about two essential requirements; one is to have high strength material with a high cross-section to provide enough rigidity against magnetic force. The second is to minimize the thermal heat load to the coil, which requires materials with low thermal conductivity with less cross-section. It is therefore needed to optimize the design of the support system under thermal and magnetic loadings to choose the right cross-section and stiffness of the support. To achieve high magnetic field accuracies, the support system for large superconducting magnets also needs to provide excellent alignment of the coils with respect to the yoke after cool-down and magnet energization. The placement accuracy requirement adds extra parameters for optimization of the support system.

Cold-mass is supported by several supports to restrain its movement during cool-down and energization. The purpose of the supporting system is to provide stability against magnetic force in the expense of small conduction heat load to the cryogen. Large superconducting magnets, like MICE Coupling magnets [14] and Mu2e Transport Solenoid Cold-Mass [15], are also required to have excellent alignment of the coils. MICE magnets are designed to have self-centered supports [14]. Self-centered supports are possible with the symmetrical magnets like solenoids. The unsymmetrical structure of the coils, e.g., superconducting spectrometer magnets [16] [17] or the unsymmetrical yoke [18], calls for designing the supports to minimize the coil movement.

1.4 Review of previous work

Several authors have reported about diverse types of supports designed for the superconducting magnets. Niemann et al. presented a tension member support made of epoxy-fiberglass for superconducting magnet and discussed on the minimization of heat leak to the magnet cold-mass [7]. The design of ISABELLE superconducting magnet support system is reported by V. Buchanan et al. [19]. Four fiberglass straps support the coil within a carbon steel vacuum vessel [19]. G.R. Jones and E.H. Christensen, in their paper, has created a database for stainless steel supports for thermal performance criteria. [20]

Hopkins et al. [21] discussed the optimized support systems for spaceborne Dewars. This paper presented a comparison of Dewar performance for both tension straps and the passive orbital disconnect struts (PODS) [21]. T. Hirakawa et al. [22] presented the design of advanced support straps for cryogenic applications and evaluated advanced composite materials for use in such straps because of their low thermal conductivity and high tensile strength. Thermal design for the straps had also been reported for optimization the advanced straps [22]. A simple one-dimensional model was developed by P. Kittel [23] to show the relative merits of different support systems for Dewar. The model considered both strengths-limited and resonant-frequency-limited applications for different supports affecting the parasitic heat load on Dewars. The model was used to compare straps, struts and disconnect supports. The comparison showed that struts are superior in strength-limited applications, straps are excellent in resonant-frequency-limited applications, while the disconnect struts are preferred for the lower on-orbit resonant frequency requirement than during launch [23].

R. M. Reimers et al. described the magnet coils system for HISS facility and discussed the support structures having a Z-shaped cross-section. The design consisted of flanged doubly tapered stainless-steel cylinders [24].

A. Lipski deliberated on an alternate design concept using a reentrant post design for the SSC dipole magnet support post that met the structural and thermal requirements and reduced the overall cost [25].

V. M. Bedakihale et al. presented the support structure design for the Toroidal Field Magnet System. The results of analytical and finite element analysis were presented [26].

A. Buenaventura et al. presented in their paper the static and dynamic studies of the LHC cryodipole in different configurations. The mechanical behavior of the cryodipoles was understood through tests and analyses [5].

Alessandria et al. reported about the mechanical characterization of the ATLAS-B0-model-coil tie rods [27]. Eight titanium alloy tie rods act as support against the magnetic forces. It also described a test facility that was built to test individual tie rods at cryogenic temperature [27]. B. Levesy et al. described the CMS coil suspension system and its mechanical analysis for different loading cases according to the operating conditions of the magnet [13]. Ti 6 Al 4 V ELI and Ti 5 Al 2.5 Sn ELI, two grades of Ti alloys, were considered for use [13]. O.P. Anashkin et al. presented an installation designed and manufactured to test the tie rods of Atlas Barrel Toroid superconducting magnets for a tension load of 2.5 MN and with 10 K to 270 K temperature gradient along the tie rod [12]. C. Mayri et al. presented the test report of the suspension system of Barrel Toroid cold-mass. The paper described the design, the tests and the behavior of individual coils [28].

Jun-ichi Ohnishi et al. described the support structure of the cold-mass for the Superconducting Ring Cyclotron. He has also detailed about the electromagnetic force measurements with strain gauges [29]. The cold-mass was supported by eight titanium-alloy rods in the vertical and azimuth directions, and by a stainless steel multi-folded pipe in the radial direction [29].

B. Wang et al. reported the design, development, and fabrication of the BESIII thin superconducting solenoid that generates 1.0 T central field. The 4.5 K coil and its support cylinder weighs 3583 kg [30]. Twenty-four radial supports, and twenty-four axial supports are used. The support designed considered for a electromagnetic de-centering forces of 63.7 kN in radial and 122.3 kN in axial direction together with a 3g axial and radial acceleration load. The design of the magnet, the cryostat and the cold-mass supports were discussed [30].

G. Biallas et al. described the support design of the Energy Doubler Dipole Cryostats and its mass production engineering [31]. The coils surrounded by a warm iron yoke was supported against high magnetic forces due to the errors in the concentricity of coil and iron yoke [31]. It is said that the ratio of the modulus of elasticity to the thermal conductivity is a figure of merit for evaluating support materials [31]. They introduced the equation of system spring constant expressed as:

$$\frac{1}{K_{system}} = \frac{1}{K_{support}} + \frac{1}{K_{coil\ sag}}$$

S.Q. Yang et al. presented the design parameters, mechanical and thermal, for the MICE focusing solenoid magnet. The results of finite element calculations were discussed including the forces and heat transfer in the cold-mass. The focusing magnet cold-mass support is reported as a self-centering support system consisting of eight tension bands [32]. The support system carry a sustained longitudinal force up to 500 kN together with a transient forces up to 1000 kN [32].

S.Q. Yang also proposed the self-centering cold-mass support system for Absorber Focus Coil (AFC) magnet. The support system comprised of eight supports strap assemblies. Each support strap assembly consisted of two oriented fiberglass epoxy support bands having two attachment hardware at each end and an intermediate temperature intercept in-between the two bands [33]. The overall spring constant of the cold-mass supports were required to be high enough to take the operating magnetic force, but the magnet center should not move more than ±1 mm and the axis of the magnet should not move more than ±0.7 mrad [33]. The design force of the AFC magnet cold-mass support system was taken as 700 kN [33].

H. Wu et al. [34] and L. Wang et al. [14] detailed about design and analysis of a self-centered cold-mass support system for the MICE coupling magnet. ANSYS FEM thermal and structural analysis was carried out on the cold-mass support assembly

[14]. Both 500 kN longitudinal and 50 kN radial force would be taken up by the support system after the magnet was fully charged. The cold-mass support system spring constants made for both directions (longitudinal and radial) was designed to be higher than $2x10^8$ N/m^{-1}. The allowable movement of the coil current center in the longitudinal direction was ±0.5 mm and in the radial direction was ±0.3 mm. ±0.001 radians was the maximum permissible tilt of the cold-mass axis. The magnet was designed to operate with limited cooling capacity of the cryo-coolers and the heat leak to the 4.2 K region through the support system was kept less than 0.25 W [34].

A theoretical model of a cold-mass suspension system for a superconducting magnet is reported by L. Li et al. [6]. The model presented considered that supported cold-mass, the cool-down tensile stress, and quasi-static acceleration load [6]. He has given the equation for thermal stress in each of the strap caused by cooling down, considering cold-mass and warm structures are mechanically rigid bodies, as: $\sigma_c = E\,\beta + E\,(L_c - L_w)/L_w$. In this equation, E is the elastic modulus of the strap along the length direction, β is the gradient thermal contraction rate of the strap, which results from a thermal gradient from the warm to the cold end. Gradient thermal contraction rate β can be thought off as half of integrated thermal contraction rate α, L_w is the warm distance between two attachment points and L_c is the distance between two attachments after cooling down [6]. Also, the load conditions during transportation and operating the superconducting magnet system were analyzed. The mechanical strength, minimum resonant frequency, and heat loads are considered in the design and presented in this paper [6]. The model was used to analyze the suspension structure of a superconducting magnet consisting of eight strap assemblies. The maximum pretension force was calculated, and the allowable accelerations for the maximum pretension were estimated [6].

A 2-D cold-mass support structure for the magnetic resonance imaging superconducting magnets, discussed by Kai Zhang et al., was made of CFRP tie rods [35]. Three main aspects, conductive heat leak, structure strength and mechanical vibration properties, of the cold-mass support structure were taken into consideration and an optimal design of the cold-mass support structure was presented including these three main aspects.

M. A Green et al. presented the Cold-mass Support System for the MSU Superconducting Cyclotron Gas-Stopper Magnet [36]. It is said that the magnet cold-mass support system carried the forces, pushing the magnet into the iron pole, together with any decentering forces came from the coil placement errors. The cold-mass support system consisted of six compression-supports for supporting magnet forces in the axial direction. Additionally, three radial supports helped to maintain the coaxiality between the coil axis with the axis of the iron poles. This paper presented an analysis of the cold-mass support system for the superconducting magnet and concluded that the designed support-system-spring-constant needed to be higher than the magnet force constant [36].

Kai Zhang et al. [9] investigated the tie rod support for a superconducting magnet with strict alignment requirements. It said that the superconducting magnets with stringent alignment requirements required that the coil was coaxially supported by warm bore with maximum deviation of 0.1 mm. The Ti-15V-3Cr-3Sn-3Al tie rod was considered here as the most appropriate cryogenic support material for its low thermal conductivity to Young's modulus ratio, isotropic mechanical property, and simple structure [9]. An optimized design of a 3-D cold-mass support structure based on Ti-15V-3Cr-3Sn-3Al tie rods was reported by considering the corresponding conduction heat leak, strength, and mechanical vibration property [9]. The relative vertical displacement between the coil and the warm bore was calculated for any external impact during transportation [9]. It was also reported that a slight shift of the coil was inevitable due to multiple shipments [9]. It was required to adjust the tie rod so that the magnetic axis of the running magnet was coaxial with the warm-bore center [9].

1.5 Objective

The main objective of the thesis is to study in detail the forces and coil shift in the link type of support structure for superconducting magnets analytically under thermal and magnetic loading. This methodology developed is unique in the sense that none has previously reported about the comprehensive analysis of the support system without using an elaborate finite element analysis. The finite element analysis for this requires involved electric-magnetic-thermal-structural coupled field models using commercial software [8]. The theoretical model adopted by L. Li [6] for cold-mass strap suspension system considered the cold-mass and warm structures as mechanically rigid bodies. The analytical model developed here also takes into account the deformation of the cold-mass.

The analytical method has been developed for both the superconducting dipole magnet and the solenoid magnet. This methodology has the advantage that it can be used for the preliminary design of the support system considering all the design constraints and further refinement may be done using finite element method whereby considerable design iterations may be avoided.

The study was made for a large aperture dipole magnet, which was being designed for FAIR Energy Buncher and a solenoid magnet for superconducting cyclotron at Kolkata. The results of this analysis were compared with the experimental data from the superconducting cyclotron magnet. During literature study, it was found out that varieties of materials are used to support structures for various applications. Superconducting magnets used in accelerator and detector applications are subjected to exposure to nuclear radiation and need to sustain irradiation damage over its lifetime. Irradiation studies were therefore carried out on pure Ti and Ti-6Al-4V alloy material, candidate for applications to support structures for superconducting magnets, and XRDLPA was carried out to characterize the microstructure of the irradiated and un-irradiated samples.

The scheme of the work is presented in Figure 1.10. The thermo-structural analysis includes temperature dependent thermal and mechanical properties. The study of the system also considers the Lorentz forces that are dependent on the coil current and its position with respect to the iron yoke. As a result, the stress developed in the support system and the coil position both changes with the increase of current, and therefore, the support stresses and coil position both are a function of current in the coil. Link type of supports has been studied here. The study aims to find the design methodology of link type support system for superconducting dipole and solenoid magnets.

The support links, generally designed for tensile loadings, hang the cold-mass of a superconducting magnet inside the outer vacuum chamber. They are designed to provide enough rigidity against magnetic force without much heat load to the helium. They are subjected to the following stress conditions depending upon the applied loads on the system:

1. Stress due to dead weights: Support link take the dead weight of the coil and associated structures and produce stress in the links
2. Pre-stress: Pre-stressing is done to ensure no slackness in the supports during initial assembly
3. Thermal stress: Cool-down of the coil to low temperature generates support stresses due to thermal contraction of different components
4. Magnetic stress: Magnetic force on coil produces support stress

In this thesis, an analytical methodology is described for the design of the support system, for link type supports. The design constraints considered are (a) the required coil positioning accuracy, (b) heat-leak through the supports, (c) support stress, and (d) supports system stability against magnetic force.

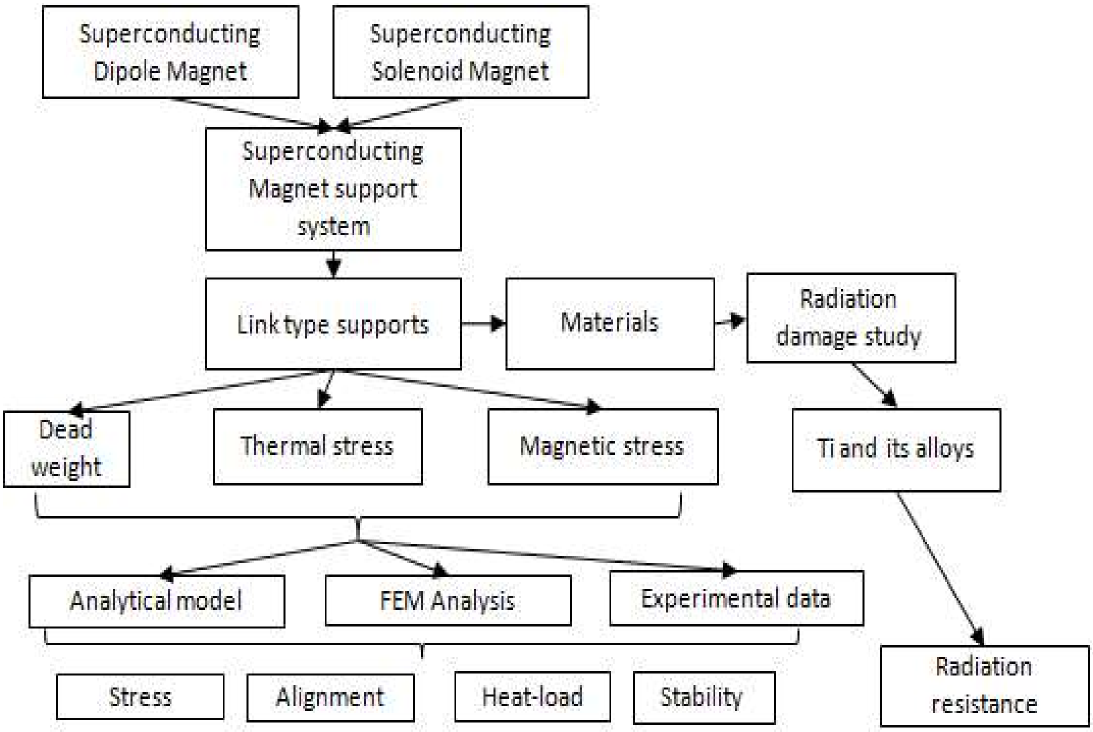

Figure 1.10 Scheme of the work

A detailed study on various support systems used for superconducting magnets has revealed that Ti and its alloys are important candidate materials owing to low thermal conductivity to strength ratio, which is comparable to G10 in 4-40K temperature range [9]. Superconducting magnets used in accelerator and detector applications are subjected to nuclear radiation exposure. During the operation of the accelerators, the radiation damage of the surrounding structural materials may sometimes occur if there is a considerable beam loss. Radiation damage would result in the generation of high energy neutrons due to a nuclear reaction. The cumulative damage with radiation exposure during its operation lifetime causes gradual but permanent changes in the microstructure. These changes, in turn, affect the physical and mechanical properties of the materials, which limit the performance of the structural components such as cryostat, support structures, etc. in a radiation environment. Support structure being one of the highly stressed structures in a cryostat, its limiting performance may limit the life of the instrument.

Ti-6Al-4V alloys show very high tensile strength and sufficient elongation at low temperature (15% at 77 K) [37] and is a candidate material for cryogenic support in accelerators [7], [12]. The radiation environment of the accelerators may make these support materials susceptible to radiation damage. Therefore, the effect of radiation damage on the microstructure and mechanical properties of Ti-6Al-4V is important to study. Samples of pure Ti and Ti-6Al-4V were taken and irradiated using proton beam from the Variable Energy Cyclotron, Kolkata, India. X-ray diffraction line profile analysis (XRDLPA) was used to characterize the microstructure of the irradiated samples in comparison with the un-irradiated ones using model-based techniques. Mechanical properties regarding the hardness of the irradiated samples have also been evaluated as a function of dose.

1.6 Organization of the thesis

The thesis is organized into five chapters as given herewith;

Chapter 1 starts with the general introduction of the support structure, description of various kinds of support structures being used by the superconducting magnets and objective of this study in details.

Chapter 2 deals with the link type of support systems analysis for superconducting dipole magnets for predicting the support stresses and coil movement under thermal & magnetic loading. The FAIR Energy Buncher Dipole magnet geometry was taken for detail analysis as an example.

Chapter 3 further extends the study to solenoid magnets and the movement of the coil. An analytical model was developed for calculating thermal forces in the coil and coil movement. Detail model was developed for the Lorentz force acting on the coil and magnetic force due to coil-yoke interaction. The methodology was applied for the superconducting cyclotron magnet at Variable Energy Cyclotron Centre, and the results were compared with the experimental data measured during cool-down and energization of the magnet.

Chapter-4 describes the irradiation study experiment, in detail, carried out for pure Ti and Ti-6Al-4V samples. The materials of the support systems, when used in the accelerators, may undergo radiation damage over the years (25-30 years lifetime of the accelerator) by the neutron-induced activity. It has been seen that the designers of superconducting magnets have used Ti and its alloys (Ti, Ti-6Al-4V, and Ti-5Al-2.5V) due to their high strength to thermal conductivity ratio. The X-ray diffraction line profile analysis results to characterize the microstructure as a function of dose have been discussed in this chapter. Microhardness of the irradiated, as well as unirradiated samples, have been measured as a function of irradiation dose.

The thesis concludes in **Chapter 5** that the analytical methodology described here could be a useful tool for the design and optimization of support systems in general and particularly for link type of support system. The analysis may also lead to effective coil centering reducing the efforts on the trial-error process. It has also been shown that Ti-6Al-4V can be considered as a suitable candidate alloy from the point of irradiation damage in accelerator applications.

Chapter 2
Analysis of support links for superconducting dipole magnet

Chapter 2

2. Analysis of support links for superconducting dipole magnets

Superconducting magnets use several types of support systems to suspend the cold-mass, coil and its former, inside the outer vacuum chamber. The purpose of the supporting system is to provide stability against magnetic force in the expense of a small conduction heat load to the cold mass. Several authors have reported about diverse types of supports used for the superconducting magnets. Niemann et al. presented a tension member support made of epoxy-fiberglass for superconducting magnet and discussed on the minimization of heat leak to the magnet cold-mass [7]. Kai Zhang et al. reported the cold-mass support structure made of CFRP tie rods for MRI superconducting magnet and conductive heat leak, structure strength and mechanical vibration properties were discussed [35].

Cold-masses are held by many supports to restrain their movement during cool-down and coil energization. Large superconducting magnets, like MICE AFC magnets [4] and dipole magnets of Energy Buncher of the FAIR Super-FRS [16], are also required to have excellent alignment of the coils. MICE magnets are designed to have self-centered supports [34].

Self-centered supports are possible with symmetrical magnets like solenoids. In many cases, the coils are unsymmetrical, e.g., superconducting spectrometer magnets [38], [39]. In these magnets, as the coil is cooled to liquid helium temperature, the coils, helium chamber and supports undergo thermal contraction. During the process, large thermal stresses are developed in the supports, and coil movement takes place. Moreover, once the magnet is energized, the resultant magnetic forces on the coils move it that redistribute the support stresses accompanying the further movement of the coil. It is therefore apparent that the coil will move from its original position in two steps, after cool-down, and as well as after energization.

The support system is responsible for excellent coil alignment as well as providing enough stiffness against the magnetic force. The system is to be designed in such a way that the heat load to the helium chamber is also minimum. With all these requirements put together, the design and optimization of the support system require a significant computational effort. H. Wu et al. carried out the extensive computation for MICE coupling magnet using Finite Element Methods (FEM) to arrive at a suitable solution [34]. In this work, an effort has been made to write analytical equations that can take care of the effect of all the supports together under thermal and magnetic loading and provide a reasonable solution for further details analysis.

In this chapter, an analytical methodology is described for the design of the support system for superconducting dipole magnets, for link type of supports. The design constraints considered are (a) the required coil positioning accuracy, (b) minimum heat-leak through the supports, (c) support stress, and (d) supports system stability against magnetic force. The finite element analysis for this system requires elaborate electric-magnetic-thermal-structural coupled field models using commercial software [14] and the multiple design iterations need a lot of time and memory. The analytical method described here has the advantage that it can be used for the preliminary design of the support system considering all the design constraints and further refinement is possible using the finite element method. The analytical methods allow us to avoid considerable design iterations.

A case study is made using the FAIR Energy Buncher large aperture superferric dipole magnet (3D view of the cryostat is shown in Figure 2.1). Table 1 shows the design parameters of the magnet. Large aperture superferric magnets have been fabricated and used elsewhere for various applications like A1900 fragment separator [40] at MSU, BigRIPS fragment separator [41] at RIKEN, in-flight separator RIA in USA, gas stopper [42] at NSCL, and correction magnets for SSC [43]. The required aperture of the FAIR Energy Buncher magnet is ±380 mm horizontal and ±100 mm vertical. The weight of the magnet iron is about 100 T [39].

The coil positioning accuracy for this magnet is stringent for achieving the required magnetic field uniformity. The magnetic analysis shows that the accuracy of ±1 mm is needed for achieving the desired magnetic field uniformity of $\pm 3 \times 10^{-4}$ [39] and calls for detail analysis of the coil movement. The results of the study are discussed in detail showing an instability region. The results indicate the importance of the initial alignment of the coil of achieving the desired position after magnet energization.

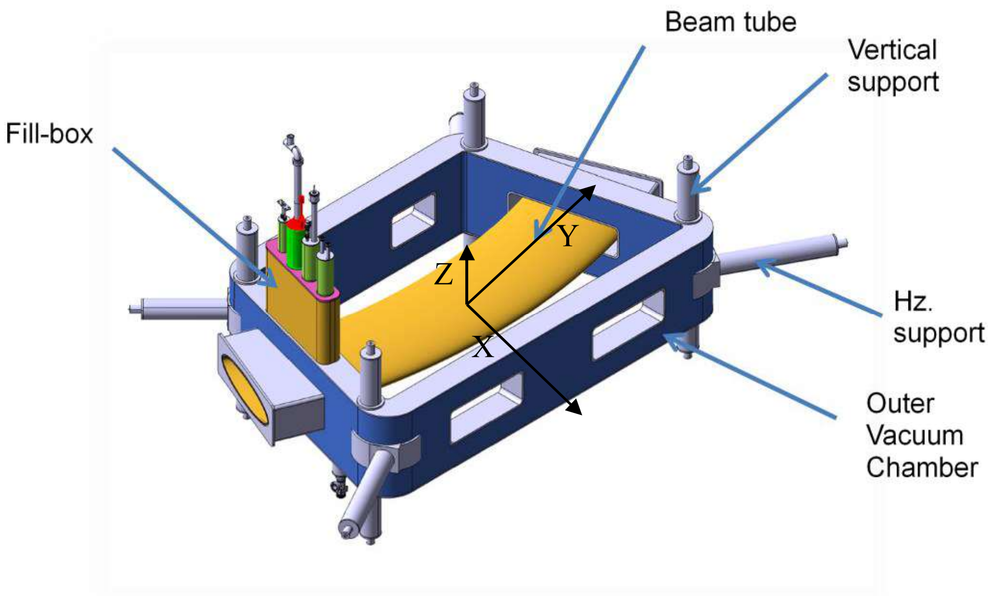

Figure 2.1 Cryostat for a typical superconducting dipole magnet

This analytical method also indicates the region of instability for the magnet support system. In this region, the stiffness provided by the support system is less than that of the magnetic rigidity. Therefore, this region needs to be avoided so that the support system does not go through uncontrolled deformation under the magnetic forces. The movement due to magnetic force results in coil misalignment and loss of magnetic field accuracy from the desired value. Coil centering is thus an important consideration for any high field magnet. Moreover, it is noticed that the initial alignment of the coil is somewhat important to achieve the desired coil position after the energization of the coil.

Table 1: Design parameters for dipole magnet

Parameter	**Value**
Maximum magnetic field at the center, Bmax	1.6 T
Bending angle	30°
Bending radius	437.5 cm
Pole face angle	0°
Field quality	$\pm 3 \times 10^{-4}$
Coil current	191 A

2.1 An analytical model for a support system for dipole magnet

The cryostat for a typical dipole magnet is shown in Figure 2.1. The trapezoidal coil is placed inside the outer vacuum chamber. Twelve support links suspend the coil and helium chamber assembly, called the cold-mass, from the outer vacuum chamber. The fill box is required to house all the helium and nitrogen plumbing lines and current leads into the helium chamber.

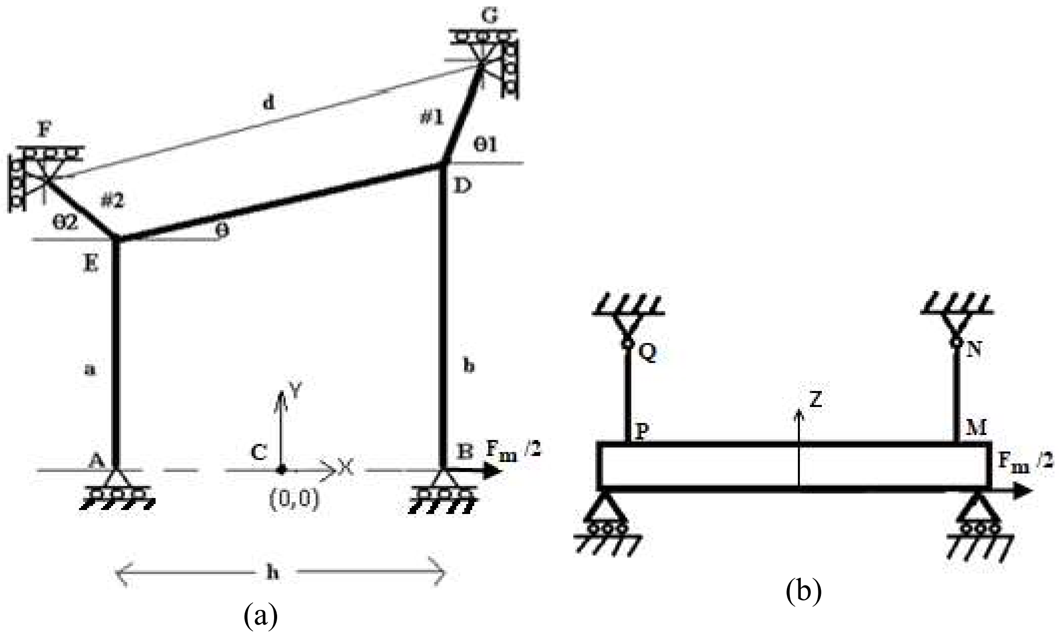

Figure 2.2: Model used for analytical calculation; (a) is top view & (b) is front view

To study analytically, the cold-mass and support structure, depicted in Figure 2.2, is modeled, keeping in mind the geometrical symmetry of the structure (X-Y plane and X-Z plane) and the direction of the magnetic force (F_m) on it. In Figure 2.2 (a), a top view of the cold-mass and support system is shown, where, AEDB depicts the cold-mass, DG depicts horizontal support #1, EF depicts horizontal support #2. Figure 2.2 (b) shows the front view of the cold-mass and support system model, where MN and PQ depict the vertical supports. Initially, the cold-mass and the support remain at room temperature. As soon as cool-down of the cold mass starts, the temperature of the cold-mass reduces, and a temperature gradient is established at the support links from the cold-mass temperature to the room temperature. Forces in the support links generate due to thermal contraction of the supports and the cold-mass. After the cold-mass reaches to the desired operating temperature and stabilizes, the current through the coil is set and the magnetic force is generated in the coil. In the present analysis, the applied thermal load on the cold-mass is taken as ΔT. Following are the assumptions made during the formulations of the model and its equilibrium equations:

a. 1/4-fold symmetry (X-Y plane and X-Z plane) of the structure is used. Symmetric boundary conditions are considered at the symmetric planes.
b. The coil and the helium chamber are assumed to have a uniform temperature of 4 K after cool-down.
c. The vertical support links remain vertical after cool-down and energization of the magnet.
d. Effect of the differential thermal contraction between coils and its former is neglected. Coil and former together is considered to be made of same material, i.e., stainless steel.
e. In the magnetic analysis, it is assumed that coil is made of rigid links, as the magnetic force is much less compared to the thermal forces and less likely to much deform the coil and former assembly.
f. Thermal and magnetic effects are not coupled, a method of superposition is used for finding out their combined effect.

2.1.1 Analysis for thermal deformation

After thermal contraction, the coil and helium chamber assembly referred to as cold-mass, is at equilibrium. The free-body diagram of the cold-mass is shown in Figure 2.3, where R_{H1} and R_{H2} are the horizontal reaction forces on the symmetric plane X-Z, whereas R_V is the vertical reaction force on the symmetric plane X-Y.
The steps of the analysis are listed below:

a. The geometry of the system is taken as input in terms of coordinates of points A, B, C, D, E, F, G, P, Q, M and N. Point C, the center of the pole, is taken as the origin and all the coordinates are stored as vectors. Vectors are called, for example, for point A as $\vec{A}$. The magnitude of the vector $\vec{A}$ is shown as A.
b. A', B', D', E' are the free position of the point A, B, D and E after cool-down. Point F, G, N, and Q does not change their position after cool-down. The free length of the helium chamber after thermal deformations is calculated by

multiplying the coordinate points A, B, D and E with $(1 - \int_4^{300} \alpha_b(T)dT)$; where, $\alpha_b(T)$ is the linear thermal contraction co-efficient of the helium chamber material.

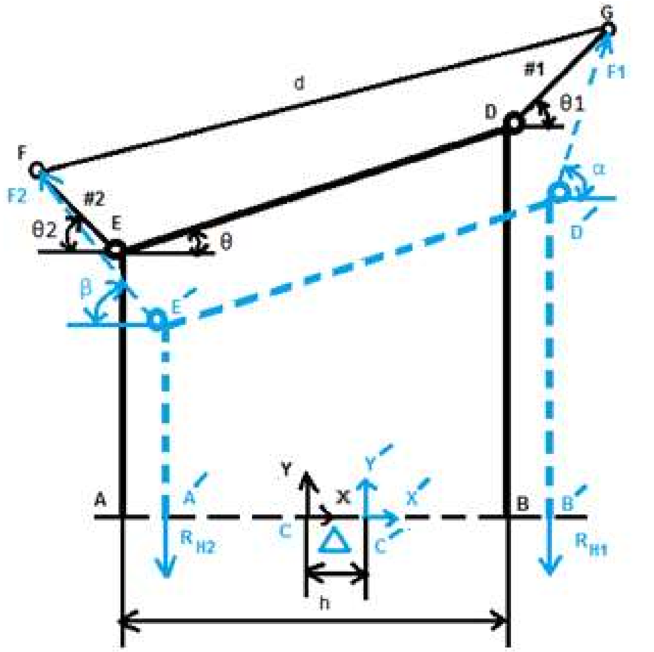

(a)

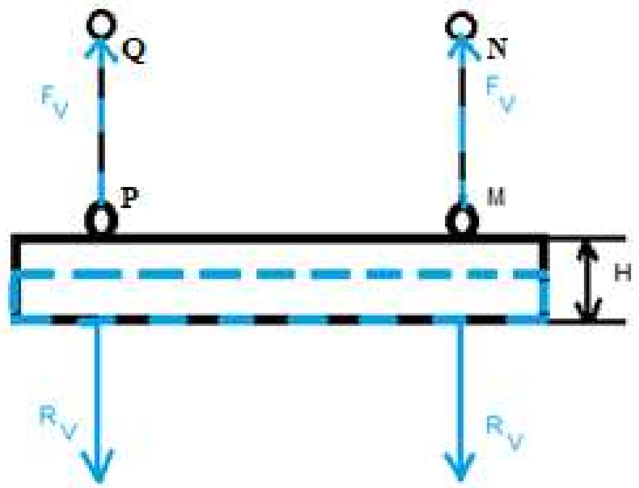

(b)

Figure 2.3: Free body diagram of cold-mass after cool-down; (a) Top view, (b) Front view

c. The stiffness of the system [31] is calculated [Refer to Annexure-1 for details] using Castigliano's Theorem [44] for the deformed geometry of the helium chamber for a force applied on support #1 only and is called as K_1. K_1 =

$f\ (\theta_1, \theta_2, \theta, a, b, c, L_s, A_b, E_b, A_s, E_s)$, where a, b and c are the length of arms of the coil, a = AE, b = BD and c = DE.

d. The stiffness of the system [31] is calculated [Refer to Annexure-1 for details] using Castigliano's Theorem for the deformed geometry of the helium chamber for the force applied on support #2 only and is called as K_2. $K_2 = f\ (\theta_1, \theta_2, \theta, a, b, c, L_s, A_b, E_b, A_s, E_s)$. L_s is the length of supports, A_s is the cross-sectional area of supports, E_s is the Young's Modulus of the support material, A_b is the cross-sectional area of helium chamber and E_b is the Young's Modulus of helium chamber material.

e. It is assumed that a small coil shift $\overrightarrow{P_t} = [x_t\ 0\ 0]$ has happened in X direction after cool-down. There is no coil movement in Y direction because of the symmetry of the structure with respect to the X axis. The resulted geometry is shown in Figure 2.3 in dotted line.

f. Equations 2.1, 2.2, 2.3, 2.4 are solved to get the unknowns F_1, F_2, F_v and x_t.

At equilibrium, the following equations are valid:

$\sum F_x = 0$; i.e.

$$F_1\, cos(\alpha) - F_2\, cos(\beta) = 0 \qquad \dots 2.1$$

From symmetry, $\sum F_y = 0$, $\sum F_z = 0$ and $\sum M = 0$.

The deformation of support link #1 due to force F_1 can be written as:

$$d_1 = \frac{F_1}{K_s}$$

The deformation of the system of the coil under the force F_1 is written as:

$$d_2 = \frac{F_1}{K_s}$$

The thermal deformation of the support links is given by:

$$d_3 = L_s(1 - \int_4^{300} \alpha_s(T) dT)$$

The length of the support link #1 at equilibrium is the vector length of D′G, i.e. $\overrightarrow{L_{11}}$. Where, B′D′E′A′ is the coil after thermal contraction and moved by the Δ distance to satisfy the force equilibrium condition.

Therefore, from deformation balance, we can write:

$$d_3 - d_1 - d_2 = |\overrightarrow{L_{11}}|$$

We can rewrite the above equation as:

$$F_1\left(\frac{1}{K_s}+\frac{1}{K_1}\right) = L_s\left(1-\int_4^{300}\alpha_s(T)\,dT\right) - |\overrightarrow{L_{11}}| \quad \dots 2.2$$

Similarly, from deformation balance, we can also write:

$$F_2\left(\frac{1}{K_s}+\frac{1}{K_2}\right) = L_s\left(1-\int_4^{300}\alpha_s(T)\,dT\right) - |\overrightarrow{L_{22}}| \quad \dots 2.3$$

$$F_v\left(\frac{1}{K_s}\right) = \int_4^{300}(L_s\,\alpha_s(T) + H\,\alpha_b(T))\,dT \quad \dots 2.4$$

Where, F_1 and F_2 are the magnitude of the support forces for support #1 & #2 respectively, α and β are angles of supports with respect to X-axis after cool-down, F_v is the force in the vertical supports. $\overrightarrow{L_{11}}$ is the vector between points D′ and G and is a function of x_t. $\overrightarrow{L_{22}}$ is the vector between points E′ and F and is also a function of x_t. K_s is the support stiffness i.e. $K_s = A_s\frac{E_s}{L_s}$. α_s is the linear thermal contraction coefficient of support material, L_s is the length of each support, H is the height of the helium chamber from the symmetry plane.

Another method can also be taken to arrive at the same equations with a slightly different form. Using Castigliano's theorem [44], one can write the deformation of the system in terms of the complementary potential energy as below:

$$U^* = \frac{F_1^2\left(\frac{1}{K_s}+\frac{1}{K_1}\right)}{2} + \frac{F_2^2\left(\frac{1}{K_s}+\frac{1}{K_2}\right)}{2}$$

Differentiating with F_1, we can write:

$$\delta = \frac{\partial U^*}{\partial F_1} = F_1\left(\frac{1}{K_s}+\frac{1}{K_1}\right) + F_2\left(\frac{1}{K_s}+\frac{1}{K_2}\right)$$

We can also write that the total deformations happened due to thermal contraction for support #1 and the coil can be written as:

$$d_1 = L_s\left(1-\int_4^{300}\alpha_s(T)\,dT\right) - |\overrightarrow{L_{11}}|$$

And, the total deformations happened due to thermal contraction for support #2 and the coil can be written as:

$$d_2 = L_s\left(1-\int_4^{300}\alpha_s(T)\,dT\right) - |\overrightarrow{L_{22}}|$$

We can say that the total deformations happened due to thermal contraction is equal to the deformations due to thermal forces. Therefore,

$$\delta = d_1 + d_2$$

i.e.

$$F_1\left(\frac{1}{K_s}+\frac{1}{K_1}\right)+F_2\left(\frac{1}{K_s}+\frac{1}{K_2}\right)=L_s\left(1-\int_4^{300}\alpha_s(T)\,dT\right)-|\overrightarrow{L_{11}}|+L_s\left(1-\int_4^{300}\alpha_s(T)\,dT\right)-|\overrightarrow{L_{22}}|$$

.... 2.5

We can, therefore, solve equations 2.1 and 2.5 and find out F_1 and F_2.

The cold-mass cools down from room temperature to liquid helium temperature. As temperature goes down, the contraction of cold-mass and support system results in thermal stresses in the support system. At steady state, the forces generated in the support system may shift the coil to reach an equilibrium condition. As the system of forces is indeterminate, both force equilibrium and deformation compatibility need to be satisfied for reaching a complete equilibrium of the system. The equations 2.1 has come from the force equilibrium and 2.2, 2.3, 2.4 have generated from deformation balance. The thermal forces generated within the system is always self-balancing, and hence equilibrium in the system is achieved by the shift of the coil.

2.1.2 Analysis for magnetic force

The model used is schematically illustrated in Figure 2.4. The structure is statically indeterminate; the method of force is applied to solve it.

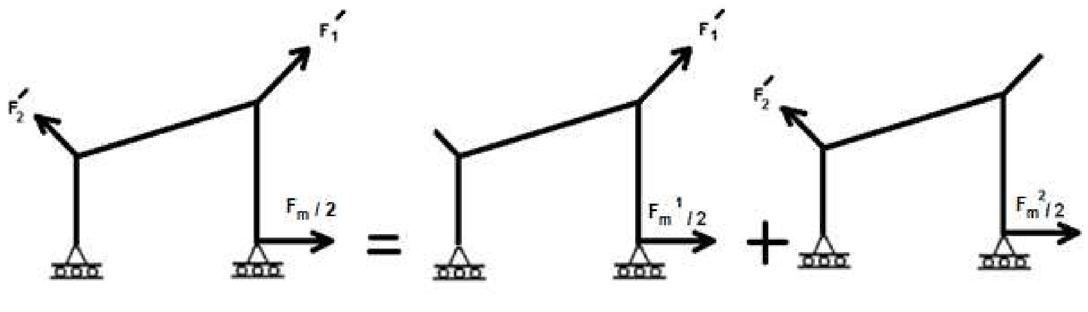

Figure 2.4: Model used for studying the effect of magnetic force (F_m). F_1' and F_2' are support reactions.

The steps of the analysis are listed below:

a. The deformed geometry of the coil and support after cool-down is taken as input.
b. Assumed that a small coil shift ($\overrightarrow{P_m} = [x_m\ 0\ 0]$), from the origin, has happened towards X-direction. The resultant magnitude of the magnetic force (F_m) on the coil for the corresponding coil shift (x) is taken as input from the magnetic analysis [Figure 2.10]. A linear equation, $F_m = 0.79E + 06\, x + 5152$, is fitted for this analysis, where x is the distance of coil center from the origin in meter.
c. This configuration is an indeterminate system of forces. The force and deformation balance equations (2.5), (2.6) and (2.7) are solved for three unknowns, F_1', F_2' and x_m.
d. The forces, F_1' & F_2' are added to the thermal forces and plotted in Figure 2.11.

In equilibrium, we can write, $\sum F_x = 0$, therefore,

$$-F_1{}'cos(\alpha) + F_2{}'cos(\beta) = \frac{F_m}{2} \qquad \text{... 2.6}$$

Again, the deformation of support under the force $F_1{}'$ is given by:

$$d_1 = \frac{F_1{}'}{K_s}$$

At the equilibrium, the length of the support is given by the sum of the magnitude of the vector length of the support link, i.e. $\overrightarrow{L_1}$ and the coil shift, i.e. ,$|(-\overrightarrow{P_m} + \overrightarrow{L_1})|$. From deformation balance, we can therefore write:

$$|(-\overrightarrow{P_m} + \overrightarrow{L_1})|\, K_s = F_1{}' \qquad \text{... 2.7}$$

Similarly,

$$|(-\overrightarrow{P_m} + \overrightarrow{L_2})|\, K_s = F_2{}' \qquad \text{... 2.8}$$

Where, F_1' and F_2' are forces generated in supports due to applicatthe ion of magnetic forces on the coil. F_m is the magnitude of the resultant magnetic force on the coil as shown in Figure 2.4. $\overrightarrow{L_1}$ and $\overrightarrow{L_2}$ are vector lengths of the support links after cool-down.

In the case of FAIR dipole magnet, the resultant magnetic force in the coil is directed towards +ve X-direction. The force equilibrium in the system is achieved by small movement of the coil towards X-direction.

2.2 Supports for Energy Buncher dipole magnet

The Energy Buncher dipole magnets for the FAIR project are of the super-ferric type in design [39]. They have a radius of 4.375 m, a maximum magnetic field up to 1.6 T with uniformity within $\pm 1.5 \times 10^{-4}$ over an elliptical bore of size ±250 mm × ±70 mm and an effective length of 2.43 m to bend ion beams by an angle 30°. This magnet system consists of mainly two sub-systems - cryostat and warm iron yoke. Cryostat, consisting of the vacuum chamber, radiation shield, and helium chamber, was designed for providing liquid helium environment to the epoxy potted Nb-Ti superconducting coil. The dimension of the iron core is shown in Figure 2.5.

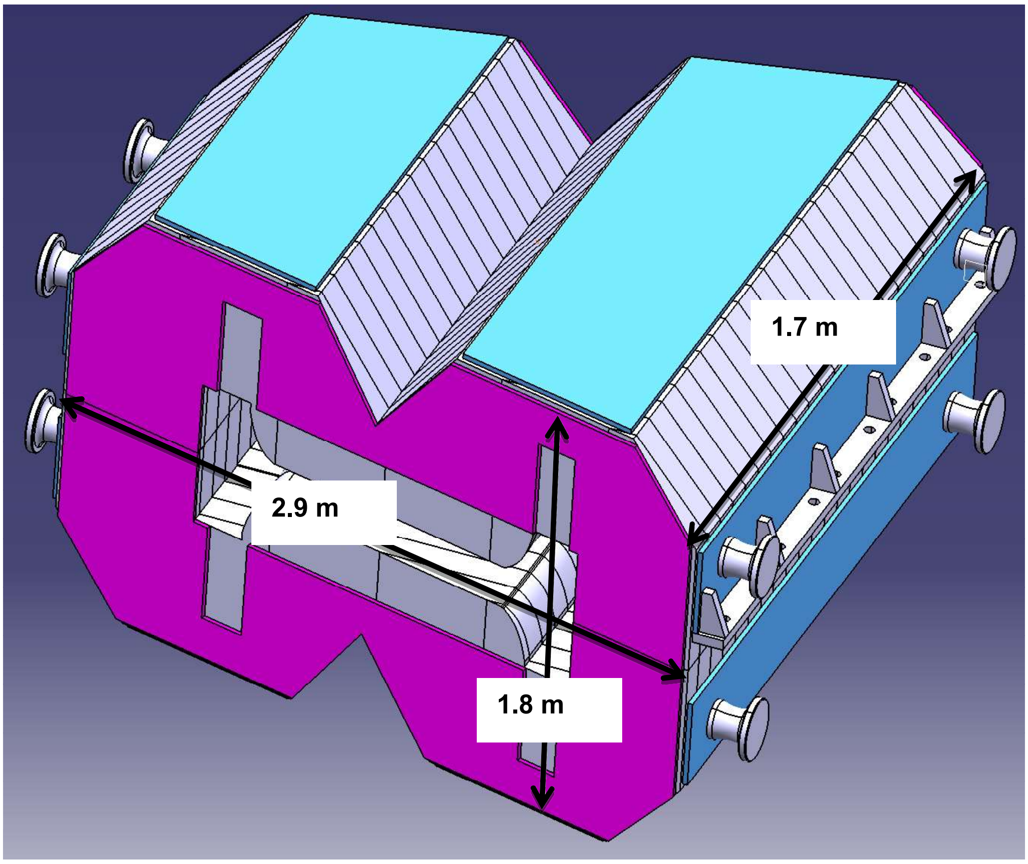

Figure 2.5 Dipole magnet iron assembly

Figure 2.6 shows the cryostat. It has a helium vessel, inside which the coil is immersed, a thermal radiation shield cooled by cold helium gas, and an outer vacuum chamber surrounding the radiation shield. Twelve glass epoxy support links – four uppers, four lowers and four horizontal links – support the helium chamber. One end of the support links are connected with the liquid helium vessel and the other end to the outer vacuum vessel. End of the support links is provided with an adjustable nut for relaxing the supports during cool-down and movement of the coil for fine tuning the magnetic field accuracy after the field measurement. The helium chamber and thermal shield are multilayer insulated. All the support links and other port connections from room temperature to the liquid helium have cold helium gas cooled thermal intercepts to reduce heat load to the liquid helium.

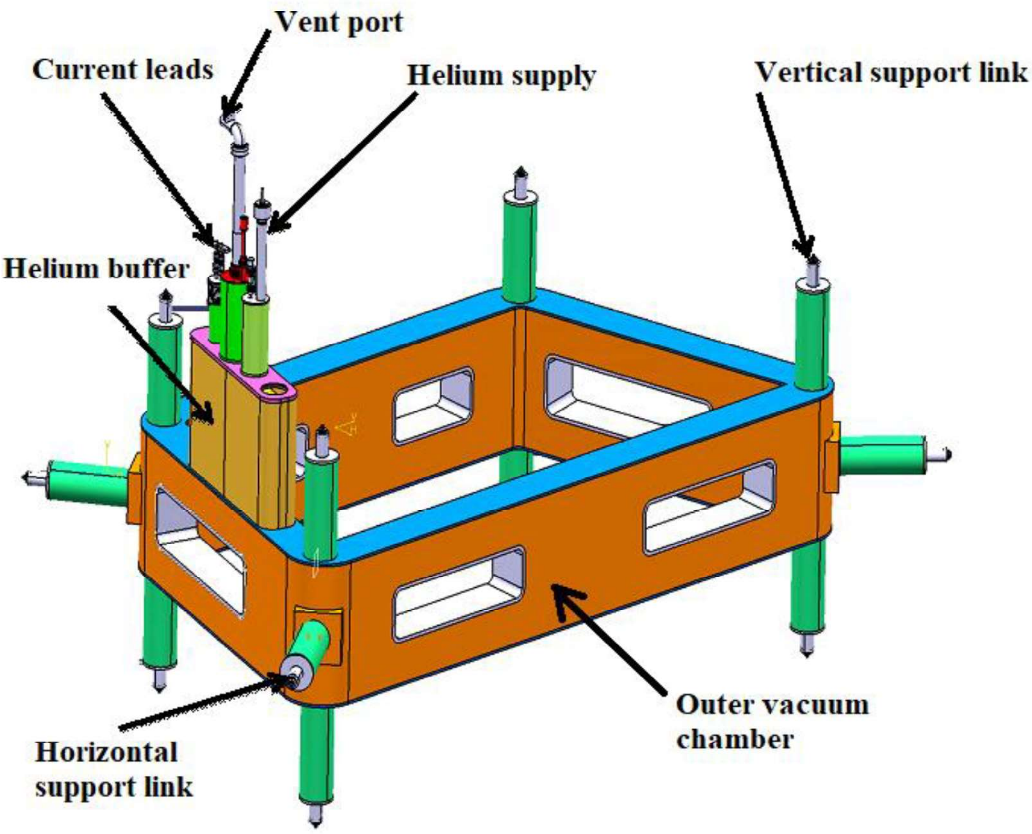

Figure 2.6 Cryostat for Energy Buncher dipole magnet - showing vertical and horizontal support links

A small liquid helium storage vessel is attached on the top of the cryostat to facilitate insertion of current lead, liquid helium line, helium gas exit port, safety port and instrumentation connections. Vapour cooled current leads is connected to the coil. This liquid helium vessel needs to be interfaced with the cryogenic lines as available at the site.

The magnet requires close tolerance on the pole pieces and coil positioning (±1 mm) for achieving the required field quality of ±3 x 10^{-4}. The cryostat shown in Figure 2.6 consists of four upper vertical, four lower vertical and four horizontal support links to connect the helium chamber to the outer vacuum chamber. The support system is so designed as to minimize the coil shift and heat in-leak while keeping support stability and stresses within the limit. The coil size to be supported is about 3 m x 1.8 m. The lengths of the supports are taken as 0.3 m with thermal shield intercept at one-third of the length of the support from the warm end.

For finding out the support forces and coil movement after cool-down, equations 2.1, 2.2, 2.3 and 2.4 are first solved for the dipole magnet geometry. The cold-mass temperature is taken as 4 K, and the temperature of the ambient is considered as 293 K. The geometry is then modified considering deformations and coil movement after cool-down and is taken as input in the analysis for magnetic forces. Equations 2.5, 2.6 and 2.7 are next solved to find out support forces and coil shift.

2.3 FEM analysis

The 3D model of the coil, helium chamber (cold-mass) and support links were generated for the analysis in ANSYS [45] using ANSYS Parametric Design Language (APDL) as shown in Figure 2.7. The twelve-support links were modeled as straight rectangular section rods.

All the support links were fixed at the warm end, and the temperature of the warm end is assumed to be at 293 K. It was also assumed that the cold-mass had reached the cold temperature and a temperature boundary condition of $T_o = 4$ K (temperature of the coil and helium chamber) was applied on all the nodes of the coil and helium chamber. Steady state thermal analysis was done for finding out the temperature distribution, and subsequent structural analysis was made for finding out force and deformations (shown in Figure 2.8).

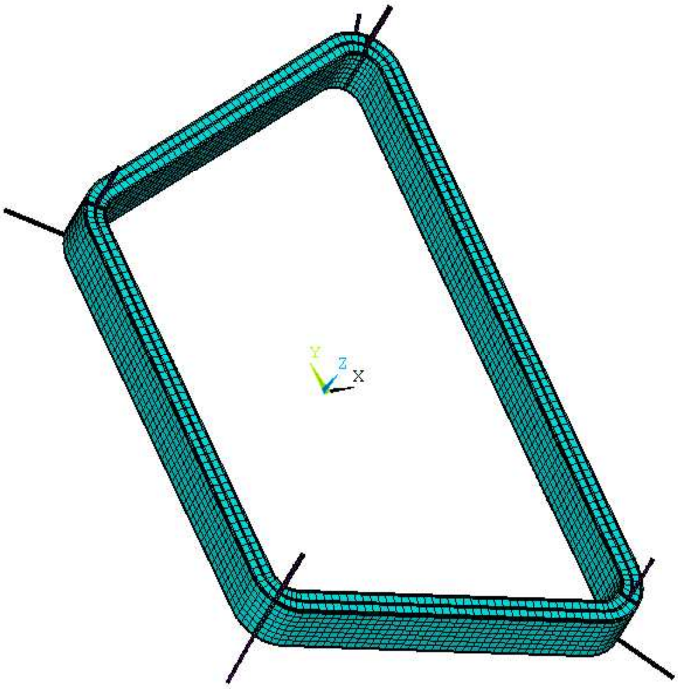

Figure 2.7 ANSYS model of coil and support links for Energy Buncher dipole magnet

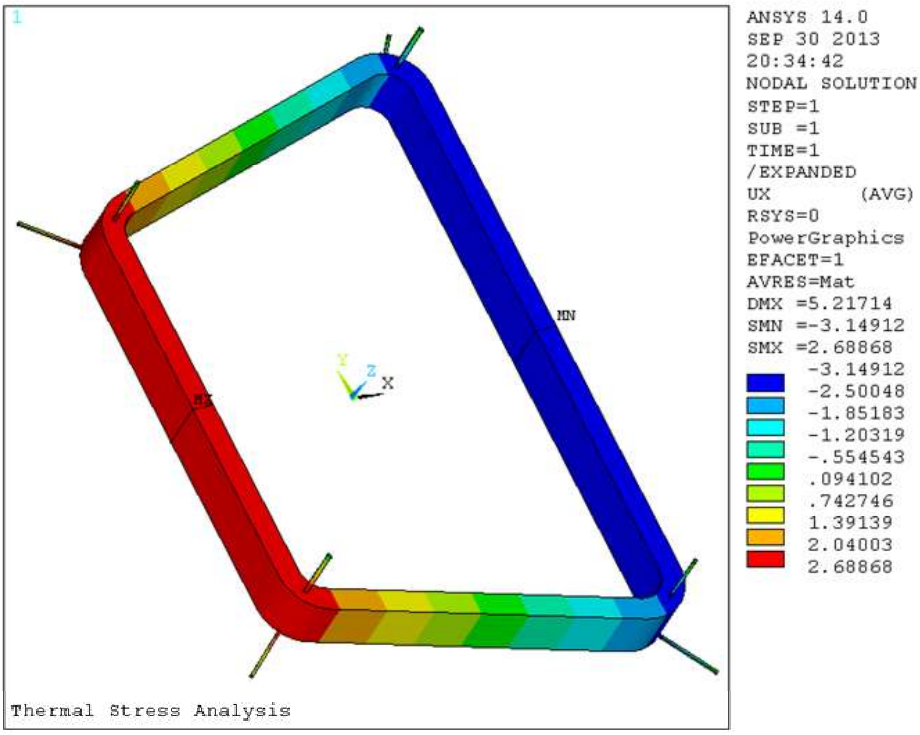

Figure 2.8 Thermal deformations in the cold-mass of Energy Buncher dipole magnet found out using ANSYS

The support reaction forces were taken as the output of the analysis. The center of gravity (CG) of the coil and helium chamber was calculated using APDL command before solution and after solution and the CG difference between them is considered as coil shift. The coil shift, derived analytically and using ANSYS, is compared in Figure 2.9. It is seen that the coil moves in negative X-direction after cool-down and is dependent only on the geometry of the structure and material of construction irrespective of the support stiffness value.

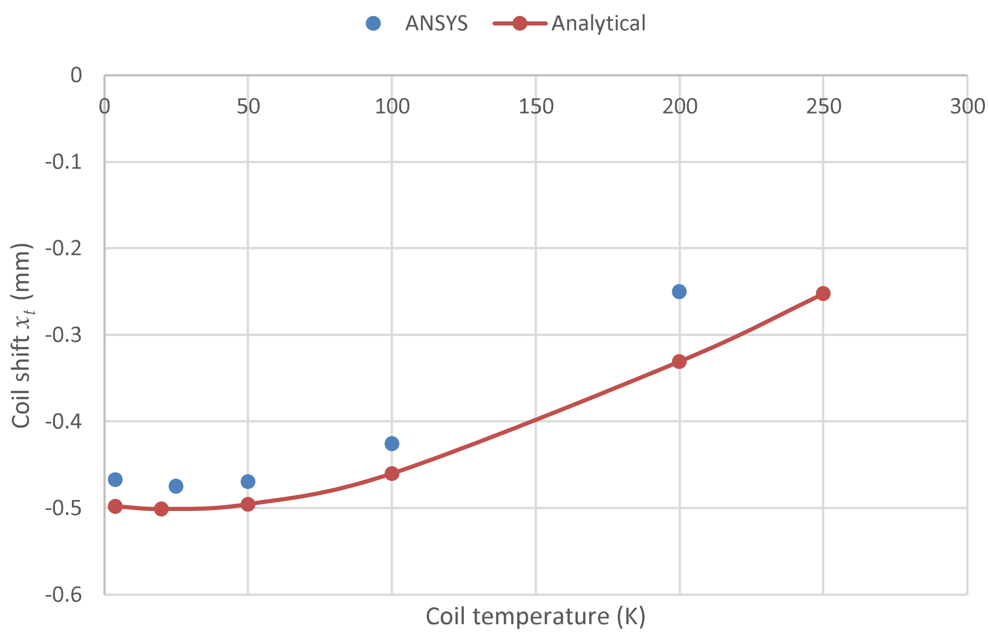

Figure 2.9 Comparison of analytical and ANSYS results of coil shift

2.4 Optimisation of support system for Energy Buncher dipole magnet

The support system optimization was done for the coil assembly using the analytical method. The geometry is taken from the magnetic analysis done to achieve the desired magnetic field uniformity [39]. The resultant magnetic force on the coil, obtained from magnetic analysis using ANSYS MSP formulation, for different distance of the coil center from the origin is plotted in Figure 2.10 and is taken as input the study. Virtual work technique is used for the computation of forces [46]. The fluctuations in the graph data are due to numerical errors of discretization.

The support stiffness was varied, and its effect on the support stress, coil shift, and heat load were plotted. Figure 2.11 shows a plot of the support force versus stiffness of each Ti-6Al-4V [47] support links after cool-down and subsequent energization of the magnet. It can be seen that the forces increase with the increase of support stiffness.

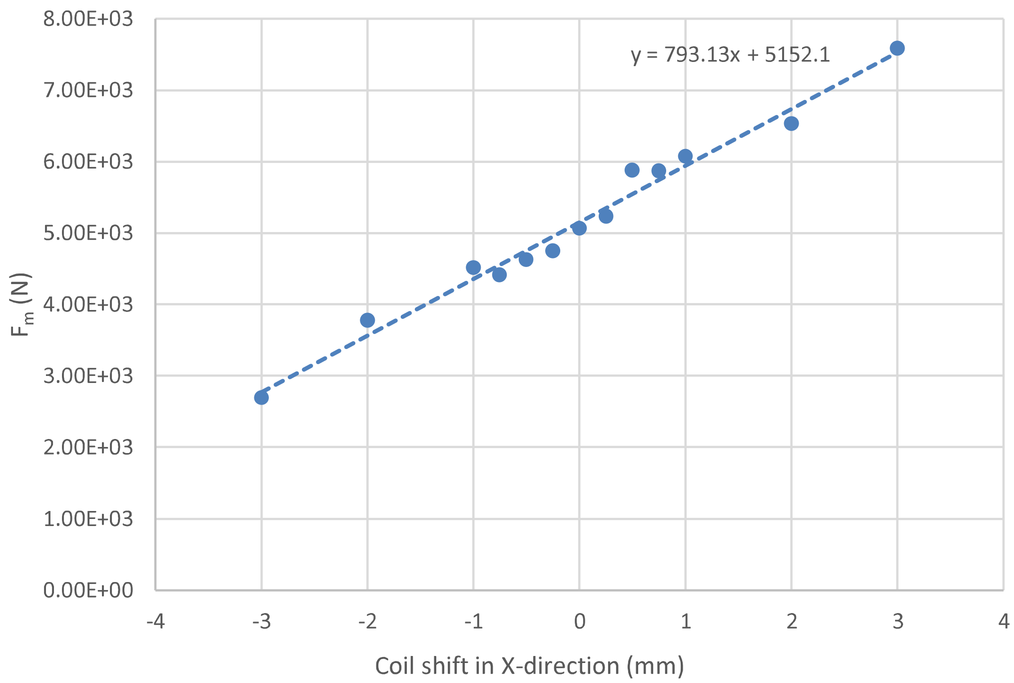

Figure 2.10: Magnetic force (F_m) vs. distance of coil center from the origin

The forces monotonically increase in the support as the stiffness increases, though stresses vary differently. In this analysis, the stiffness of the supports is varied by increasing the cross-sectional area of the supports keeping the length constant. The reason is that there is not much play with the support length as the distance between the magnets are very close, and the support of two nearby magnets will interfere with each other if made much longer.

When the magnet is energized, the support forces $F_1{}'$ decreases and $F_2{}'$ increases from its value after cool-down. The support stress S_1 always decreases with the increase in support stiffness as the cross-sectional area increases while F_1 decreases. In contrast, the support stress S_2 increases for an increase in support stiffness. In this case, both cross-sectional area of the support and F_2 increase. The results in the

Figure 2.11 shows that S_2 increases and this can happen if the rate of increase of F_2 is more than the rate of increase of support cross-section A_s. It is also seen that stresses are always very high because of large magnet geometry and this necessitates the loosening of the supports during cool-down to reduce stresses in the support links to keep it within the allowable limit of the material.

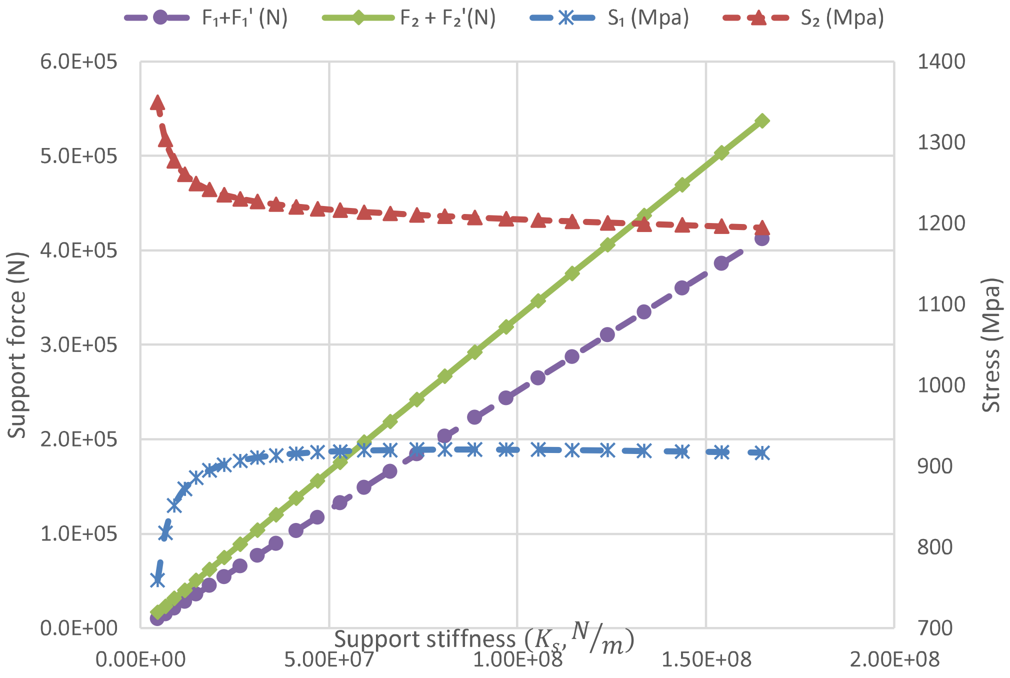

Figure 2.11 Support force vs. support stiffness ($F_1 + F_1'$) and ($\mathrm{F}_2 + \mathrm{F}_2'$) are forces after coil energization. S_1 and S_2 are support stresses, calculated by dividing the forces with crosa s-sectional area of each support

The total coil movement, $x_f = x_t + x_m$, is calculated with respect to the mid-point of the iron pole for varied support stiffness values (Figure 2.12). The peak areas are instability region where a small movement of the coil results in its uncontrolled movement that may cause support failure. This region moves on the higher stiffness side with the increase of the magnetic force value as the magnetic field is increased. It is therefore evident that stiffness value should be greater than 1.00E+07 for FAIR dipole magnet to avoid this region.

The instability region for low support stiffness is shown in the graph as a sudden increase of coil movement (as seen in Figure 2.12 for K_s less than 1.0E+07 N/m for

B=1.6 T). The negative value of coil movement below this stiffness value is not showing the real result, it is only an artifact of numethe rical solution of mathematical equations.

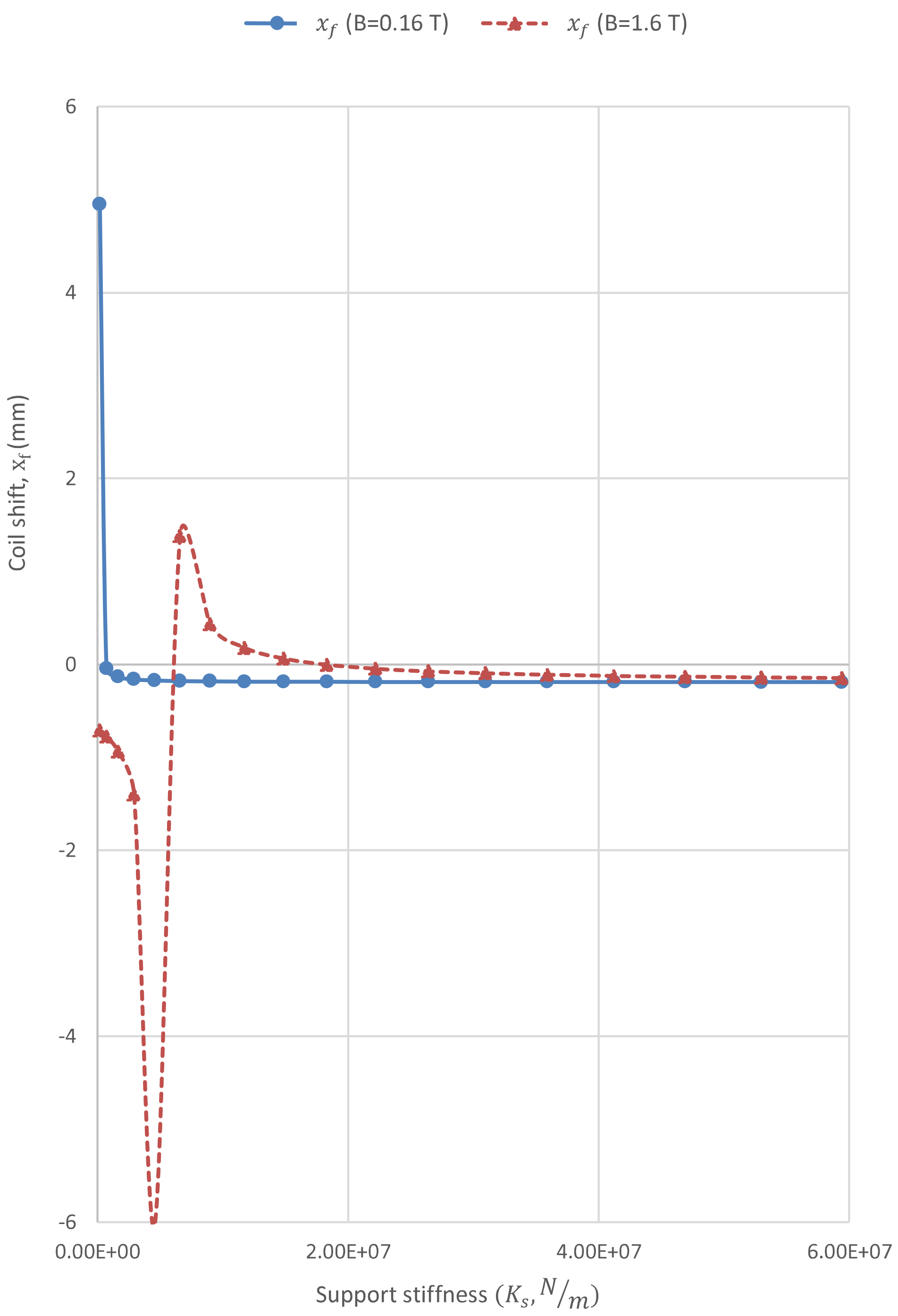

Figure 2.12: Coil center shift (x) vs. support stiffness (K_s) plot for highest (1.6 T) and lowest (0.16 T) magnetic field values.

The coil moves towards negative X-direction after cool-down and tries to move from negative to a positive direction as the resultant magnetic force is in positive X-direction. The increase in support stiffness increases the stiffness of the system and thus results in less coil shift from the point, where it was after cool-down. At a large stiffness value, the coil should stay at the same location, where it was after cool-down. At the lower magnetic field, the magnetic forces are not large enough to move the coil towards positive X-direction, and hence the coil stays close to the point, where it was after cool-down (as shown in Figure 2.13 as a graph for B=0.16 T).

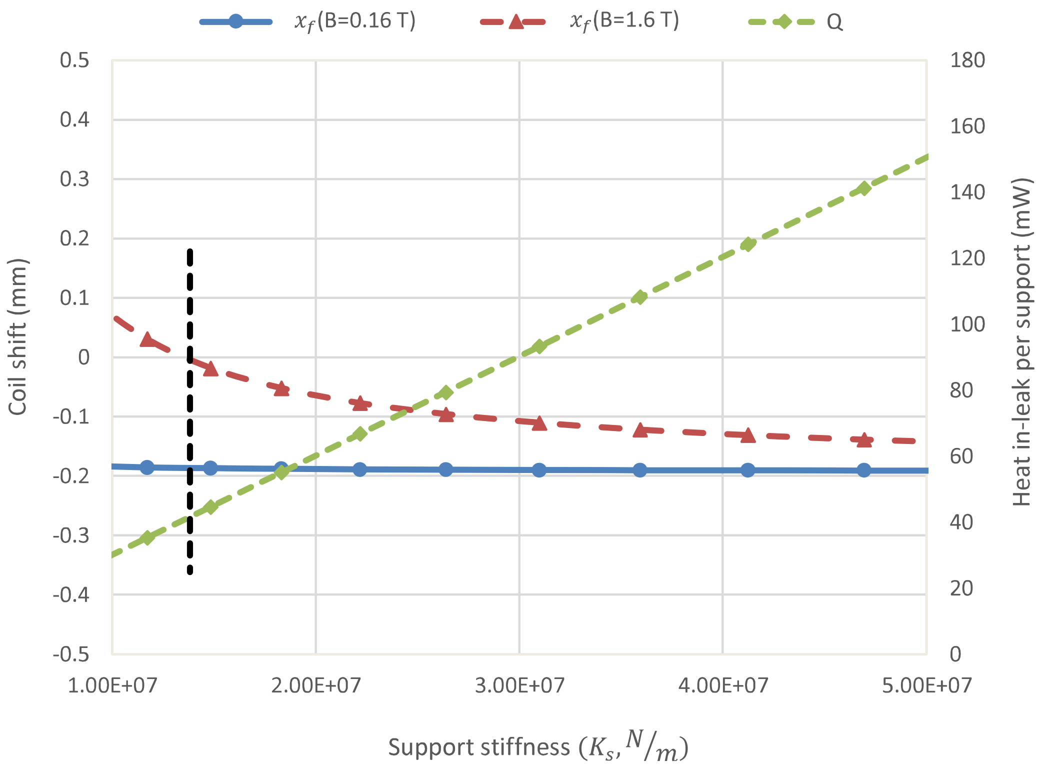

Figure 2.13: Coil shift and heat in-leak vs. support stiffness

The heat in-leak through each support to liquid helium is calculated using the following equation [48]:

$$Q = \frac{3}{2}\frac{A_s}{L_s}\int_4^{80} K(T)\, dT$$

… 2.9

Where, Q is the heat in-leak, A_s the area of support, L_s the length of support, $K(T)$ is the thermal conductivity of support at temperature T [47]. It is assumed that the intercept is at $\left(\frac{2}{3}\right)^{rd}$ length of the support link and the temperature of the support is at 80 K. The heat in-leak increases with the increase of support stiffness due to the increase in support link cross-sectional area.

Figure 2.13 shows a set of graphs of coil shift and heat in-leak per support for the magnet. The plot is shown beyond the instability region from a minimum K_s value of 1.00E+07 and for ± 0.5 mm range for movement of the coil. A point is marked in the plot (dotted line) where the coil movement is almost zero for B=1.6 T magnetic field. At this point ($K_s \cong$ 1.5E+07 N/m), the maximum coil movement is 0.2 mm for B=0.16 T operation of the magnet and heat in-leak is a little over 40 mW per support. For minimum magnetic field (0.16 T), the magnetic force is small, and the coil remains at the position where it was after cool-down.

2.5 Effect of initial positioning of the coil

It is important to place the coil at the right position during assembly with respect to the poles to keep it at the desired location even after cool-down and coil energization.

Figure 2.14 shows a plot of coil movement with different initial positioning error (x_i) of the coil. It is seen that the initial position is very important to achieve the desired accuracy of coil position after cool-down and coil energization. The FAIR dipole coil is to be placed with an accuracy of ± 0.2 mm to achieve the desired positioning accuracy of ± 1 mm, even after energization.

It seems that initial alignment of such a large coil with an accuracy of ±0.2 mm is challenging. Some special methodology is to be called for doing this. It may be possible to align the coil for different excitations forgetting initial position to achieve the required field uniformity by some external adjustment nuts. This method would be a very tedious task requiring magnetic field measurement at different excitations. A force balance technique, in which the support reaction forces are measured, and coil centering is done by balancing this force by moving the coil [49], looks more effective way to deal with the situation.

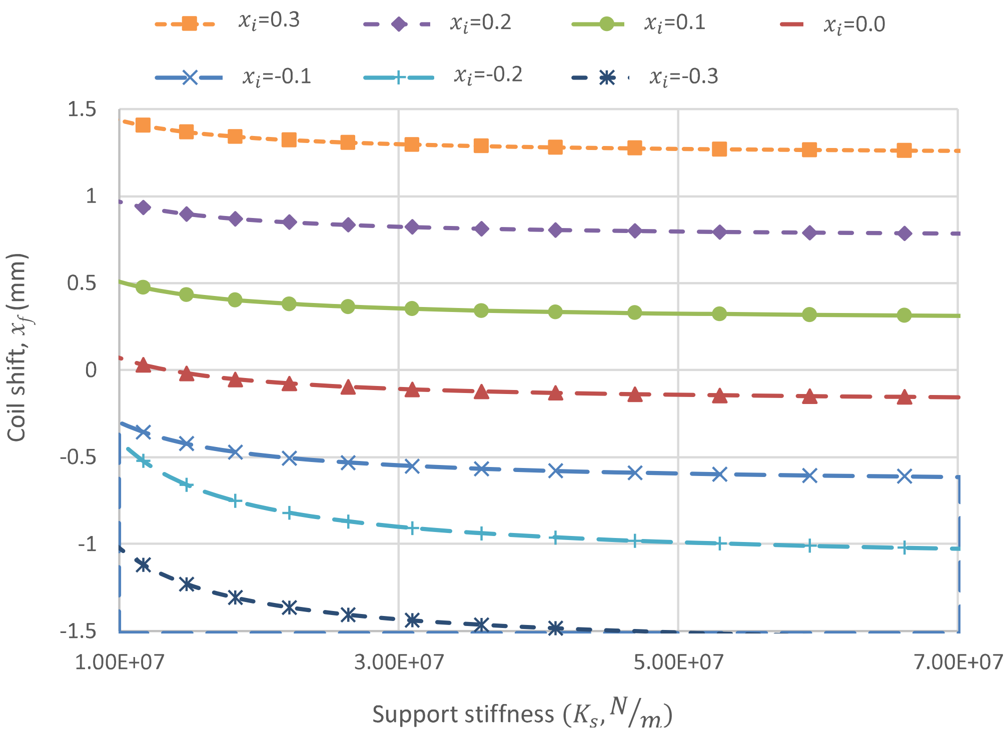

Figure 2.14 Effect of initial positioning (x_i) of the coil with respect to the center of the iron pole piece

2.6 Conclusion

The analytical solution presented here is used to study the coil support structure of a large aperture dipole magnet. It is noticed that the coil positioning accuracy can be obtained within ± 1 mm in all excitation levels. The coil needs to be initially aligned with an accuracy of ±0.2 mm to meet the final positioning requirement. It is also required to relax the support link tensions during cool-down of the magnet to keep support stresses within the allowable limit of the material. This methodology has the potential for application to other geometries of the magnets. Extensive study has been carried out for the superconducting solenoid magnet and is presented in Chapter 3.

Chapter 3
Support system for solenoid magnet

Chapter 3

3. Support System for Solenoid Magnet

Superconducting solenoid magnets are in use in various devices, such as accelerator magnets, MRI, tokamaks, and so on. Solenoid magnets, being symmetric, have unique advantages over other shapes. They are easy to design, as magnetic forces can be balanced for its inherent symmetries. Moreover, the magnetic field accuracies are also more comfortable to obtain and easy to build. The support structures of the solenoid magnets are also relatively more straightforward because of its symmetric coil structure. Support links are one of the most used support systems for the solenoid magnets [14], however, several other kinds of support systems are also designed.

3.1 Support links for solenoid magnet

In general, the solenoid magnet coils are symmetrical with an iron pole and yoke. Typical geometry of a solenoid is shown in Figure 3.1. The coils are wound around a bobbin, which acts like a liquid helium chamber and support links hang it from an outer vacuum chamber (not shown in the figure).

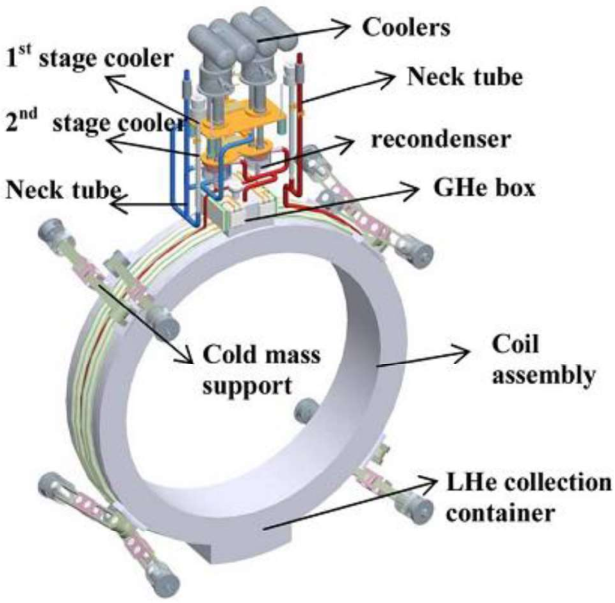

Figure 3.1 Typical geometry of a superconducting solenoid magnet [50]

3.2 Support links of superconducting cyclotron magnet

The main magnet of Superconducting cyclotron at VECC is a 1.42 m diameter [51] warm bore superconducting solenoid magnet having 80 T magnet iron around it [52]. The magnet cryostat houses a superconducting Nb-Ti coil at liquid helium temperature (4.5 K). The coil is wound on a stainless-steel bobbin. The bobbin is closed by welding an outer wall to it, forming a closed liquid helium chamber. The bobbin is supported by nine support links inside the outer vacuum chamber – six vertical (three each in upper and lower side and three horizontal [Figure 3.2]. All the vertical support links [Figure 3.3] are identical in length, while one out of three horizontal support links [Figure 3.4] is shorter in length. One end of the support links is fixed to the liquid helium chamber while the other end is attached to the outer vacuum chamber. There is an intermediate liquid nitrogen shield intercept connected to each support links. The material of the support links is glass-epoxy. Vertical supports are numbered as #1 to # 6, and horizontal supports are number as #7 to #9 respectively. The individual support numbers are used where each support link force vary between them.

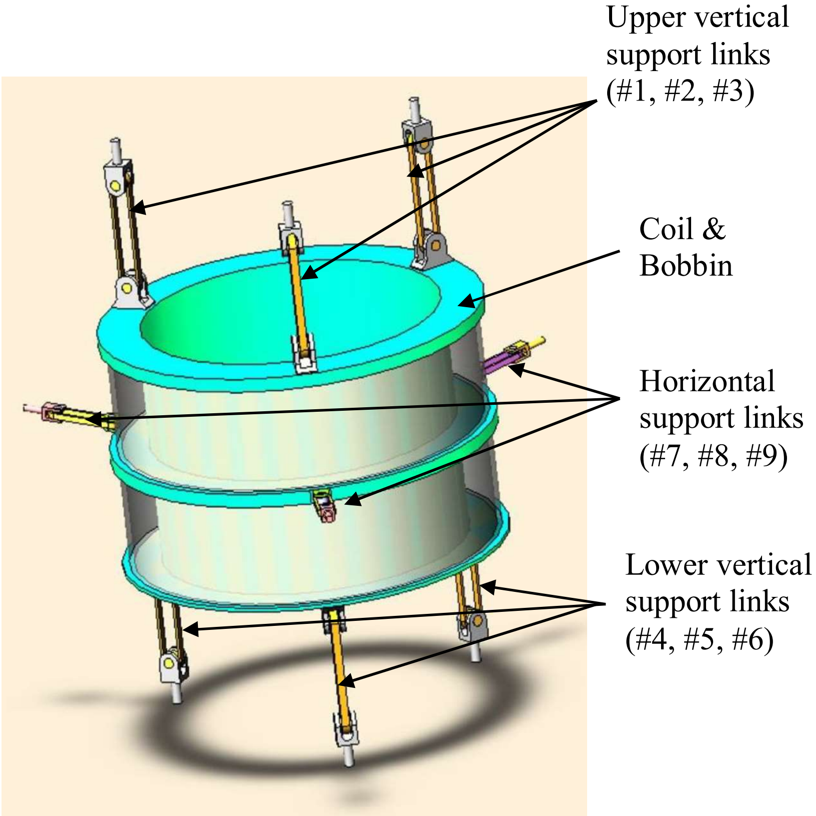

Figure 3.2 Coil support system for the superconducting cyclotron, showing upper, lower vertical support links and horizontal support links.

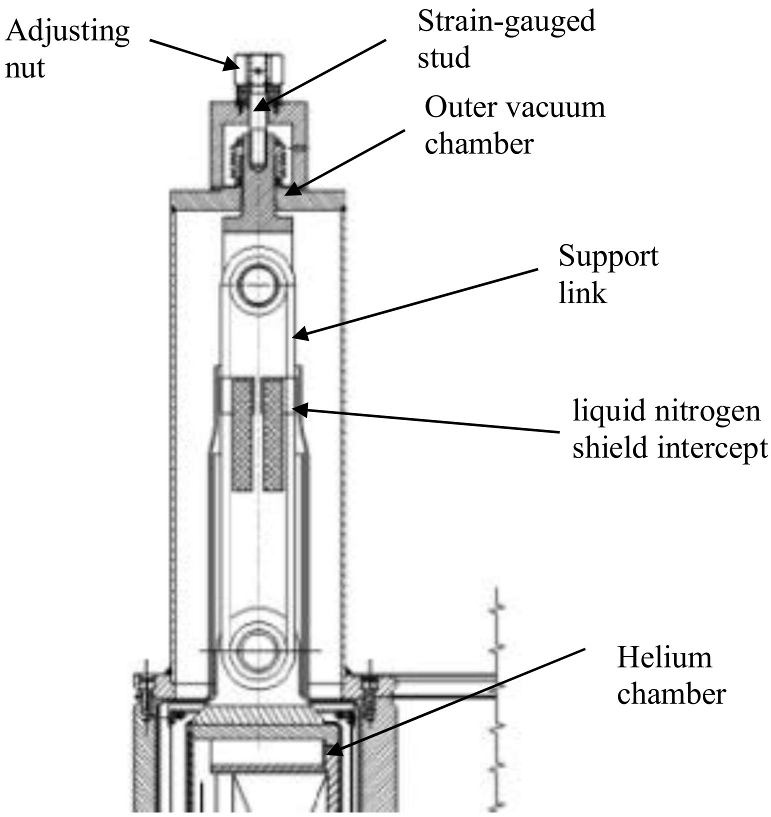

Figure 3.3 Vertical support link

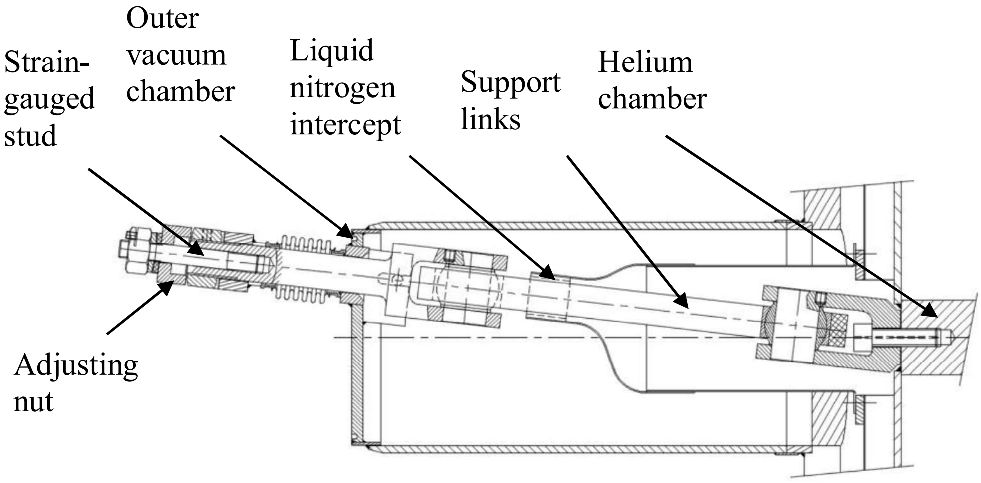

Figure 3.4 Horizontal support link

Both the horizontal and vertical support links have an adjusting nut connected to the warm end to loosen or tighten the support as and when required.

3.3 An analytical model for a support system for solenoid magnet

A general free body diagram of the coil with its support links is shown in Figure 3.5 (a) and (b). The cold-mass (coil and its bobbin) along with the support links contract during cool-down and manifest as forces in the support links. The coil may also move from its room temperature position if the coil or its support structure is not symmetric [53].

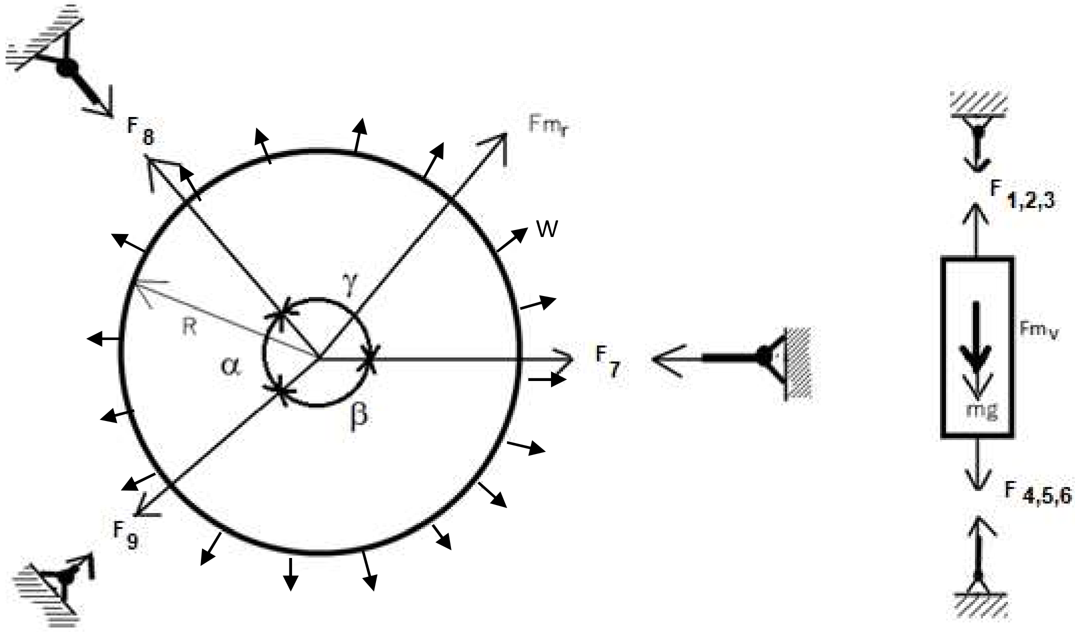

(a) (b)

Figure 3.5 The free body diagram of the solenoid coil along with the (a) horizontal and (b) vertical support links

The Lorentz force (w) on the coil is always symmetric for a solenoid magnet and hence would be balanced in all condition. However, in iron core solenoid magnets, the force due to iron can produce a resultant force on the coil (F_m) due to any vertical or radial asymmetry in the system. The asymmetry can come due to iron shape, coil position in the iron, due to initial alignment error or thermal movement, etc. The magnetic force on solenoid will have radial and vertical component, while any azimuthal component may be ignored due to inherent symmetry. The cold-mass can be supported by n number of support links, while it is necessary to have at least three horizontal support links, three upper vertical support links and three lower vertical support links to restrict all six degrees of freedoms.

The vertical support links have to take the weight of the cold-mass (*mg*) along with the resultant vertical magnetic force (Fm_v) if any due to the vertical coil shift. The horizontal supports provide rigidity against the resultant radial magnetic force (Fm_r). There is also load due to thermal contraction acting on the support links, as the magnet coil is cooled down to cryogenic temperature for its operation.

It is seen from Figure 3.5 that the system of force is indeterminate. The method of force is applied to find enough equations for the equilibrium condition.

The assumptions are:

1. The coil is cooled to its operating temperature (e.g., liquid helium temperature), and the temperature is uniform throughout the coil.
2. All stresses are within the elastic limit of the materials
3. Horizontal links always remain horizontal, and vertical links remain vertical.
4. All stresses are within elastic limit, so the principle of superposition is used for thermal and magnet stresses.

3.3.1 A thermal model of support links for solenoid magnet

In general, the support links are made of low thermal conducting materials, like glass–epoxy, CFRP, Ti and Ti alloys, etc. [7] [11] [12] [13]. One ends of the support links are fixed with the outer vacuum chamber, which always remains at room temperature (about 300 K). Whereas the other ends are hinged with the bobbin at 4 K. In between two ends of the support links, liquid nitrogen/helium gas cooled thermal shields are attached for heat interception. A typical support link configuration is schematically shown in Figure 3.6.

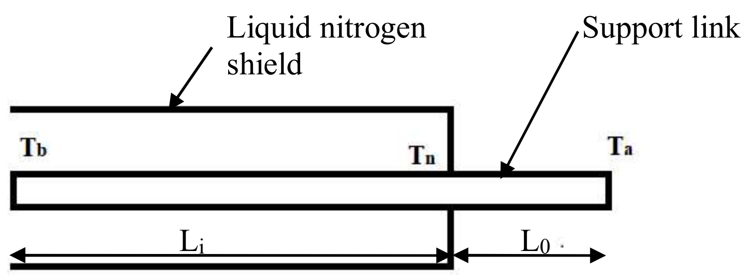

Figure 3.6 Schematic diagram of the support link

The temperature distribution in support links varies along the length L_i and L_o in two different steps. For simplifying the calculation, linear temperature distributions are assumed for L_i and L_o length of support links as shown in Figure 3.7.

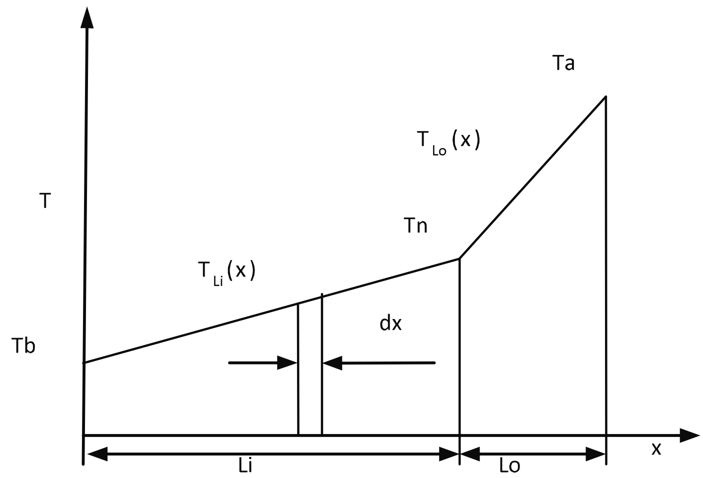

Figure 3.7 Temperature distribution along the support links. T_a is the ambient temperature, T_b is the cold-mass temperature and T_n is the intercept temperature

The following equations can represent the temperature distribution along the length of support link:

$$T_{Li}(x) = \frac{(T_n - T_b)x}{L_i} + T_b, \quad (0 \leq x \leq L_i) \quad .... 3.1$$

$$T_{Lo}(x) = \frac{(T_a - T_n)x}{L_o - L_i} + T_n, \quad (L_i \leq x \leq L_o) \quad .... 3.2$$

Contraction of support links length due to temperature decrease:

$$\Delta L_k = \int_0^{L_i} \alpha_s(T) \left(T_{L_i}(x) - T_b \right) dx + \int_{L_i}^{L_o} \alpha_s(T) \left(T_a - T_{L_o}(x) \right) dx$$

…. 3.3

Contractions of mean radius and height of the bobbin due to temperature decrease is given by:

$$\Delta R_b = R_b \int_{T_a}^{T_b} \alpha_b(T) dT \quad .... 3.4$$

$$\Delta H_b = H_b \int_{T_a}^{T_b} \alpha_b(T) dT \quad .... 3.5$$

3.3.1.1 Horizontal Support Link

The horizontal support links are fixed with the outer periphery of the bobbin at 120° apart from each other, shown in Figure 3.8 (a).

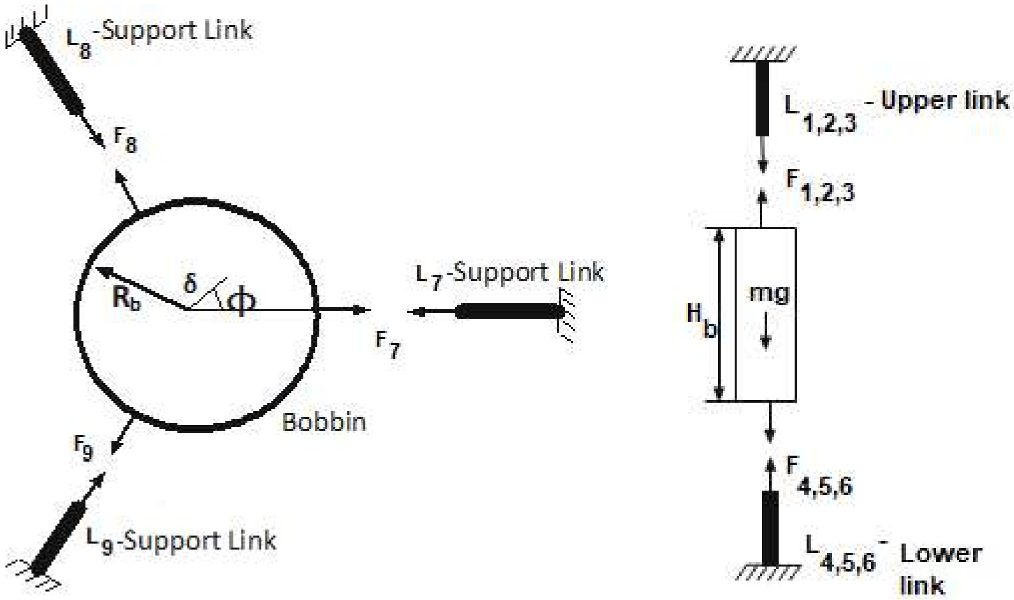

(a) (b)

Figure 3.8 Freebody diagram of the bobbin (a) with horizontal support links, (b) with vertical support links

Change in support link length due to the thermal force is given by (where k=1,2,…,9):

$$\Delta L_k' = F_k \frac{L_k}{A_{sk}\, E_s} \quad \ldots.\ 3.6$$

Change in bobbin mean radius due to thermal force is given by (where k = 7,8,9):

$$\Delta R_b' = F_k\, K_b \quad \ldots.\ 3.7$$

The stiffness of bobbin against horizontal support link force may be calculated (refer Annexure 2 for details) and found to be:

$$K_b = \frac{2\, R_b^3}{E_b\, I_b} \int_0^{\frac{\pi}{3}} [R_c(1 - cos\,\theta) + R_r\ sin\,\theta]^2\, d\theta \quad \ldots.\ 3.8$$

Where,

$$R_c = \frac{\int_0^{\frac{\pi}{3}} (1 - \cos\theta - \sqrt{3}\ \sin\theta)\ \sin\theta\ d\theta}{\int_0^{\frac{\pi}{3}} (1 - \cos\theta - \sqrt{3}\ \sin\theta)^2}$$

$$\text{and, } R_r = 1 - \sqrt{3}\, R_c$$

Therefore, for three horizontal support links at the equilibrium condition, the following equations are true:

$$\frac{F_7}{\sin\alpha} = \frac{F_8}{\sin\beta} = \frac{F_9}{\sin\gamma} \quad \text{.... 3.9}$$

$$d\ cos\phi\ =\ \Delta L_7\ +\ \Delta R_b - F_7\ (\frac{L_7}{A_{s7}E_s}\ +\ K_b) \quad \text{.... 3.10}$$

$$d\ cos\ (120\ +\ \phi)\ =\ \Delta L_8\ +\ \Delta R_b - F_8\ (\frac{L_8}{A_{s8}E_s}\ +\ K_b) \quad \text{.... 3.11}$$

$$d\ cos\ (240\ +\ \phi)\ =\ \Delta L_9\ +\ \Delta R_b - F_9\ (\frac{L_9}{A_9E_s}\ +\ K_b) \quad \text{.... 3.12}$$

Equation 3.9 comes from the equilibrium of force. Equation 3.10, 3.11 and 3.12 is deformation balance equations for three support links. From these four equations, 3.9, 3.10, 3.11, 3.12, the horizontal link forces (F_7, F_8, F_9), the shift of the coil center (d) and the direction of shift (ϕ) can be determined by iteration.

Another method for finding out the same equations in a different form is using Castigliano's theorem, as shown in Chapter 2. The complementary potential energy of the system can be written as:

$$U^* = \frac{F_7^2\left(\frac{1}{K_7} + K_b\right)}{2} + \frac{F_8^2\left(\frac{1}{K_8} + K_b\right)}{2} + \frac{F_9^2\left(\frac{1}{K_9} + K_b\right)}{2}$$

Now, the deformation of the system is given by:

$$\delta = \frac{\partial U^*}{\partial F_7} = F_7\left(\frac{1}{K_7} + K_b\right) + F_8\left(\frac{1}{K_8} + K_b\right) + F_9\left(\frac{1}{K_9} + K_b\right)$$

Here, it is assumed that:

$$\frac{\partial F_8}{\partial F_7} = \frac{\partial F_9}{\partial F_7} = 1$$

Where δ is equal to the total thermal deformation of the system at the supports, i.e.

$$\delta = \Delta L_7 + \Delta R_b + \Delta L_8 + \Delta R_b + \Delta L_9 + \Delta R_b$$

We can therefore write,

$$F_7\left(\frac{1}{K_7} + K_b\right) + F_8\left(\frac{1}{K_8} + K_b\right) + F_9\left(\frac{1}{K_9} + K_b\right) = \Delta L_7 + \Delta L_8 + \Delta L_9 + 3\,\Delta R_b \quad \text{.... 3.13}$$

Solving equations 3.9 (two equations) and 3.13, we can also find out F_7, F_8, and F_9.

3.3.1.2 Vertical Support Link

It is assumed that the upper three vertical support links equally share the total weight of the bobbin. During cool-down, a thermal force will develop in vertical support links and bobbin along its longitudinal direction, due to shrinkage in length with decreasing temperature shown in [Figure 3.8 (b)].

Therefore, the total load during cool-down in the upper support link #1, #2 and #3 can be determined by:

$$F_{1,2,3} = \frac{(\Delta H_b + 2\,\Delta L_{1,2,3})}{\left(\frac{H_b}{A_b E_b} + \frac{2\,L_{1,2,3}}{A_{S1,2,3}\,E_S}\right)} + mg/3 \quad \text{... 3.14}$$

$$F_{4,5,6} = \frac{(\Delta H_b + 2\,\Delta L_{4,5,6})}{\left(\frac{H_b}{A_b E_b} + \frac{2\,L_{4,5,6}}{A_{S4,5,6}\,E_S}\right)} \quad \text{... 3.15}$$

3.3.2 FEM Analysis

A detail 3-D finite element analysis was carried out using ANSYS [45] for finding out temperature distribution, support stress, and coil movement. The temperature distribution on support links and bobbin was determined in the first step by thermal analysis. The force and deformation were found out in the second step by coupling the thermal results into the structural analysis.

In thermal analysis, the convection heat load is neglected, as the support links are located inside the vacuum chamber. The room temperature end of the support links is always maintained at ambient temperature (300 K), and the other end temperature is reduced to 4 K during cool-down. It is assumed that the temperature of the thermal shield is maintained at a temperature of 100 K. Temperature-dependent material properties were used for this analysis [47] [54].

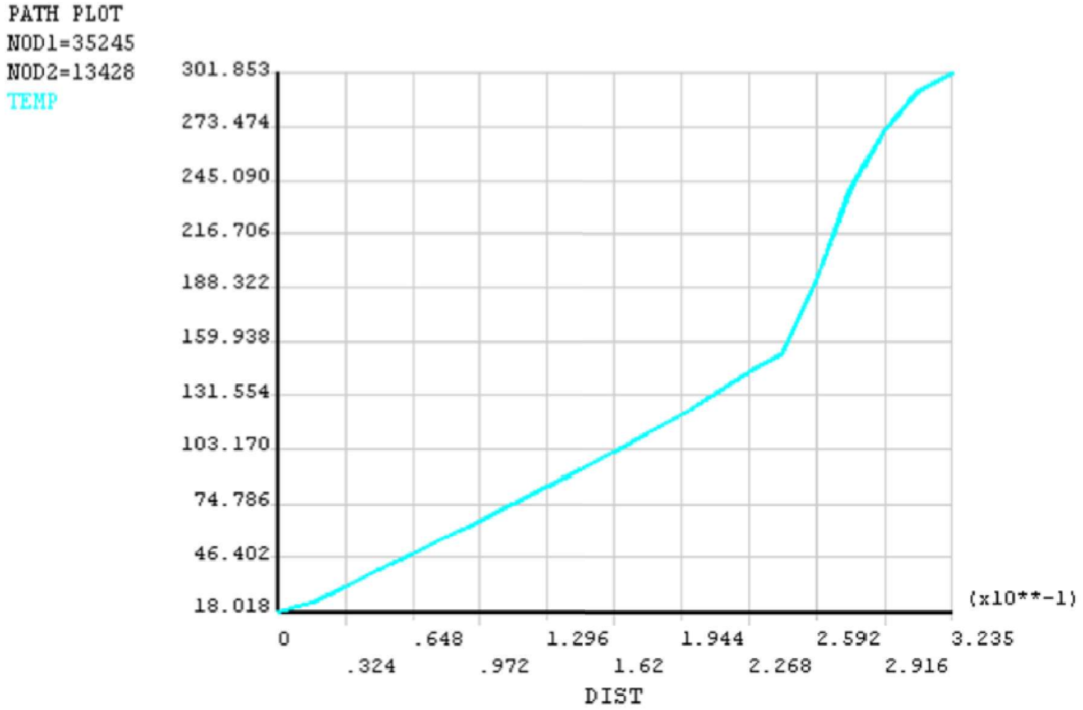

Figure 3.9 Temperature distribution along the length of support link determined using ANSYS

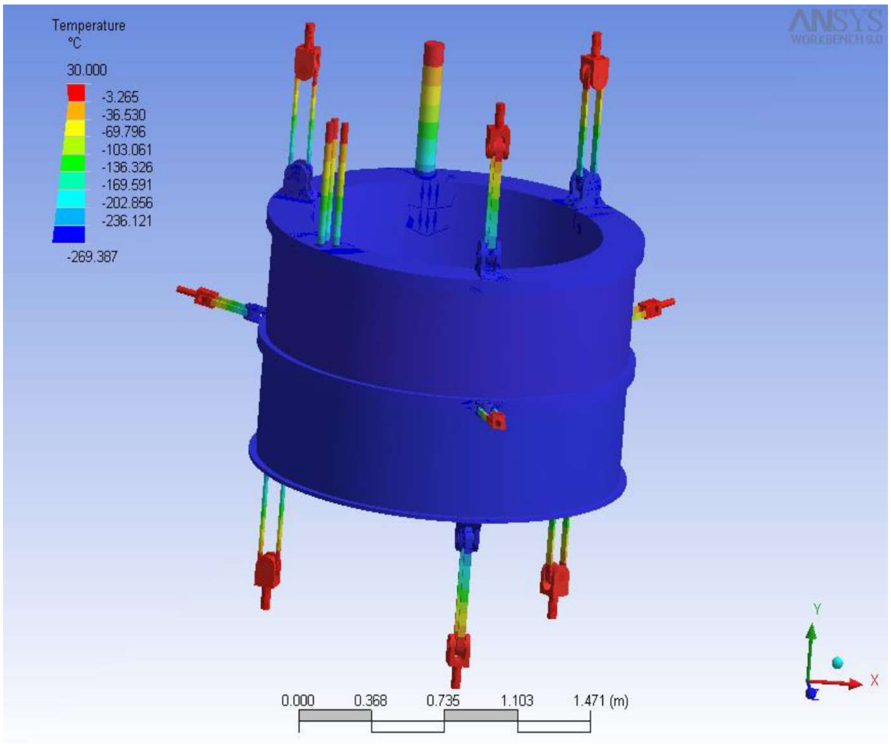

Figure 3.10 Contour plot of the temperature distribution after cool-down

The temperature distribution was determined using ANSYS [45] and is plotted along the length of support links as shown in Figure 3.9. A contour plot of the temperature distribution is also shown in Figure 3.10. In the subsequent structural analysis, earth gravity was considered to include the effect of the weight of the bobbin assembly. The reaction forces on all support links and deformation in bobbin assembly were found out after the post-processing of the results.

3.3.3 Support force measurement system

The warm end of each support links is equipped with a strain-gauged stud to measure the strain in the support links. The specifications of the strain-gauged studs are ST-FB 5/8″ - 11 NC x 5″ (120 ohm/200 °F) and ST-FB 1″ - 8 NC x 7″ (120 ohm/200 °F) [55] for horizontal and vertical support links respectively. The rated load for horizontal studs is 6800 kgf (15000 lbf), and vertical studs are 20400 kg (45000 lbf). These studs were calibrated by Strainsert Dead Weight Calibration Device and were certified by M/s Strainsert. The strains are measured with model 6100 scanner. The strain reading can be converted into force using the calibration factor and assuming a linear relationship between strain and force. The specified non-linearity of the gauges is ± 1% of the allowable load, and non-repetition is ± 0.1% of F.S.

The coil was equipped with silicone diode temperature sensors. During the cooldown of the magnet, the temperature of the coil and the support link forces were recorded.

3.3.4 Results of the analysis and comparison with experimental data

Equations 3.9 to 3.12 and equation 3.13 were solved considering the geometry of the coil structure for K500 superconducting cyclotron. Temperature-dependent material properties were used in the analysis. The forces developed in horizontal and vertical support link were calculated with decreasing the bobbin temperature and is shown in Figure 3.11.

From Figure 3.11, it can be found that the maximum horizontal and vertical support link forces may rise to 9.849 x 10^4 N and 10.1 x 10^4 N during cool-down. The allowable load for horizontal support links is 6.8 x 10^4 N (6800 kgf), smaller than the maximum calculated force. Therefore, the horizontal support links needed adjustment (loosened) during cool-down to protect them from breakage. However, the vertical support links required no change since the allowable load for vertical support links is 20.4 x 10^4 N (20400 kgf), much higher than the calculated force.

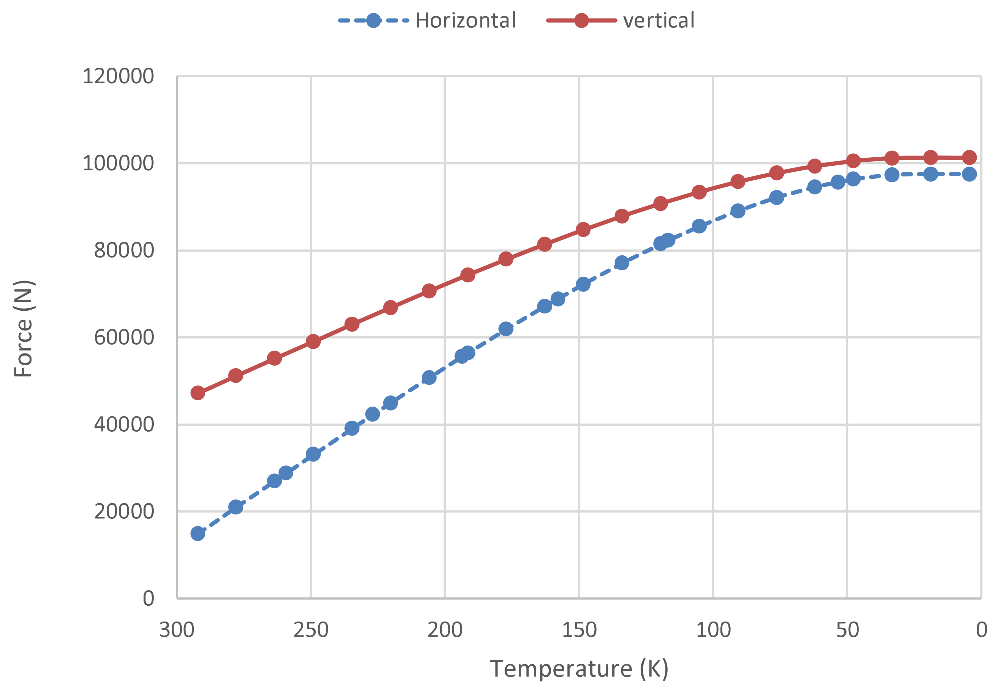

Figure 3.11 Analytically calculated forces in horizontal (#7, #8, #9) and vertical support links (#1, #2, #3)

The maximum and minimum load limits used during the operation, for horizontal support links, was kept as 3 x 10^4 N and 1.5 x10^4 N respectively. An empirical relation [Figure 3.12] was obtained keeping the force limits and considering full adjustments (i.e., after each adjustment, near minimum load in supports are achieved), which is represented by the following equation:

$$\mathrm{F_k(T)} = 3 \times 10^{-10}\ \mathrm{T_6} - 2 \times 10^{-7}\ \mathrm{T_5} + 9 \times 10^{-5}\ \mathrm{T_4} - 0.011\ \mathrm{T_3} - 0.980\ \mathrm{T_2} + 41058\ \mathrm{T} + 97320$$

$$(\text{for } 1.5 \text{ x } 10^4 \text{ N} < F_k < 3 \text{ x } 10^4 \text{ N}) \qquad \text{.... } 3.16$$

The horizontal support link forces are derived as a function of temperature from the equation 3.14 for different adjustments considering the load limits and are plotted in

Figure 3.12. It shows that six full adjustments (loosening) are necessary at 260 K, 225 K, 190 K, 160 K, 115 K and 55 K temperature. The measured forces in the horizontal support link are also plotted in the same figure.

It can be seen from the experimentally measured data in Figure 3.12 that five full and two half (total six full) adjustments were necessary for the horizontal support links during its cooldown. The half adjustments were given early to avoid the inconvenient timing of adjustment.

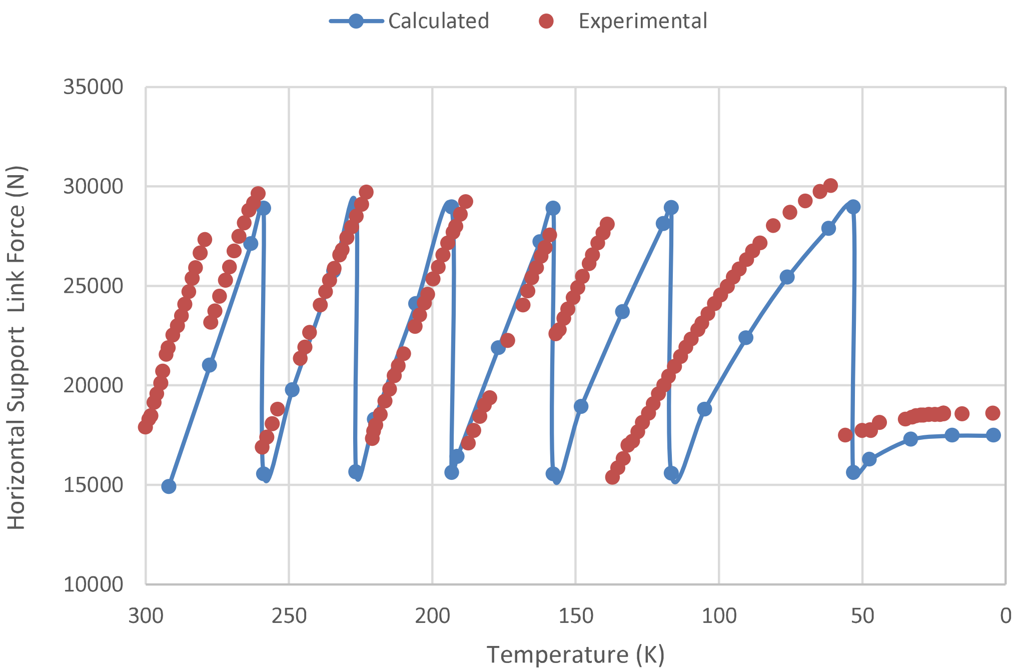

Figure 3.12 Comparison of calculated horizontal support link force (#7) with measured data of #7 support link

It the figure, there is a difference between calculated and measured force values at the starting point. This difference is because of the pre-stress in the support links, and the initial value of the horizontal support link force was 1.8 x 10^4 N instead 1.5 x 10^4 N. Figure 3.13 shows the comparison between calculated and measured values of upper vertical support link force during cool-down. The initial values do not match well, which may be due to an error in measured data or FEM results as the contraction values are minimal at a higher temperature.

Since one of the horizontal support links is shorter in length than the other two, the center of the coil will also shift during cool-down, in the direction of short support link because of its higher rigidity. Figure 3.14 shows the movement of the coil center with decreasing temperature of the bobbin. It can be seen from the figure that the center of the coil would shift by 0.384 mm when the coil reaches at 4.5 K temperature.

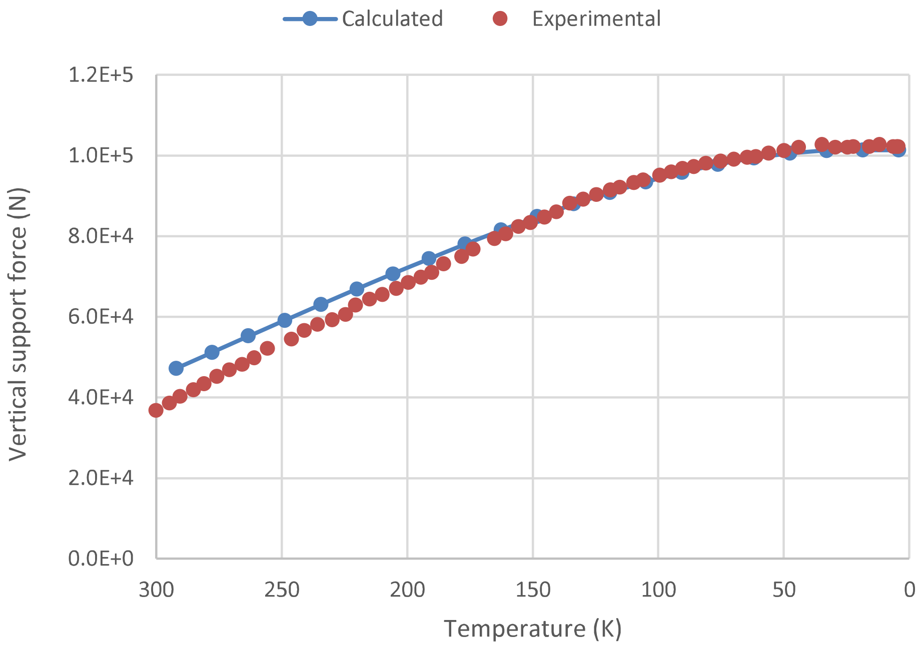

Figure 3.13 Comparison of calculated upper vertical link force (#1, #2, #3) with measured data

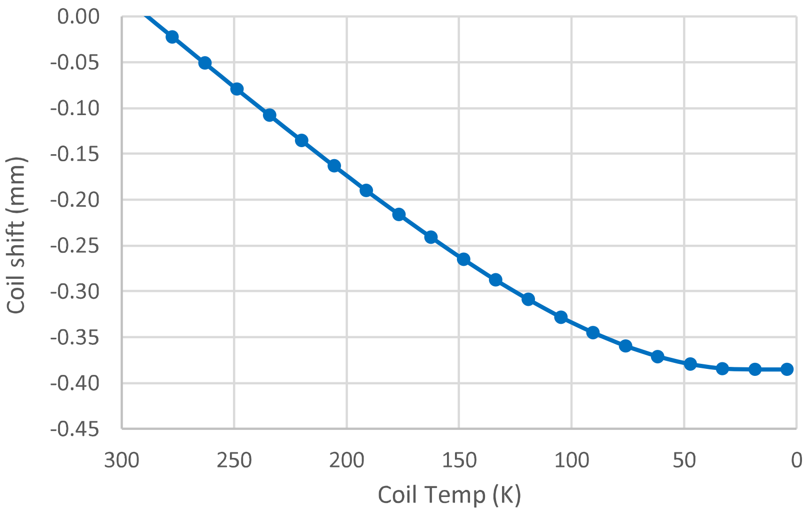

Figure 3.14 Shift of the coil center with decreasing temperature

The analytical, ANSYS results and measured data for support links force and shift of coil center are compared in Table 2. The ANSYS model considered the same loading conditions and same assumptions that are used in the analytical study, i.e. (a) temperature of the coil has reached coil operating temperature (e.g., liquid helium temperature) and uniform throughout the coil, (b) the horizontal links remain horizontal, and the vertical links remain vertical. All the boundary conditions are applied accordingly. It may be noted that measured data for horizontal support links shown are cumulative forces measured before each adjustment during cool-down. It may also be noted that it was not possible to know the shift of the center of the coil as there were no measurements available for it.

Table 2: Comparison of analytical and ANSYS results with measured data

Parameter (Unit)	**Analytical (1-D model)**	**ANSYS (3-D model)**	**Measured data**
Horizontal Link force (N) (#7, #8, #9)	9.849×10^4 9.849×10^4 9.844×10^4	12.6×10^4 12.5×10^4 13.5×10^4	9.44×10^4 9.22×10^4 8.18×10^4
Vertical Link force (N) (#1, #2, #3)	1.01×10^5	10.2×10^4 10.4×10^4 9.59×10^4	10.2×10^4 11.4×10^4 9.95×10^4
Shift of coil center (mm)	-0.384	-0.379	–

3.4 Magnetic force and coil centering

In a solenoid magnet, the magnetic force (Lorentz force) in the coil is always balanced because of the inherent symmetry in coil structure. However, in the case of the iron core magnet, magnetic interaction between the iron yoke and coil takes place. The axial and radial placement of the coil with respect to the iron results magnetic forces between them [56] that varies with the radial as well as the axial shift from the symmetry plane [57]. The coil must be well centered with respect to the outer yoke to eliminate the asymmetry force and to avoid magnetic field imperfections [58].

The Lorentz force in the coil results in radial expansion of the coil due to magnetic hoop stress and the radial support link forces uniformly decrease with the current. The unbalanced radial force due to coil shift is generated by $\overrightarrow{J_\theta} \times \overrightarrow{B_z}$ interaction and is directed towards a radial direction. The radial force is unstable and extremely large at higher current. This may result in uncontrolled deformation of the supports and can damage to the cryostat and the coil [59]. The vertical axial force generated by a radial component of the magnetic field is stable and it comes out to be small relative to the radial force.

3.4.1 Magnetic force on the coil

The resultant magnetic force on coil varies with the shift of the coil from the axis and is a function of current. In this discussion, let us take into consideration that the coil has a shift in the radial direction for an iron core solenoid.

The interaction of iron and the coil may be calculated by image-current method. Figure 3.15 shows the model used for a general solenoid magnet with iron pole and yoke. It is assumed that the poles have become saturated, which is true for all high field superconducting magnets, and do not produce any radial magnetic force on the coil.

3.4.1.1 An analytical model for finding out magnetic force on the coil

A model depicted in Figure 3.15 that is used to calculate the magnetic force on the superconducting coil.

The dipole moment of the coil,

$$\overrightarrow{M_c} = N.\vec{I}.\pi a_p^2$$

The dipole moment of the image coils,

$$\vec{M} = \overrightarrow{M_c}$$

The magnetic field at any point P from the center of the coil [60] in a spherical coordinate system (shown in Figure 3.16) for $r^2 >> a_p^2$ is given by:

$$\overrightarrow{B_r} = \frac{\mu_0}{4\pi} \cdot \frac{2\,\overrightarrow{M_c}}{r^3} \cos\theta$$

$$\overrightarrow{B_\theta} = \left(\frac{\mu_0}{4\pi}\right) \cdot \frac{\overrightarrow{M_c}}{r^3} . \sin\theta$$

$$B_\phi = 0$$

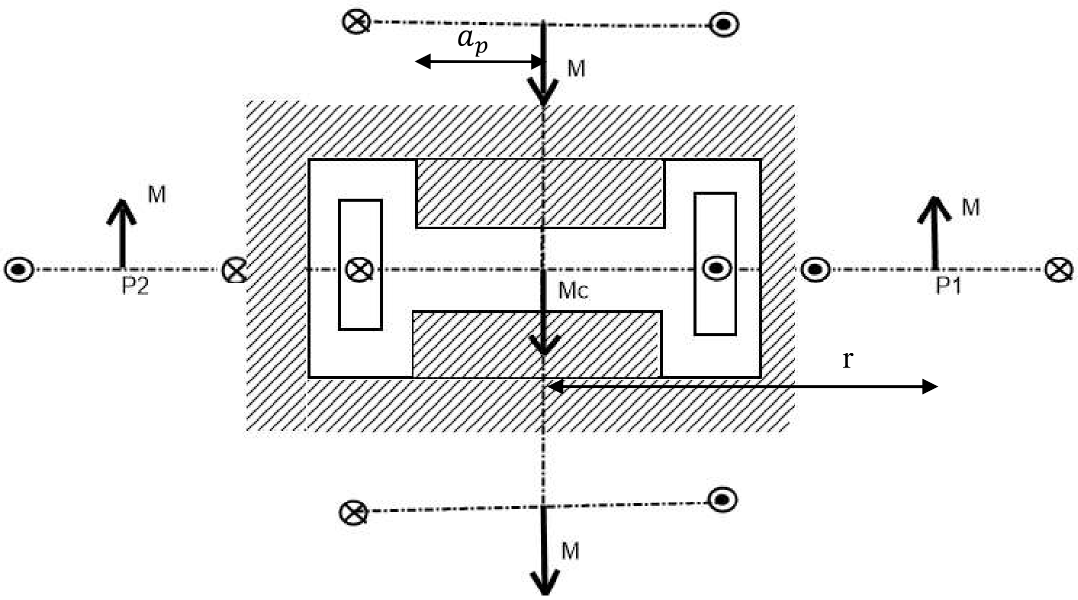

Figure 3.15 Image current model for an iron core solenoid magnet

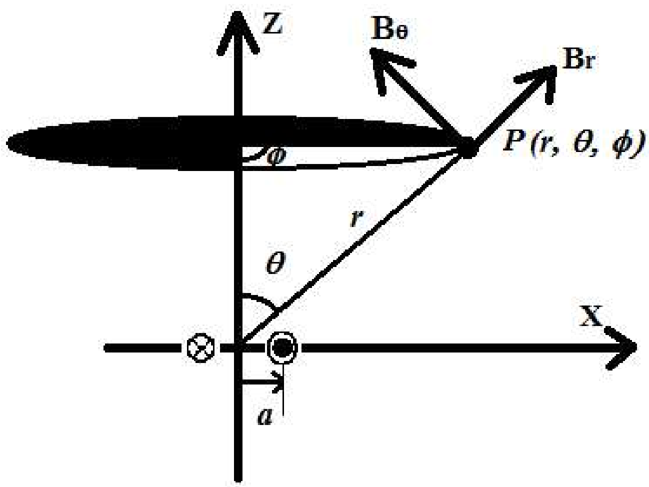

Figure 3.16 Co-ordinate system and variables used for the magnet

For the image-coil at right in Figure 3.15 the magnetic field at its center (point P1) is given by:

$$\theta = 90°, \overrightarrow{B_r} = 0, \overrightarrow{B_\theta} = \frac{\mu_0}{4\pi} . \frac{\overrightarrow{M_c}}{r^3} = \overrightarrow{B_z}$$

The magnitude of the force on the right-side image coil is given by:

$$F_L = |\nabla(\vec{M} \cdot \vec{B})| = |M|.|\frac{\partial B_z}{\partial r}| = -\frac{\mu_0}{4\pi} . \frac{3\, M_c^2}{r^4}$$

The magnitude of the force on the left-side image coil at its center (point P2) is given by:

$$F_R = -\frac{\mu_0}{4\pi}\cdot\frac{3\,M_c^2}{(r+\Delta r)^4}$$

Where the distance from image coil is $r + \Delta r$, i.e., the left side image coil is placed Δr distance apart than the right-side image coil from the center of the coil.

The net force on the image coils or the iron is

$$F_i = F_L - F_R = -\frac{\mu_0}{4\pi}.\frac{12\,M_c^2}{r^5}.\Delta r$$

The force exerted by the iron on the coil is thus

$$F = -F_i = \frac{\mu_0}{4\pi}.\frac{12\,M_c^2}{r^5}.\Delta r$$

Hence, the force exerted on the coil by the iron is given by,

$$F_m = \frac{\mu_0}{4\pi}.\frac{12\,M_c^2}{r^5}.\Delta r$$

This equation was not used here to calculate the magnetic force due to substantial variation found in magnetic force value by this equation and the measurements.

3.4.1.2 An alternate way of calculation of magnetic force on the coil

The radial Lorentz force per unit perimeter of the coil is calculated considering a uniform current density ($\overrightarrow{J_\theta}$) in the solenoid and integrating $\overrightarrow{B_z}$, the axial component of the magnetic field, over the cross-section of the coil, as shown below.

$$w = J_\theta \int_r \int_z B_z[r,z]\, dr\, dz \quad \ldots.\ 3.17$$

The radial force due to coil-yoke interaction is directly related to the radial gradient of the Z component of the magnetic field at the coil region. The calculated field gradient is taken from the magnetic analysis code (POISSON) for the K-500 main magnet configuration. As the Δr is infinitesimally small, the radial outward force is approximated by [57],

$$F_m = 4\pi\,\Delta r \int_r \int_z J_\theta \frac{\partial B_z[r,z]}{\partial r}\, r\, dr\, dz \qquad \ldots.\ 3.18$$

The integration is performed for the full cross-section of the coil.

3.5 An analytical model for calculating support forces

A model was developed for analyzing the effect of the magnetic force on support links. The forces on the support links will get reduced with the increase of current due to the expansion of the coil and bobbin under the Lorentz force. The coil also sees the resultant magnetic force acting between the iron yoke and the coil and depending on the direction of the force; the support forces may increase or decrease due to this force.

The model made for analysis is shown in Figure 3.17 (a), where, w denotes the Lorentz force per unit perimeter of the coil and F_m denotes the resultant magnetic force acting on the coil due to yoke-coil interaction, while θ is the direction of the force F_m.

The assumptions are:

1. There is no coil offset in the vertical direction.
2. The vertical support links remain vertical, and horizontal support links remain horizontal, i.e., there is no interaction between the horizontal and vertical support link forces.
3. The deformations are less compared to the size of the coil.
4. The magnitude of the net magnetic force (F_m) acting on the coil is much less than the Lorentz force on the coil. Hence, the deformation of the coil under the F_m is neglected.
5. The system of horizontal supports acts as a couple linear system of a parallel concatenation of elements. [61]

In case of parallel spring system, the forces distributed in each of the springs can be calculated in several ways, (1) by solving the force and deformation balance equations, (2) minimization of the complementary potential energy of the system or (3) by minimizing the deformation of the system [61]. Method (2) and (3) are different forms of the same equation. A three-spring system is analyzed for comparison of the methods and is detailed in Annexure-5. Here you can see that the above three methods finally arrive at the same equations, even though the approaches are different. It may also be noted that method (2) and (3) are in general applicable to all systems with very small deformations and these methods are very much useful for analysis of complex systems where it is complicated to calculate the deformation balance required by method (1).

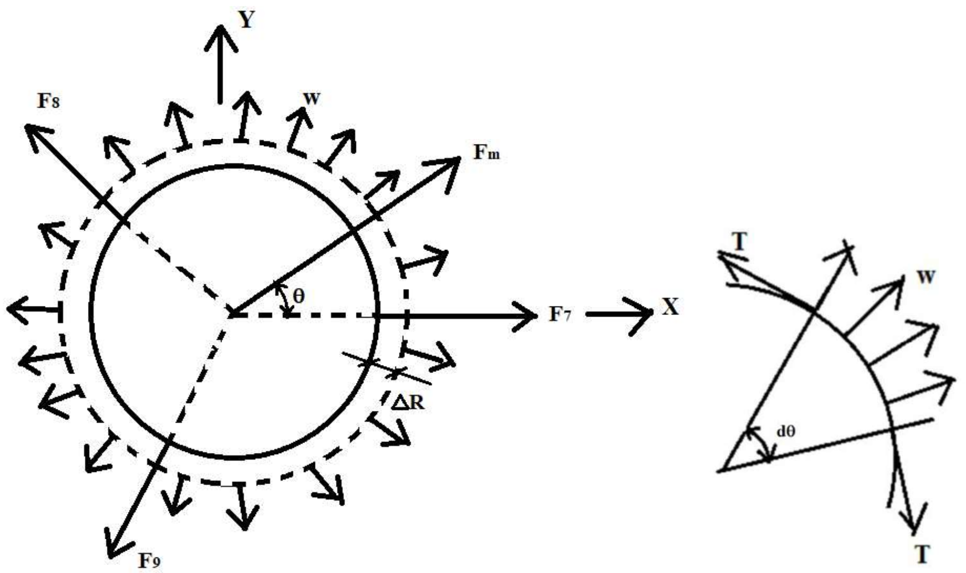

(a) (b)

Figure 3.17 (a) Analytical model for magnetic force on the coil, (b) a small azimuthal cut of the coil under Lorentz force w, T is the tensile force generated in the coil due to the Lorentz force in the coil

The force equilibrium equations for the model shown in Figure 3.17 (a) are given below:

$\sum F_x = 0$, i.e.

$$F_m \cos(\theta) + F_7 - F_8 \cos\left(\frac{\pi}{3}\right) - F_9 \cos\left(\frac{\pi}{3}\right) = 0$$

… 3.19

$\sum F_y = 0$, i.e.

$$F_m \sin(\theta) + F_8 \sin\left(\frac{\pi}{3}\right) - F_9 \sin\left(\frac{\pi}{3}\right) = 0$$

… 3.20

As the system of forces is indeterminate, the Castigliano's theorem [44] was used for finding out the third equation, as detailed in the following equations.

Complementary strain energy of the system is given by:

$$U^* = \frac{F_7^2}{2K_7} + \frac{F_8^2}{2K_8} + \frac{F_9^2}{2K_9} + \frac{2\pi R\, T^2}{2AE}$$

… 3.21

Where, K_7, K_8, K_9 are the support stiffnesses, A is the cross-sectional area of the bobbin and E is the Young's Modulus of the material of the bobbin and the coil. F_7, F_8 and F_9 are forces in the corresponding support link. T is the tensile force generated in the coil due to the Lorentz force in the coil.

Now, using Castigliano's 2nd theorem [44], we can write,

$$\frac{\partial U^*}{\partial F_7} = \frac{F_7}{K_7} + \frac{F_8}{K_8}\left(\frac{\partial F_8}{\partial F_7}\right) + \frac{F_9}{K_9}\left(\frac{\partial F_9}{\partial F_7}\right) + 2\pi \frac{TR}{AE}\left(\frac{\partial T}{\partial F_7}\right)$$

… 3.22

From Figure 3.17 (b), we can write,

$$T = wR$$

… 3.23

$$\Delta R = TR/AE$$

… 3.24

Where, R is the radius of the bobbin and ΔR is the deformation of the bobbin-coil assembly under Lorentz force.

It is now assumed that since F_7, F_8 and F_9 are at an angle $\frac{2\pi}{3}$ with each other and are at equilibrium. Therefore, it can be assumed that any small change in F_7 will cause equal changes in F_8 and F_9. So,

$$\frac{\partial F_8}{\partial F_7} = \frac{\partial F_9}{\partial F_7} = 1$$

… 3.25

It may also be assumed that the forces in $\frac{2\pi}{3}$ sector of the coil perimeter is completely transferred to the nearest support and we can write,

$$\left(\frac{2\pi R}{3}\right) w = F_7$$

… 3.26

Or, we can say from equation (3.23)

$$\frac{2\pi T}{3} = F_7$$

… 3.27

Therefore,

$$\frac{\partial T}{\partial F_7} = \frac{3}{2\pi}$$

… 3.28

Substituting equation (3.25) and (3.28) in equation (3.22), we can write,

$$\frac{\partial U^*}{\partial F_7} = \frac{F_7}{K_7} + \frac{F_8}{K_8} + \frac{F_9}{K_9} + \frac{3TR}{AE}$$

… 3.29

Now, using the extension of Castigliano's method developed by Clive L. Dym [61] applicable to any parallel concatenation of spring elements (details of derivation is explained with three parallel springs in Annexure-5), one can say,

$$\frac{\partial U^*}{\partial F_7} = 0$$

So, we can, therefore, write from equation (3.29),

$$\frac{F_7}{K_7} + \frac{F_8}{K_8} + \frac{F_9}{K_9} = -3\Delta R$$

… 3.30

The unknowns of the equations, F_7, F_8 & F_9 are solved using equations (3.19), (3.20) and (3.30) for finding out the support forces. The evolution of equations is detailed in Annexure 4.

3.6 Results of the analysis and comparison with measured data

The geometry of K500 superconducting cyclotron at Kolkata [62] and its support system was used for analysis. Magnetic forces, calculated by equation 3.17 and 3.18, were taken as input the problem. Equation 3.18 was solved assuming a coil shift (Δr) of 1 mm towards 0° with respect to the X-axis. Equations 3.19, 3.20 and 3.30 were solved to find out the support reaction forces (F_7, F_8 & F_9) in the three-support links. There were pre-stresses in the all the three-support links due to the initial tension and subsequent cool-down. The forces were being measured by the strain-gauges studs. When the measured pre-stress values were added with the calculated support forces (F_7, F_8 & F_9), the plot of the calculated support forces (F_7, F_8 & F_9) and the measured support forces vs. current in the coils looks like one shown in Figure 3.18. It can be clearly seen that the support force F_7 rises, while the calculated force drops, as F_m acts towards support #7. The support reaction forces do not match with the measured value by nature. The reason is very evident that the assumed direction of the magnetic force is not correct.

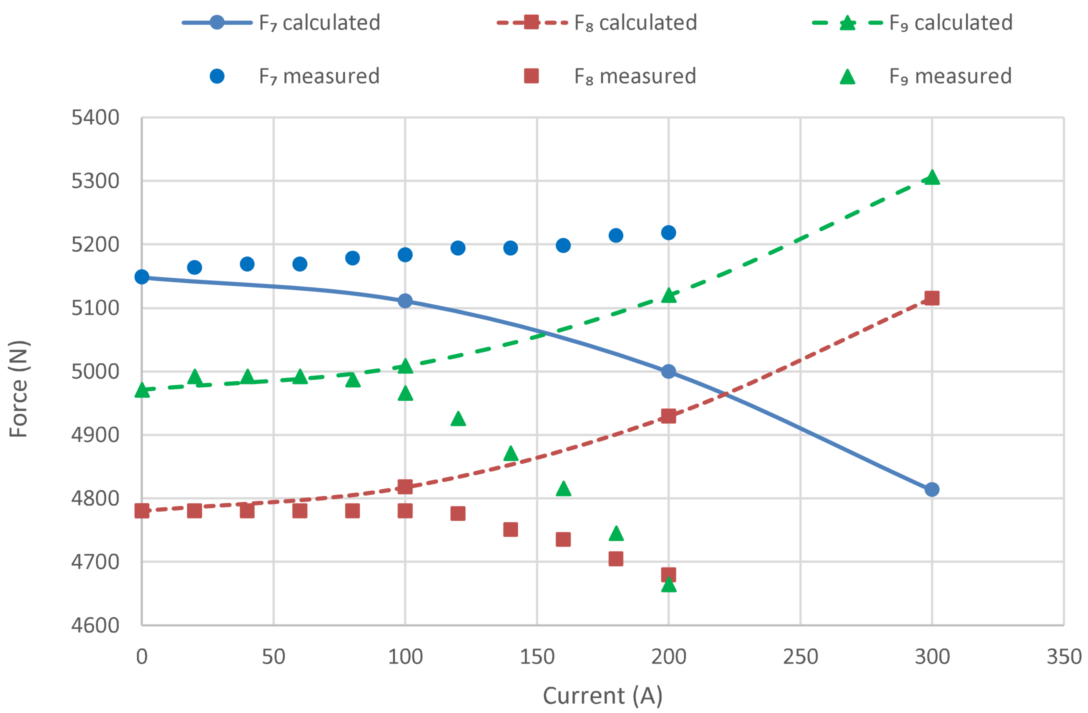

Figure 3.18 Horizontal link force at coil shift of 1 mm at 0° angle (anticlockwise from X-axis in Figure 3.17)

A few trials with the amplitude and angle of magnetic force, a plot could be generated as shown in Figure 3.19. With a coil shift of 1.2 mm at 210°, the variation of the calculated forces in the support links with current nicely resembled the variation measured.

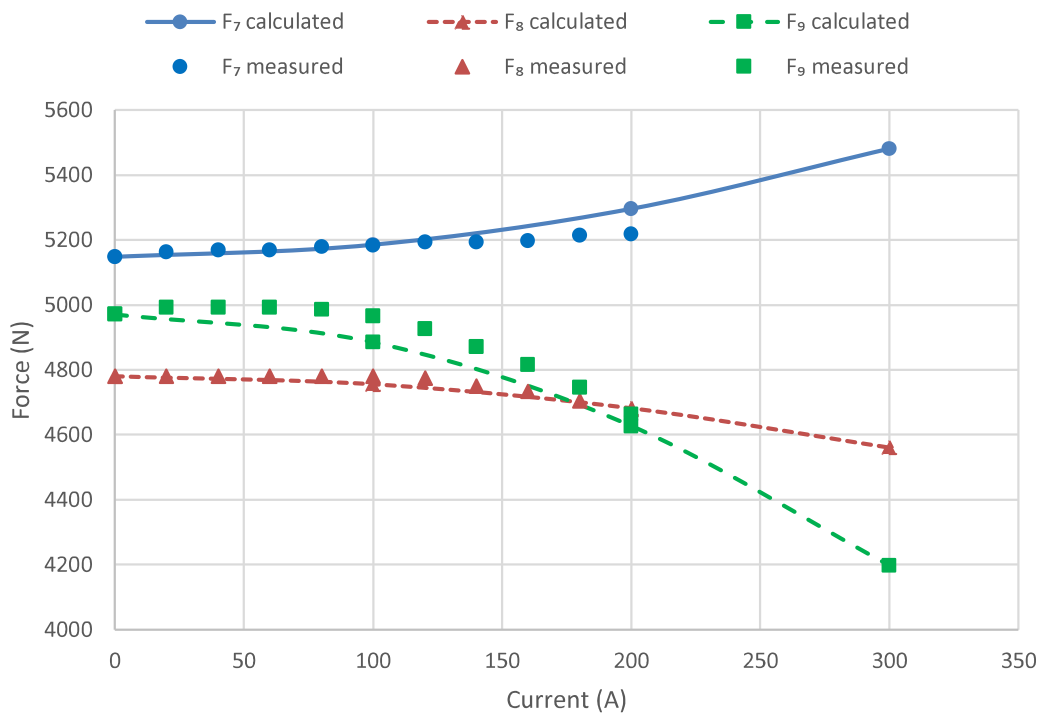

Figure 3.19 Horizontal link force for coil shift of 1.2 mm at 210° angle (anticlockwise from X-axis in Figure 3.17)

3.7 Coil centering

Some magnets, like superconducting cyclotron magnet at Variable Energy Cyclotron Centre, by design, are not stable under magnetic forces and may result in unrestricted movement of the coils if they are not correctly centered within the iron yoke [63]. The centering of the coils is thus an essential part of the design of the magnet as well as an important activity during the first energization of the magnet. P. Miller et al. [63] reported the coil centering of the K500 Magnet at Michigan State University by balancing forces in the support links. A trial-error method for coil centering was published by M. K. Dey et al. [49] for the Kolkata Superconducting Cyclotron Magnet. H. Blosser et al. [59] reported the failure of support link bolt in the K500 superconducting cyclotron magnet during energization. It has also been said that in superconducting magnets, the coil may move from its initial aligned position after cool-down due to asymmetry in the coil design or its support systems [53]. The actual location of the coil after cool-down is completely unknown as the initial positioning error adds up with the thermal movement of the coil and not measurable inside the welded outer vacuum chamber. It is, therefore, necessary to center the coil correctly inside the iron yoke to avoid failure of the support system under high magnetic force [59] as well as to achieve the required magnetic field accuracy [63]. L. Wang et al. reported [14] self-centering support system to avoid the coil shift during the cool-down process.

The rise of the measured support force F_7 and fall of the other two (F_8 &F_9) in Figure 3.19 indicate an initial coil shift. The calculated and measured forces are shown in Figure 3.19 that agrees with each other and predict a coil shift of about 1.2 mm at an angle of 210°.

The horizontal support link nuts were rotated to give movement to the coil so that the coil shift can be reduced. After each move, the values of support link forces with an increase in current were noted. After several movements, it was seen that the variation of force in the support link #7 almost became flat up to 450 A current, after which a rising trend was observed. This measured data of the experiment are plotted in Figure 3.20 along with the calculated force in support links for a coil shift of 0.8 mm towards 210°. The calculated results closely follow the measured values.

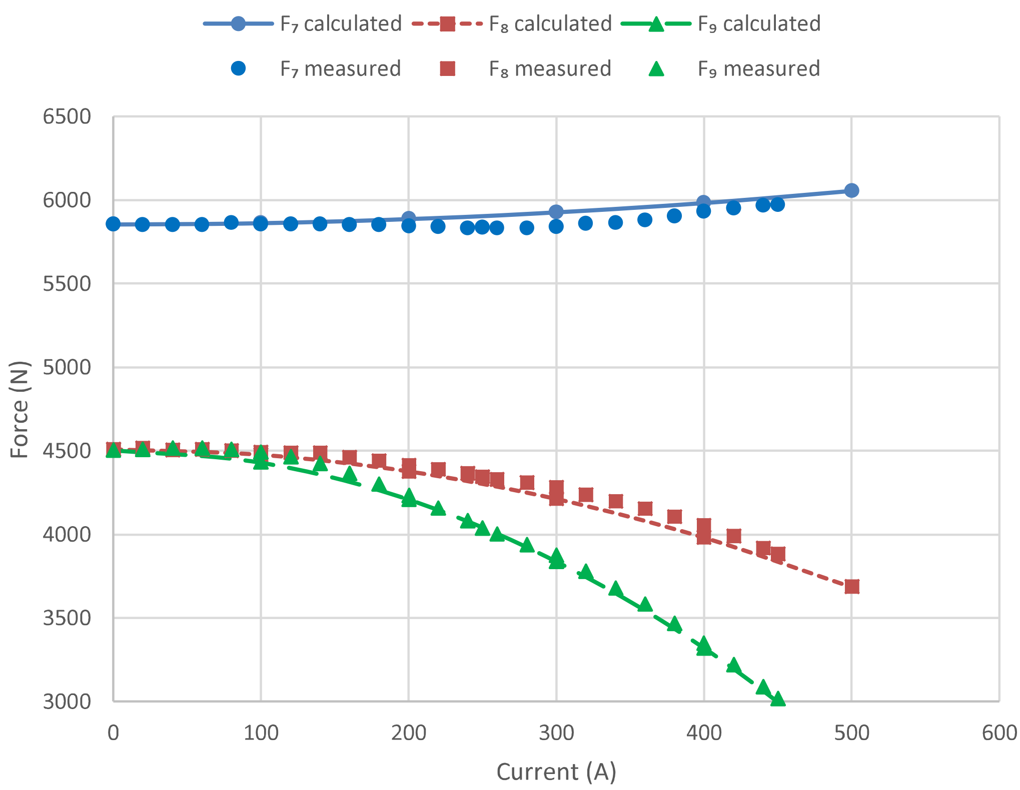

Figure 3.20 Horizontal link force for coil shift of 0.8 mm at 210° angle

It has been tried to correlate the movement given using support nut with the calculated support forces. The coil movement given by adjusting the support nuts during several iterations were vectorially added and found out to be 0.8 mm at 33° angle. If we assume a 1.2 mm initial coil shift towards 210° angle, then after the adjustments, the remaining offset is 0.4 mm at 203°. The calculated offset, 0.8 mm at 210°, does not match with the shift result. The reason for this may be that the same movement of the coil may not have wholly reflected in the actual movement given in the nut due to additional internal stiffness came from the attached plumbing lines with the bobbin [63]. The other reason may be that the magnetic forces are underpredicted by the equation 3.18.

3.8 Conclusion

An analytical model for studying the support system force and coil movement during cool-down and energization of the superconducting magnet was developed. The calculated support link forces during cool-down are compared with both the FEM results and measured values for K500 superconducting cyclotron magnet. It is found that the predicted forces are in excellent agreement with the FEM results. The estimation of the shift of the coil center due to cool-down was also found out from this analysis. It is a significant parameter for energization of the superconducting magnet. If the coil centering is not done correctly, then it may cause a sudden rise of the magnetic force on the horizontal support links during energization.

An analytical model for calculating support forces during energization has also been developed, and the support forces were calculated for K500 superconducting cyclotron for different current in the coil. The prediction from the present model agrees very well with the experimental data taken during energization and is useful for coil centering.

Chapter 4

Proton irradiation studies on support link materials

Chapter 4

4. Proton irradiation studies on support link materials

The cryogenic supports are used for superconducting magnets and RF cavities that are essential parts of large accelerators. These supports are designed with different configurations and varied materials [14], [25], [35], [64] for various kinds of superconducting magnets, like dipoles, solenoids, multipoles, superconducting cavities, etc. The structural materials for supports should have low thermal conductivity and high tensile strength [7]. Epoxy fiberglass composites, carbon fiber reinforced plastic [7], Ti and its alloys [12], [13], etc. are among the structural materials for supports in cryogenic systems. Tie rods made of Ti-5Al-2.5Sn extra-low-interstitial grade titanium alloy were selected to support the cold-mass of the Barrel Toroid of a Toroidal Large Hadron Collider Apparatus (ATLAS) detector and the solenoid of a Compact Muon Solenoid detector [12], [13].

Superconducting magnets used in accelerator and detector applications are subjected to exposure to nuclear radiation. Radioactivity in accelerator components may be induced directly by primary radiations and photonuclear reactions and indirectly by secondary particles (neutrons, protons) originated in the same reactions [65]. The radioactivity induced by primary radiation/photons is confined within a limited region of space. On the other hand, the radioactivity induced by secondary radiation is distributed in space according to their own penetrating power [65]. The lifetime of an accelerator may be considered to be about 25–30 years. During the operation, sometimes there may be a considerable beam loss which will result in the generation of high energy neutrons due to nuclear reactions. These neutrons may cause irradiation damage of the surrounding structural materials. The radiation damage essentially refers to the lattice disorder caused due to elastic collisions of bombarding particles and solid material atoms which result in significant changes in the microstructure of the materials. The cumulative damage with radiation exposure during its operation lifetime causes gradual but permanent changes in the microstructure. This exposure, in turn, affects the physical and mechanical properties of the materials, which limit the performance of the structural components such as cryostat, support structures, etc. in a radiation environment [66].

The irradiation damage study is done to do rapid testing of materials under irradiation for emulating the long-term irradiation effects. Irradiation damage is a process in which primary knock-on atoms (PKAs) induced by energetic particles' bombardment with the target material come to rest in the crystal lattice as an interstitial, which involves the creation of point defects. Due to the diffusion of these isolated point defects, these are agglomerated and forms defect clusters. A significant part of the defects annihilates due to the recombination among them and also in the possible sinks. The equations give the final survival rate of defects (vacancies and interstitials):

$$\frac{dc_v}{dt} = K_0 - K_{iv}C_iC_v - K_{vs}C_vC_s + \nabla.(D_v\nabla C_v) \qquad \dots 4.1$$

$$\frac{dC_i}{dt} = K_0 - K_{iv}C_iC_v - K_{is}C_iC_s + \nabla.(D_i\nabla C_i) \qquad \dots 4.2$$

where $\nabla \cong 0$ with very high sink density.

K_0 - defect production rate

K_{iv} - vacancy-interstitial recombination rate coefficient

K_{vs} is the vacancy-sink recombination rate coefficient

K_{is} is the interstitial-sink recombination rate coefficient,

C_v and C_i are the concentration of vacancies and interstitials

D_v and D_i are the diffusion coefficient for a vacancy and an interstitial.

The solution of the above equation gives $\tau_1 = (K_0\text{-}K_{iv})^{-1/2}$ and $\tau_2 = (K_{is}C_s)^{-1}$, where τ_1 is the characteristic time up to which the linear build-up of defect concentration occurs and τ_2 is the time to achieve quasi-steady state.

These equations are valid for both neutron and proton irradiation, as both the processes are involved with the defect production. With ion irradiation, the rate of production of defects is almost higher by two orders of magnitude. In a post-irradiation test programme (for both neutron and proton), it is only the final state of the material that is important in the determination of equivalence between the microstructure and not the path is taken.

Ti-6Al-4V alloys show very high tensile strength and sufficient elongation at low temperature (15% at 77 K) [67] and is a candidate material for cryogenic support in accelerators [12], [13]. The thermal conductivity of Ti-6Al-4V is always lower than stainless steel in the temperature range of 300 K to 20 K [54]. The radiation environment of the accelerators may make these support materials susceptible to radiation damage. Therefore, it is interesting to study the effect of radiation damage on the microstructure and mechanical properties of Ti-6Al-4V. However, their use requires careful attention to their crack tolerance at cryogenic temperature [68], [69].

Ti–6Al–4V alloy has also been used extensively for other various applications in aerospace and other industries due to its excellent general properties like low elasticity modulus, high resistance to impact loading, high strength to weight ratio, low density, and low thermal expansion coefficient. The database in unirradiated condition on physical and mechanical properties of this alloy is mostly available [70] and [71]. Ti alloys are sensitive to neutron irradiation, and even a relatively low dose of irradiation may cause in degradation of ductility and fracture toughness [72], [73], [74]. Extensive literature is available on the irradiation studies of α-titanium alloys. The irradiation effects on ($\alpha + \beta$) Ti–6Al–4V alloy are limited particularly at low dpa [75], [76], [77], [78], [79], [80]. Here, we have carried out the irradiation of pure Ti (α Ti) and Ti-6Al-4V ($\alpha + \beta$ alloy) using proton beam from the Variable Energy Cyclotron, Kolkata, India to understand and compare the evolution of defects in both the materials at different doses. The changes in microstructure and microhardness as a function of doses have been characterized by X-ray diffraction line profile analysis (XRDLPA) and micro-indentation techniques respectively. X-ray line profile analysis is an effective and a non-destructive technique to characterize the microstructure of the deformed and irradiated alloys ([81], [82] [83], [84], [85], [86], [87], [88], [89], [90], [91]). In the present paper, different model-based approaches like Simplified breadth method [92], [93], [94], Williamson-Hall technique [95], Modified Rietveld method [96], [97], [98] and Variance method [83], [84], [85] have been used to characterize post-irradiated microstructural parameters like domain size, microstrain, dislocation densities as a function of irradiation dose in pure Ti and Ti-6Al-4V.

Microhardness of the unirradiated and irradiated samples has been measured by Vickers hardness tester.
In this study, we have investigated the effect of various levels of proton irradiation on solid samples cut from sheets of annealed materials, namely Titanium and Ti-6Al-4V. Post-irradiation, we obtained the X-ray diffraction data (I vs. 2θ data) for both unirradiated and irradiated samples. The microstructure has been characterized by X-ray Diffraction Line Profile Analysis (XRDLPA).

4.1. Experimental

The materials for this study are pure Ti and Ti–6Al–4V sheet with a thickness of 1.5 mm. The alloy has a nominal composition of Ti–5.8%Al–4%V–0.08%Fe–0.03Si%–0.02%C–0.16O% (in wt.%) and is processed by a conventional rolling route. Samples of size 20 x 20 mm^2 were cut from the sheets of stress relieved pure Ti and annealed Ti-6Al-4V alloy. These samples were mounted on an aluminum flange [Figure 4.1], as used in other irradiation experiments at VECC, and covered with an aluminum foil of thickness 100 μm, which was used as a beam degrader.

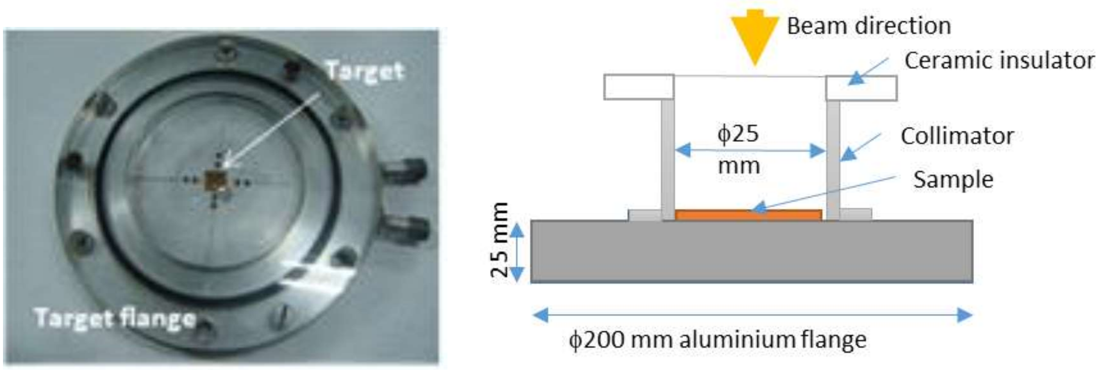

Figure 4.1 Flange for mounting irradiation target

Proton Irradiation was carried out using beam from Variable Energy Cyclotron (VEC), Kolkata [Figure 4.2]. The incident energy of the proton on these samples was 7 MeV after degradation. The irradiation doses were 1 x 10^{20} p/m^2, 7 x 10^{20} p/m^2, 4 x 10^{21} p/m^2 and 5 x 10^{21} p/m^2 (we refer proton/ m^2 as p/m^2 throughout the paper). The dose level in dpa was calculated using SRIM-2000 [99]. A continuous flow of water cooled the flange. As a result, the temperature of the sample did not rise above 313 K as measured by the thermocouple mounted near the sample. The setup mounted on the beamline is shown in Figure 4.3.

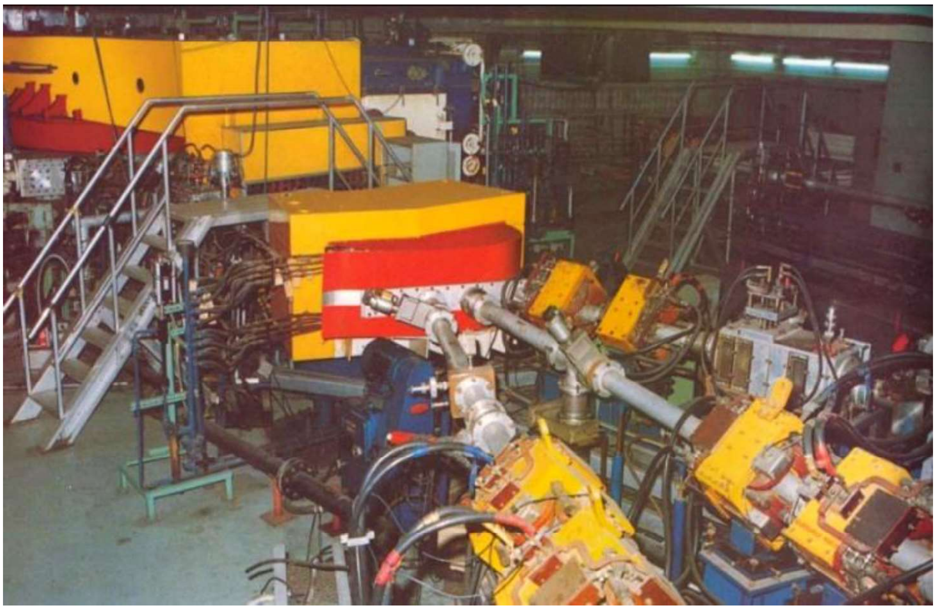

Figure 4.2 Variable Energy Cyclotron

Figure 4.3 Irradiation setup mounted on the beamline

X-ray Diffraction (XRD) profile for each irradiated sample has been collected by Bruker D8 Advance X-ray diffractometer [Figure 4.4] with LYNXEYE detector [100] using CuK$_{\alpha}$ radiation. The range of 2θ was from 35° to 90° and a step scan of 0.02° was used. The time per step was 1 s.

Figure 4.4 Bruker D8 Advance X-ray diffractometer

Microindentation method was used to measure the microhardness values of the unirradiated and irradiated samples. Vickers hardness (HV) values were measured on the irradiated surface using DuraScan-70 [101] hardness tester [Figure 4.5 (a)]. A load of 500 gf was applied on the sample for 20 s to determine the hardness. Seven indentations were carried on the irradiated region of a sample. A gap of about 1 mm was maintained between two successive measurements. Average microhardness value for a sample was determined by averaging hardness values measured at seven distinct locations. The value of the diagonal 'd' used for calculation of HV is obtained from the measure of the impression ${(d_1 + d_2)}/{2}$ diagonals of the impression of the indenter [Figure 4.5 (b)] on the sample is related to the Vickers pyramid number (HV). For the Vickers test, both the diagonals are measured, and the average value is used to compute the HV using the formula:

$$HV \approx 1.8544 \frac{F}{d^2}$$

where F is in kgf and d is in mm.

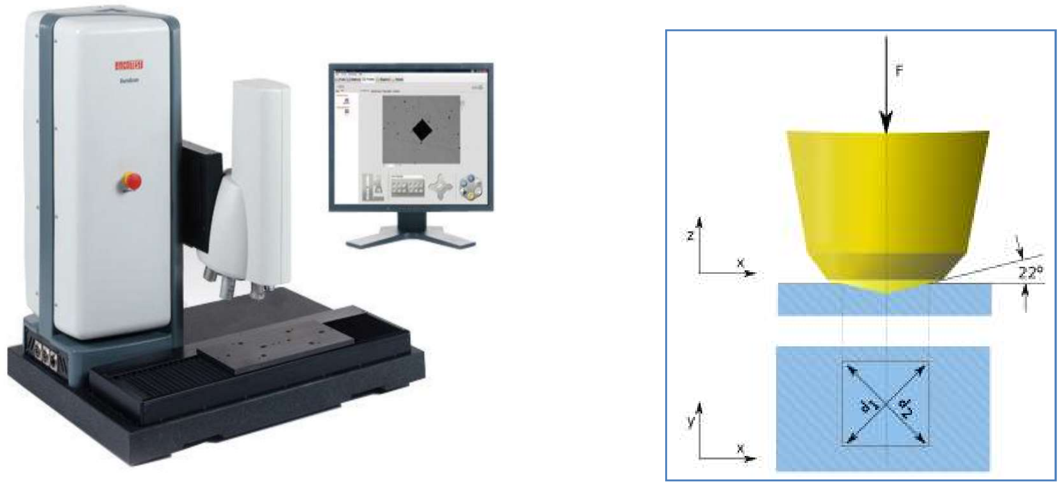

(a) (b)

Figure 4.5 (a) DuraScan-70 hardness tester, (b) diagonals of the impression of the indentation

Unirradiated and irradiated (5 x 10^{21} protons/m^2) Ti-6Al-4V samples were electro-polished using an electrolyte of 90:10 (by volume) methyl alcohol and perchloric acid under 21 V at 40 °C for 10 s. The samples were subjected to the electron backscatter diffraction (EBSD) analysis (orientation image mapping system provided by Oxford Instruments) within an FE-SEM (field emission scanning electron microscope) instrument from Carl Zeiss using 25 kV accelerating voltage. In each sample, an approximate area of 500 μm x 500 μm was scanned by the EBSD. Beam and video conditions were kept identical between the scans, and a step size of 0.5 μm was used. In EBSD analysis, grains were identified based on a 10° misorientation criterion.

4.2. Method of Analysis

The analysis aims to find out the variation of microstructure with irradiation. The broadening of a Bragg peak usually occurs due to instrument and specimen. Origins of specimen broadening are numerous. Generally, any lattice imperfection will cause additional diffraction-line broadening. Therefore, dislocations, vacancies, interstitials, substitutional, and similar defects lead to lattice strain. If a crystal is broken into smaller incoherently diffracting domains by dislocation arrays (small-angle boundaries), stacking faults, twins, large-angle boundaries (grains), or any other extended imperfections, then domain-size broadening occurs. So, we can say, overall, the broadening of a Bragg peak occurs due to the instrumental broadening, small domain size and microstrain. Detailed broadening information is obtainable from the line shapes of the peaks; analysis of the line shapes permits characterization of the microstructure in terms of the microstrain and average domain size. Simplified Breadth Method and Williamson-Hall technique have been incorporated in the present study for the analysis. The instrumental broadening correction was made using a standard defect-free Si sample.

4.3 Data Analysis and Results

The range of 7 MeV proton in Titanium was found to be around 230 μm using SRIM 2000 software [99]. The total target displacements of the collision events as a function of depth as evaluated using SRIM 2000 are shown in Figure 4.6. The average dpa value over a range of 230 μm for the highest dose sample was found to be around 0.03 dpa, and at the peak damage region, the dpa is 1.

A typical well-recrystallized microstructure of unirradiated and irradiated Ti-6Al-4V at the highest dose (5 x 10^{21} p/m^2) has been shown in Figure 4.7 (a) and (b). The average grain size for the samples was found to vary 10–30 μm in both the cases. The figure shows the EBSD Inverse Pole Figure (IPF) map of the unirradiated and irradiated samples respectively. High angle boundaries are marked in black in the maps.

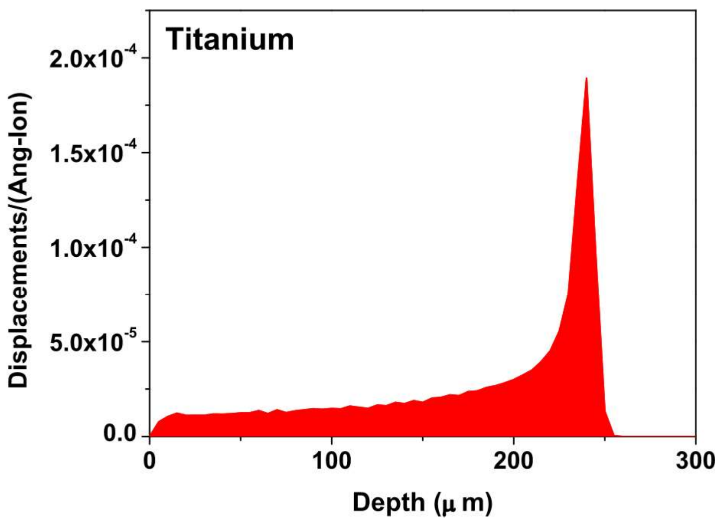

Figure 4.6 Damage profile of 7 MeV proton in Titanium (Calculated using SRIM 2000)

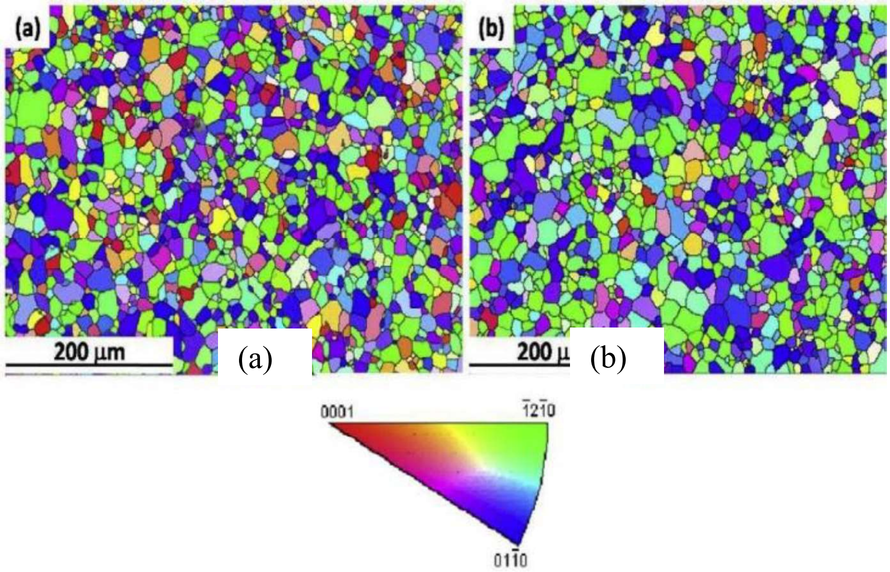

Figure 4.7 EBSD Inverse Pole Fig. map of (a) unirradiated and (b) irradiated Ti-6Al-4V (dose 5 x 10^{21} p/m^2) samples.

Detailed X-ray diffraction line profile analysis has been carried out on the unirradiated and irradiated samples of pure Ti and Ti-6Al-4V samples as a function of radiation dose. Apart from the instrumental broadening, X-ray diffraction peak profiles may broaden because of 1) small crystallite size, 2) dislocations, 3) planer defects (Stacking faults and twin boundaries), 4) chemical heterogeneities, and 5) surface relaxation in case of nanoparticles [102]. Due to the long-range characteristics of the strain field arising out of dislocations, these defects cause considerable line broadening in the diffraction peaks [103] [104]. If structural mistakes are present, the arrangements of atoms differ in different regions of the crystallite [92]. This difference can arise from the external influence, such as heat treatment, plastic deformation, and adsorption or radiation damage [92]. The choice of the methods or techniques is of utmost importance to obtain the parameters of pure physically broadened line profile for further line broadening analysis. Basically, the methods ([81], [82], [83], [84], [85], [86], [87], [88], [89], [90], [91], [92], [93], [94], [95], [96], [97], [98], [102], [103], [104], [105], [106] & [107]) can be divided into two broadly classified groups, (1) the deconvolution approach, where the physically broadened peak is unfolded from the observed profile and the (2) the convolution approach, where, in contrast a profile is generated with suitable mathematical function and adjusted to the observed pattern through a least square fitting. We have used different techniques such as single peak analysis by integral breadth method ([92], [93], [94]), Williamson-Hall technique [95], [108], modified Rietveld method by whole powder pattern fitting technique using MAUD software [109] and Variance method to characterize the microstructural parameters of the irradiated Ti and Ti-6Al-4V samples. In all these techniques except variance method, predefined mathematical functions such as Voigt, Lorentzian or pseudo-Voigt function are used to fit the diffraction profiles. Fourier transform of the individual profiles is then carried out after correcting the instrumental broadening. The fitting values of the Fourier transform as a function of coherent length are correlated with the microstructural parameters. In the variance method, the asymptotic behavior of the second and fourth order restricted moments of the intensity distribution in the diffraction peaks are analyzed for the determination of the mean size of the crystallites [98]. Groma [107] and Borbely and Groma [105] presented an improved method over it for the evaluation of particle size and dislocation density from X-ray Bragg peaks. The method of analysis for these techniques has been described in detail in papers ([87] to [91]).

Figure 4.8 shows the 2θ vs. intensity for pure Ti (un-irradiated and irradiated at different doses). The intensity of the peaks of the irradiated samples changes significantly with dose as compared to the unirradiated samples as seen from the figure. It is also clearly evident that the shape of the peak profiles almost remained unaltered particularly for the highest intensity peak, i.e. (0 0 2) with increasing doses of irradiation. Another interesting thing to note that the (1 0 1) peak was almost symmetric in un-irradiated condition but it became asymmetric after a dose of 7 x 10^{20} p/m^2 (inset Figure 4.8), particularly at the right side of the peak. The asymmetry was found to increase with dose.

On the other hand, the variation of intensity of the XRD peaks of Ti-6Al-4V is not as significant for the irradiated samples as compared to unirradiated sample as seen in Figure 4.9. Moreover, these peaks are found to be much more symmetric at different doses except for the highest dose, i.e., at 5 x 10^{21} p/m^2 as seen in Figure 4.9. At this dose, the broadening of the peaks has reduced and a clear separation of α_1 and α_2

peaks for each diffraction peak is revealed with a high asymmetry at the left part of the tail (Figure 4.9 inset). The asymmetry was so significant that we could not carry out an analysis with the techniques stated earlier.

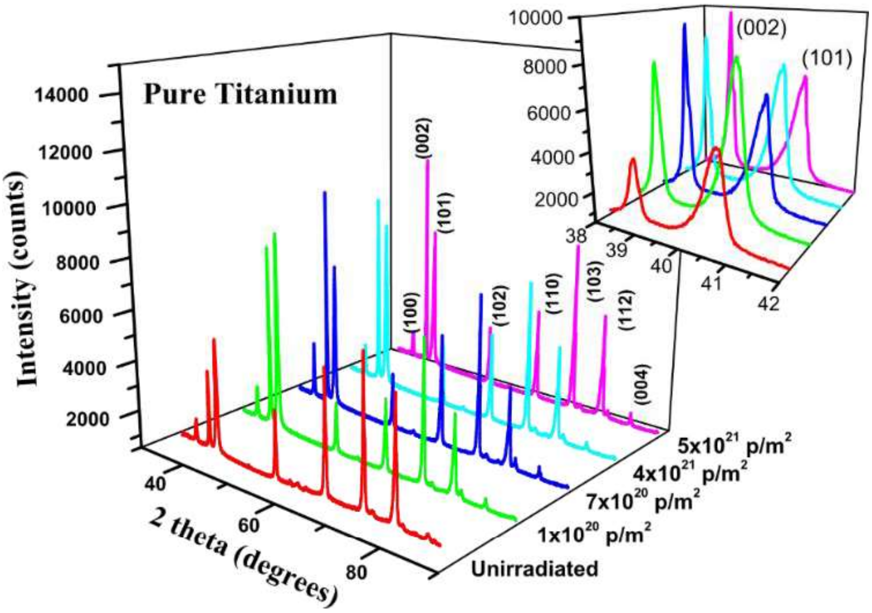

Figure 4.8 XRD profiles obtained from unirradiated and irradiated pure Ti samples. The inset shows the graph in expanded scale near (0 0 2) and (1 0 1) peaks.

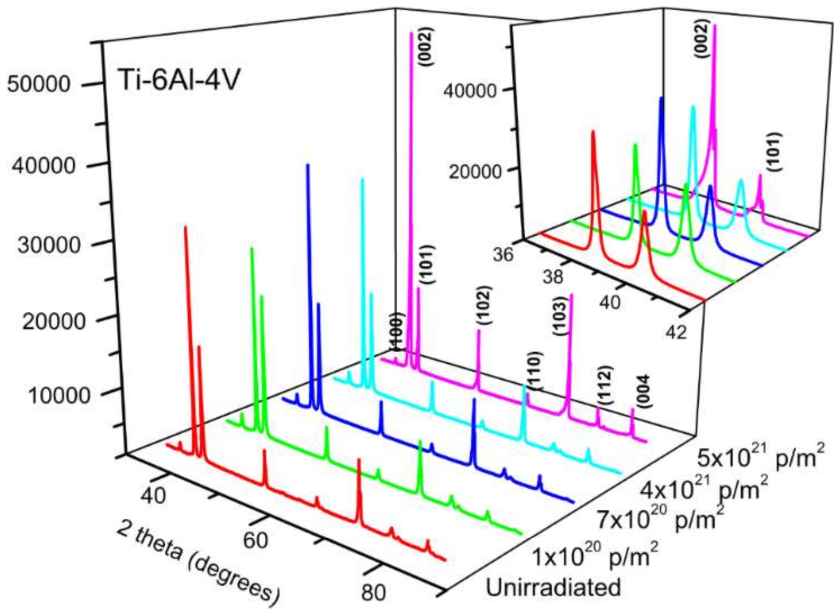

Figure 4.9 XRD profiles obtained from unirradiated and irradiated Ti-6Al-4V samples. The inset shows the graph in expanded scale near (0 0 2) and (1 0 1) peaks

4.3.1 Size-Strain Analysis from Simplified Breadth Method

According to Van de Hulst and Reesinck [93], X-ray line profiles can be approximated by a Voigt function, a convolution of a Cauchy and a Gaussian function. Langford [94] derived an explicit equation for a Voigt function and showed that the breadth of Cauchy and Gaussian part could be obtained from the value of $2\omega/\beta$ ($=\phi$, called the shape factor where ω is the Full Width at Half Maxima), where β is the instrumental corrected integral breadth of a XRD peak. For a Voigt function ϕ varies between the limits:

$0{:}63 \leq \phi \leq 0{:}94$

where $\phi = 0.63$ is the Cauchy limit and $\phi = 0.94$ is the Gaussian limit. In the absence of higher orders of a particular family of reflection, the size-strain analysis requires the assumption of profile shapes for size and strain broadened profiles. The Cauchy component of the profile is assumed to be solely due to small crystallite size and the Gaussian component is due to the microstrain. The relation between volume weighted domain size (D_v), microstrain (ϵ), β_c and β_G is given by:

$$D_v = \frac{\lambda}{\beta_c \cos(\theta)} \text{ and } \epsilon = \frac{\beta_G}{\tan(\theta)}$$

Where, β_c and β_G represent the Cauchy and Gauss component of the integral breadth respectively. 2θ is the diffraction angle. λ is the wavelength of CuK_α.

Table 3: Values of D_v and ε from single peak analysis using simplified breadth method

Plane	**Unirradiated**		**1 x 10^{20} p/m^2**		**7 x 10^{20} p/m^2**		**4 x 10^{21} p/m^2**		**5 x 10^{21} p/m^2**	
hkl	**D_v (Å) ±10%**	**ε (10^{-3}) ±5%**	**D_v (Å) ±10%**	**ε (10^{-3}) ±5%**	**D_v (Å) ±10%**	**ε (10^{-3}) ±5%**	**D_v (Å) ±10%**	**ε (10^{-3}) ±5%**	**D_v (Å) ±10%**	**ε (10^{-3}) ±5%**
100	322	2	247	2	351	2	348	3.09	308	2.51
002	426	1	383	1	572	1	446	0.63	576	0.92
101	205	2	217	3	256	4	239	3.3	243	2.88
102	358	2	251	2	325	2	293	1.44	352	1.61
110	368	2	300	2	323	2	314	1.96	348	2.09
103	398	2	422	2	417	1	433	1.53	492	1.56
112	284	2	199	1	223	1	205	0.93	257	1.51

Single peak analysis has been carried out using the simplified breadth method for all the reflections for both Ti and Ti-6Al-4V samples at different doses. The XRD pattern only shows the peaks of the α phase, no peak related to the β-phase could be observed. We could not carry out the analysis on the samples irradiated at 5 x 10^{21} p/m^2 for Ti-6Al-4V sample, as the peaks were highly asymmetric. Table 3 and Table 4 gives the values of D_v (volume weighted domain size) and ε (upper microstrain) for pure Ti and Ti-6Al-4V samples respectively.

Table 4: Values of D_v and ε from single peak analysis using simplified breadth method for Ti-6Al-4V samples

Plane	**Unirradiated**		**1 x 10^{20} p/m^2**		**7 x 10^{20} p/m^2**		**4 x 10^{21} p/m^2**	
hkl	**D_v (Å) ±10%**	**ε (10^{-3}) ±5%**	**D_v (Å) ±10%**	**ε (10^{-3}) ±5%**	**D_v (Å) ±10%**	**ε (10^{-3}) ±5%**	**D_v (Å) ±10%**	**ε (10^{-3}) ±5%**
(100)	320	1.03	311	1.0	318	1.09	276	1.25
(002)	631	1.05	512	0.85	633	1.12	564	1.51
(101)	360	1.66	335	1.78	351	1.69	318	1.98
(102)	438	0.97	332	0.68	409	0.75	368	0.87
(110)	296	0.35	296	1.04	283	0.95	277	0.97
(103)	458	0.96	355	0.97	425	0.85	386	0.94
(112)	237	0.45	–	–	–	–	–	–
(004)	–	–	312	0.56	420	0.62	363	0.50

The variation of domain size for pure Ti and Ti-6Al-4V as revealed from the analysis does not show any systematic dependence on the doses. Rather, the values of the domains are within the error limit even with the increase in dose of irradiation except for a very few crystallographic planes for both the materials. Microstrain values also remain almost invariant in both the cases even at higher doses of irradiation.

4.3.2 Williamson-Hall Plots

In a Williamson–Hall (W–H) [95] plot the integral breadth β of the specimen is plotted with $S = \left(\frac{2\sin\theta}{\lambda}\right)$. The size term $\left({}^{1}/_{D_v}\right)$ represents the order-independent and 2ε the order-dependent part. If a W–H plot is strongly order-dependent with negligible intercept, X-ray line broadening is attributed to strain broadening only. If, however, the plot is order-dependent with measurable intercept then size broadening may be appreciable. Thus, an indexed Williamson-Hall plot is essential to ascertain the origin of line broadening and forms the basis of a more detailed analysis. In this model, it was assumed that both size and the strain broadened profiles are Cauchy in nature. Based on this assumption, a mathematical relation was established between integral breadth (β), volume weighted average domain size (D_v) and microstrain (ε) as follows:

$$\frac{\beta cos\theta}{\lambda} = \frac{1}{D_v} + 2\epsilon\frac{2sin\theta}{\lambda} \qquad ...4.3$$

The plot $\frac{\beta \cos\theta}{\lambda}$ $vs.$ $S = \left(\frac{2\sin\theta}{\lambda}\right)$ gives the values of ϵ from the slope and D_v from the ordinate intersection.

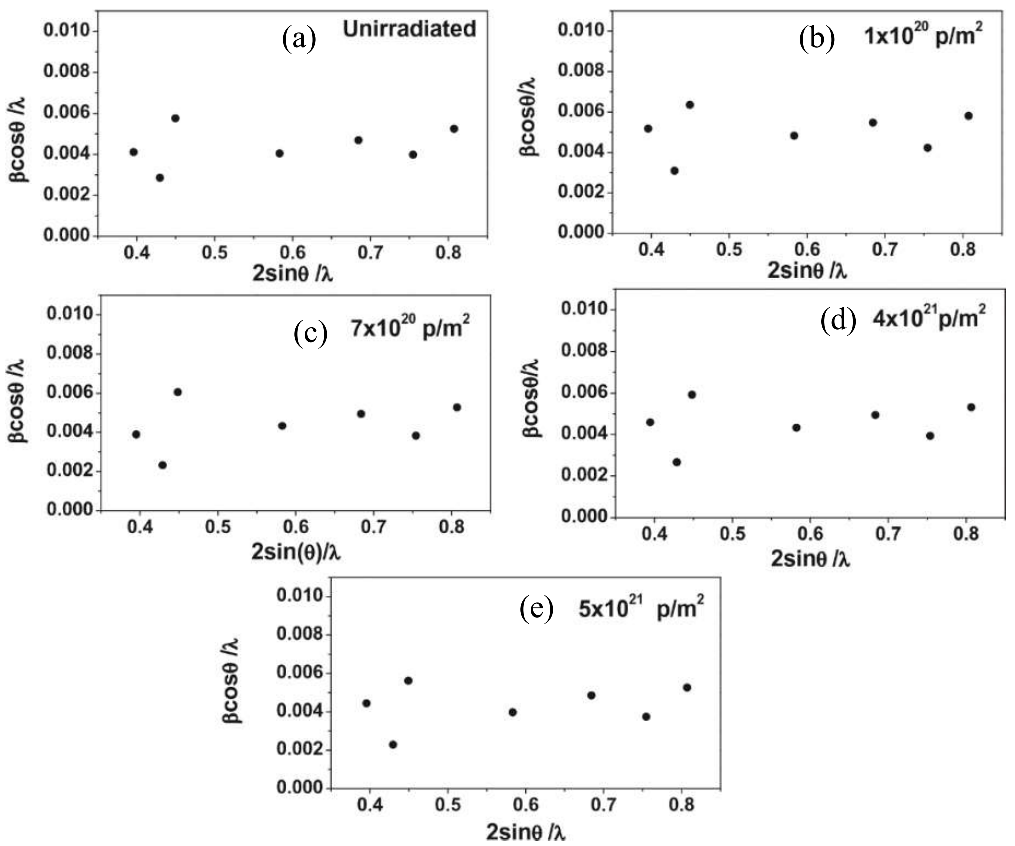

Figure 4.10 Williamson-Hall plot for the (a) unirradiated and (b–e) irradiated pure Titanium samples

Figure 4.10 and Figure 4.11 show the WH plots for unirradiated and irradiated pure Ti and Ti-alloy samples. In general, W-H plots are used as a first approximation to find the relative importance of the domain size and microstrain on XRD line broadening effects [95]. It is based on the Uniform deformation model (UDM), where the strain is assumed to be uniform in all crystallographic directions. Hence the isotropic nature of the crystal is considered, where the material properties are independent of the direction along which they are measured [108]. Ti-based alloys being HCP materials, it has an inherent anisotropy along different crystallographic directions. As a result, the plots are highly scattered and therefore a linear dependence of $\beta cos\theta/\lambda$ with S (where β is the instrumental corrected integral breadth, λ is the wavelength of CuK_{α}) could not be established, implying the anisotropic nature of the domains and microstrain.

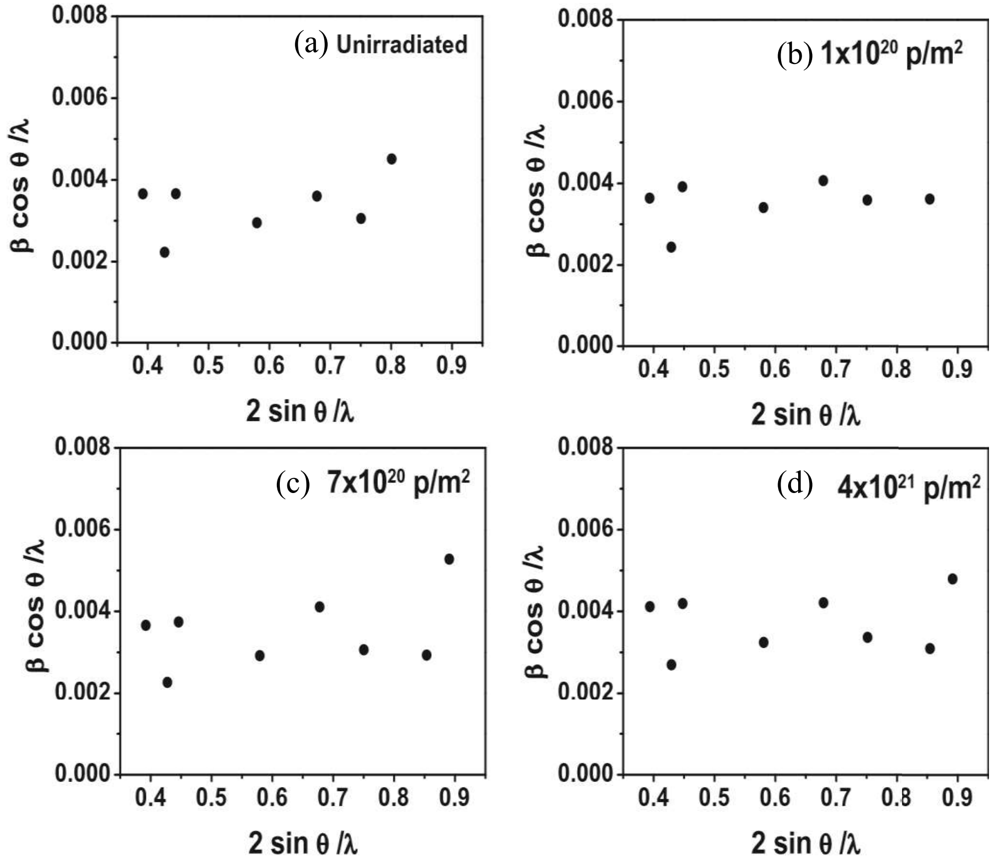

Figure 4.11 Williamson-Hall plot for the (a) unirradiated and (b–d) irradiated Ti-6Al-4V samples

4.3.3 Modified Rietveld technique

The X-ray diffraction spectra were analyzed with the Modified Rietveld method using the program package MAUD [109]. Using the similar procedure described by Wenk et al. [110], XRD data were refined considering the instrument parameters, obtained using the standard LaB6. The background, the lattice parameters and the microstructural parameters (relative isotropic crystallite size (D_S) and r.m.s. microstrain $\langle\epsilon_L^2\rangle^{\frac{1}{2}}$ were then refined, and finally, the preferred orientation parameter (P) were also considered to obtain the best fit. Figure 4.12 (a) and (b) represents a typical Rietveld fit for the samples at a dose of 4 x 10^{21} p/m^2 for pure Ti and Ti-6Al-4V samples.

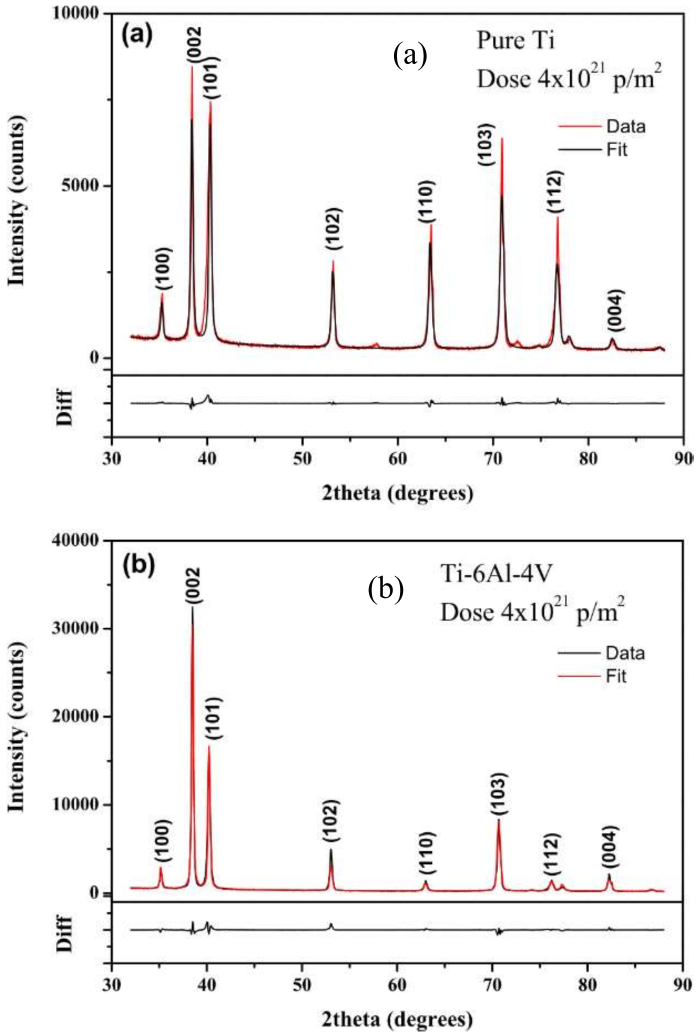

Figure 4.12 Modified Rietveld fitting plot of the (a) pure Ti irradiated to 4 x10^{21} p/m^2 and (b) Ti-6Al-4V alloy irradiated to 4x10^{21} p/m^2

Figure 4.13 (a) and (b) represent the variation of domain size as a function of dose. In both the cases, the trend of the variation of domain size with dose remains almost the same. In case of pure Ti, the domain size is smaller as compared to Ti-6Al-4V even for the unirradiated sample. The domain size has reduced at the initial dose of irradiation and then increased with dose and finally saturates at higher doses.

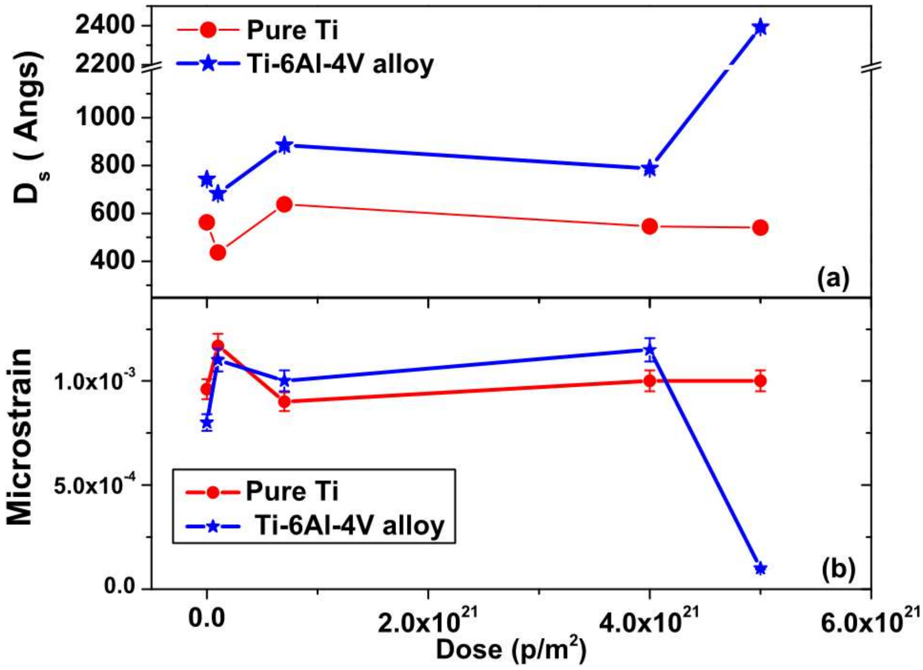

Figure 4.13 Variation of (a) average surface weighted domain size and (b) microstrain as a function of irradiation dose for pure Ti and Ti-6Al-4V

In the transient region at low doses of irradiation, the lattice disruption caused by the bombardment of the projectile results in generation of vacancies, which act as incoherent region in the X-ray diffraction. This is termed as domain. The size of the domain decreased initially with dose. During irradiation, two competing processes take place simultaneously; first the generation of irradiation-induced vacancies which migrate and agglomerate leading to formation of vacancy clusters [111]. These vacancy clusters then form dislocation loops. On the other hand, the second mechanism which plays a key role in governing the microstructural evolution during irradiation is the annihilation of defects in the possible sinks (dislocation loops) [111]. As the damage occurs in a localized region (within 230 μm), concentration of small order defect clusters is quite high within that region. These act as trapping center for irradiation-induced defects during the course of irradiation. This results in an increase of the size of the coherent region due to the annihilation of defects, restoring perfect lattice. This phenomenon is observed at an intermediate dose of 7 x 10^{20} p/m^2 for both pure Ti and Ti-6Al-4V alloy, where the domain size has increased with dose. With further increase in dose (4 x 10^{21} p/m^2,), the domain size is found to saturate for both the materials as observed in Figure 4.13 (a).

This clearly indicates that dynamical steady state has been achieved between the two competing processes as discussed earlier, at higher doses of irradiation. Moreover, the domain size for Ti-6Al-4V is found to be higher as compared to pure Ti at all doses. This may be attributed to the formation of vacancy-impurity (alloying elements) complexes which inhibit the vacancies to grow as clusters; hence restricting the formation of incoherent region or domain within the matrix.

It is interesting to note that the broadening of the XRD peaks of the sample at highest dose (5 x 10^{21} p/m^2) of irradiation is almost negligible for Ti-6Al-4V and α_1 and α_2 peaks are clearly resolved for each diffraction peak (Figure 4.9 inset). This clearly signifies that there is a relaxation of strain field of the matrix of α-phase. On the other hand, all the peaks reveal a hump near the tail of the left side. This may be attributed to the radiation-induced segregation (RIS) of the undersized solutes like V and Al [112]. Ti-6Al4V exhibits extensive phase redistribution under irradiation [112]. Wilkes and Kulcinski [113] have shown that ion irradiation of this alloy resulted in the formation of copious precipitation of a fine bcc phase in the matrix of a titanium. Further studies using dual ion beam [79], [114] and neutron irradiation [115], [116] of Ti-Al-4V have confirmed that the beta precipitates (rich in V) are radiation-induced precipitates. In our case, XRD analysis could not reveal any β-phase even in the samples irradiated with the highest dose. This may be due to the smaller volume fraction of the β precipitates which may be beyond the detectable limit by XRD. However, Aida Amroussia et al. [78] could not observe any notable change in the microstructure of Ti-6Al-4V and Ti-6Al-4V-1B even after irradiation with swift heavy ion. In the XRD pattern, a clear asymmetry was observed in the left-hand sides of all the peaks. This may have been resulted due to the segregation of solute elements during irradiation, which has caused a change in the local variation of lattice parameters [117], [118]. Zubicza [102] has given a detail description of the line broadening caused by chemical heterogeneities which yields a distribution of the profile centers scattered from different volume of the materials.

4.3.4 Variance method

Variance method is based on the analysis of an individual peak. Figure 4.14 (a) and (b) represents the XRD data of (1 0 1) peak in q-space for both pure Ti and Ti-6Al-4V. It is seen that peak broadening is less in Ti-6Al-4V as compared to pure Ti. No analysis could be done on pure Ti irradiated at 5 x 10^{21} p/m^2, eventhough the peak was symmetric. This is due to the scattered tail region of the peak (1 0 1) in the q-space as can be seen in Figure 4.14 (a). Moreover, we could not also carry out analysis of the highly asymmetric (1 0 1) peak for the sample Ti-6Al-4V at 5 x 10^{21} p/m^2 with a hump at the left side tail part, which would otherwise give erroneous results.

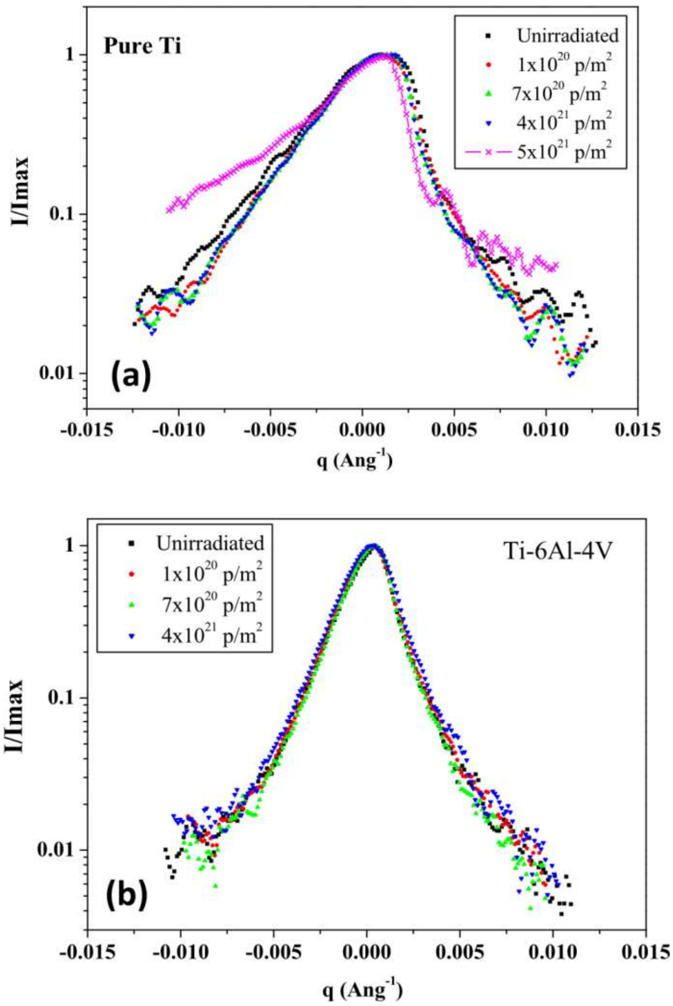

Figure 4.14 (101) peaks obtained from XRD data in q-space for the unirradiated and irradiated (a) pure Ti samples, (b) Ti-6Al-4V samples

Figure 4.15 and Figure 4.16 show the typical second- and fourth-order moments of the peak of pure Ti samples and Ti-6Al-4V alloy irradiated at different doses. The second order and fourth order restricted moments are of the following forms [84], [85], [105]:

$$M_2(q) = \frac{1}{\pi^2 D_s} q - \frac{L}{4\pi^2 K^2 D_s^2} + \frac{\Lambda \langle \rho \rangle \ln\left(q/q_0 \right)}{2\pi^2} \quad .... 4.4$$

and

$$\frac{M_4(q)}{q^2} = \frac{1}{(3\pi^2 D_S)} q + \frac{\Lambda(\rho)}{4\pi^2} + \frac{3\Lambda^2 \langle \rho^2 \rangle}{4\pi^2 q^2} \ln^2(q/q_1) \quad .... 4.5$$

where D_s is the average column length or area weighted domain size measured in the direction of the diffraction vector, L is the taper parameter, K is the Scherrer constant, $\langle \rho \rangle$ is the average dislocation density, $\langle \rho^2 \rangle$ is the average of the square of the dislocation density, q_0 and q_1 are fitting parameters and Λ is a geometrical constant describing the strength of the dislocation contrast which takes the value of the order of unity [84], [85], [105].

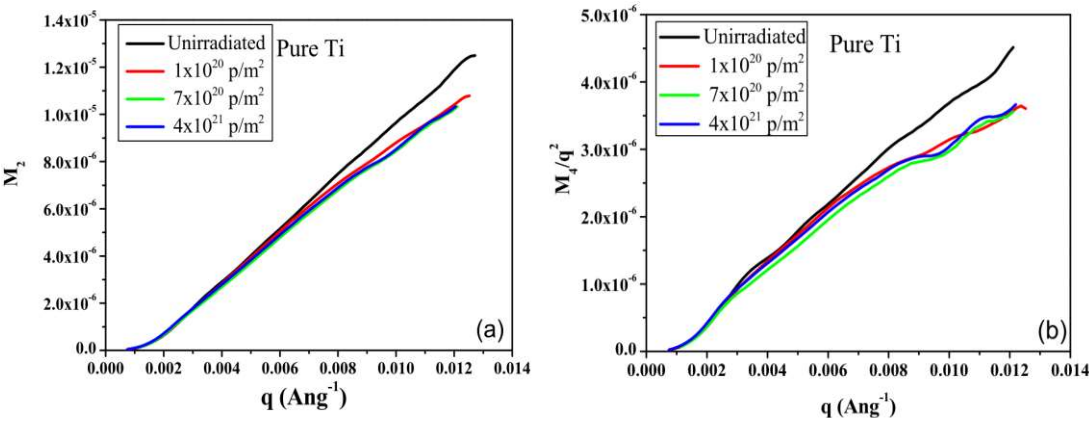

Figure 4.15 Second order and Fourth order restricted moments of the (1 0 1) peak of pure Ti samples

The asymptotic regions of the curves are fitted with Equations 4.4 and 4.5 [105] respectively. The nature of M_2 and M_4 suggest that both size and strain broadening are present [105]. The background values were chosen in both the cases in such a way that the calculated M_2 and M_4 from those data range yielded the similar size and dislocation density values [105]. The domain size and dislocation density obtained from the fit done for the unirradiated and irradiated samples are listed in Table 5 and Table 6 for pure Ti and Ti-6Al-4V. The maximum error in the size values is ±10%, and the maximum error for dislocation density is ±20%.

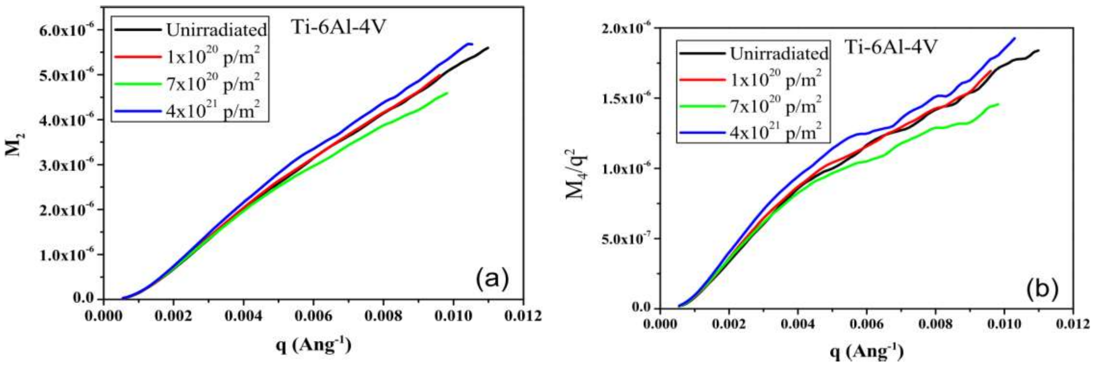

Figure 4.16 Second order and Fourth order restricted moments of the (1 0 1) peak of Ti6Al-4V samples

Table 5: Results of variance analysis of the (1 0 1) peak for pure Ti samples

Sample	**D_s (Å) (±10%)**	**Dislocation density ($/m^2$) (±20%)**
Unirradiated	101	1.5 x 10^{15}
1 x 10^{20} p/m^2	227	7.3 x 10^{15}
7 x 10^{20} p/m^2	126	1.8 x 10^{15}
4 x 10^{21} p/m^2	161	4.6 x 10^{15}
5 x 10^{21} p/m^2	–	–

Table 6: Results of Variance analysis of the (1 0 1) peak for Ti-6Al-4V samples

Sample	**D_s (Å) (±10%)**	**Dislocation density ($/m^2$) (±20%)**
Unirradiated	235	1.04 x 10^{15}
1 x 10^{20} p/m^2	278	1.8 x 10^{15}
7 x 10^{20} p/m^2	369	2.2 x 10^{15}
4 x 10^{21} p/m^2	226	1 x 10^{15}
5 x 10^{21} p/m^2	–	–

It is to be noted that the results obtained by the various techniques show a similar trend in the variation of the microstructural parameters. However, the absolute values of different parameters obtained from each analysis should not be compared.

4.3.5 Microhardness measurement

Figure 4.17 shows the Vickers hardness values of the unirradiated and the irradiated samples for both the materials. The hardness values of the pure Ti are higher than that of Ti6Al-4Vfor both unirradiated and irradiated samples. In the case of pure Ti, the microhardness values have increased systematically and then saturates with dose.

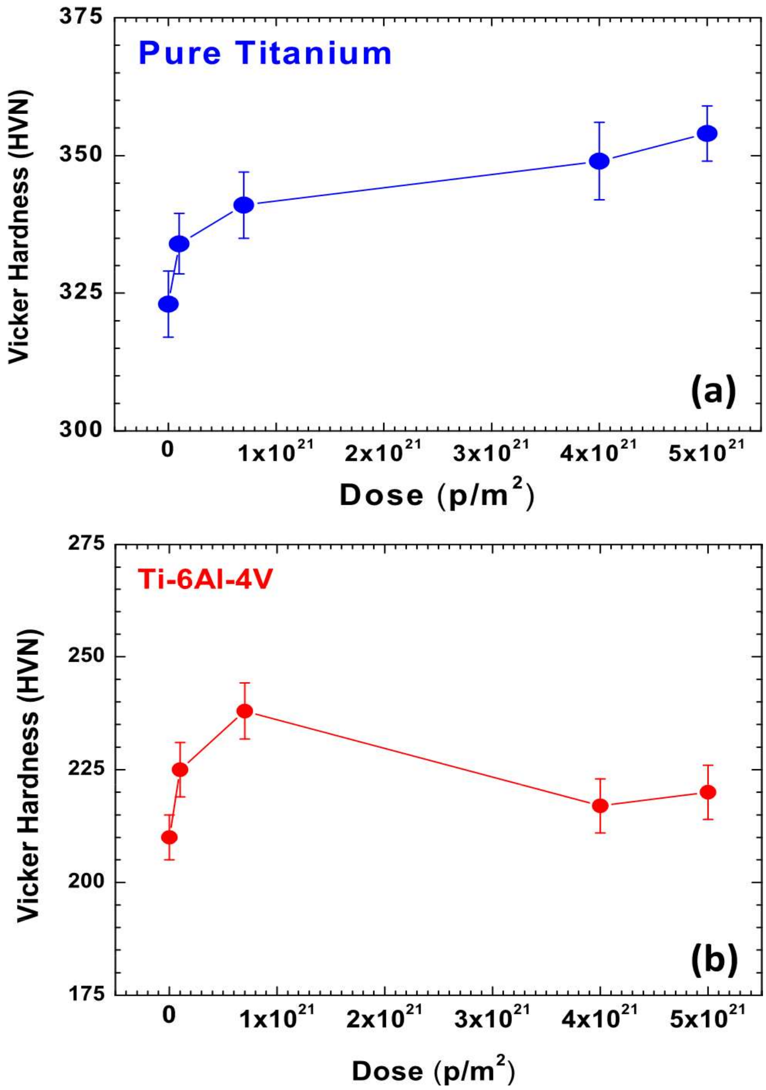

Figure 4.17 Microhardness values (Vickers Hardness) as a function of dose for pure Ti and Ti-6Al-4V samples

The microhardness value obtained for the unirradiated pure Ti sample is found to be higher than that reported in the literature [119]. The results reported in [119] are for fully annealed samples and our as received pure Ti samples were in stress-relieved condition.

On the contrary, a significant reduction in microhardness values for irradiated Ti-6Al-4V samples at the doses 4 x 10^{21} p/m^2 and 5 x 10^{21} p/m^2 have been seen. The reason may be the segregation of alloying elements resulted during irradiation, as also observed in XRD. These results corroborate with the values obtained by XRDLPA where the domain size increases and dislocation density decrease slightly at these doses.

We have irradiated Ti-6Al-4V at different doses and have studied the microstructural changes as a function of dose and then compared with pure Ti sample in the same irradiated condition. Since there exists a strong correlation between microstructure and mechanical properties, a systematic quantitative characterization of the microstructural parameters will help to study the degradation of the mechanical properties of these structural components as a function of dose. Here we see that domain size of Ti-6Al-4V has increased at a dose of 7 x 10^{20} p/m^2 and then almost saturated up to a dose of 4 x 10^{21} p/m^2. At the highest dose of irradiation, it is observed that the effect of irradiation is almost negligible as it is also evident from the separation of $\alpha_1$and α_2 peaks (Figure 4.9 inset). Moreover, we see that the microhardness value of Ti-6Al-4V even at the highest dose of irradiation is comparable with the unirradiated sample which contrasts with the results of pure Ti where the hardness values were found to increase with dose. Hence, this study reflects that the effect of irradiation on Ti-6Al-4V alloy is not significant with respect to the changes in microstructure and mechanical properties.

Amroussia et al. [78] estimated the change in microhardness with dpa in Ti-6Al-4V due to 36 MeV Ar ions at two different temperatures. To compare the results of present study, relative change in microhardness has been calculated for different doses of proton irradiation. Penetration depth of the Vickers indenter at 500 gf on Ti-6Al-4V was 7.2 μm. Irradiation dose in terms of dpa was estimated for the region of microhardness measurement. Figure 4.18 shows the variation of relative microhardness values with dose for proton-irradiated samples along with the results of

Amroussia et al. [78], shown as Tirr = 350°C Ar @ 36 MeV and Tirr = 25°C Ar @ 36 MeV. It is evident that the relative values of microhardness follow similar trend.

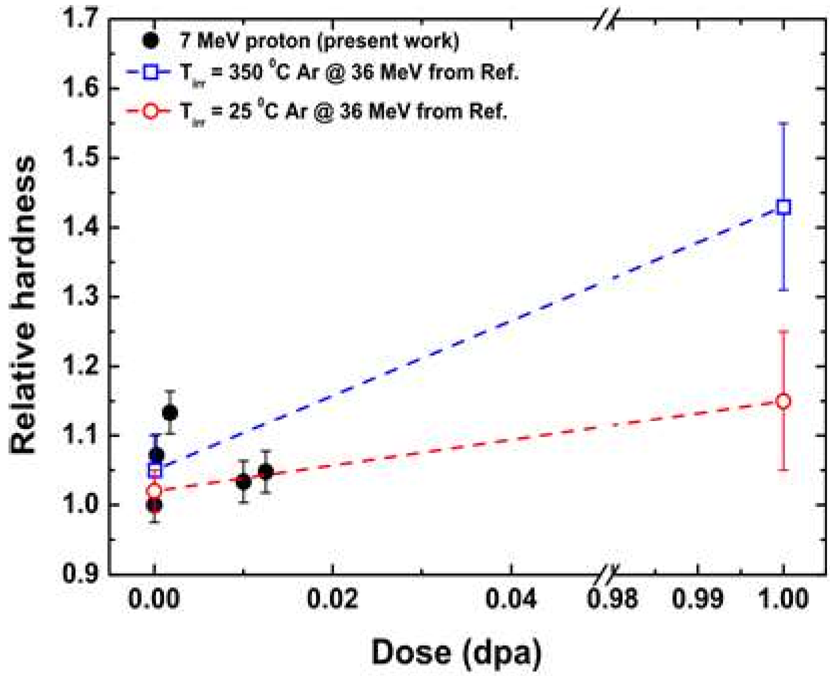

Figure 4.18 Relative microhardness values as a function of dpa in Ti-6Al-4V

4.4 Conclusions

It is reported in the literature that Ti-6Al-4V alloy is considered as a good candidate material for cryogenic support in accelerators [12], [13] as it shows very high tensile strength at low temperature and low thermal conductivity (lower than stainless steel) in the temperature range of 300 K to 20 K [54], [67]. Our study shows that Ti-6Al-4V can also be considered a radiation resistant alloy at least up to a dose of 4 x 10^{21} p/m^2, which is expected to be higher than the normal dose experienced by the supporting structure of accelerators during its lifetime (almost equivalent to the dose of 1 x 10^{16} p/m^2 considering 20 years of operation).

In the present studies, the microstructure of the irradiated samples has been characterized in detail using different model-based techniques of XRDLPA. These methods may not be comparable, but they are complementary to each other. It is seen from the analysis that the broadening of the diffraction peaks and the domain size (both the surface weighted and volume weighted) for irradiated Ti-6Al-4V samples, obtained from different techniques were found to be more as compared to the irradiated pure Ti samples. This clearly indicated that the size of the incoherent regions resulted during irradiation (domain) due to the formation of defects are less for the same dose of irradiation for pure Ti which imply that this material is less resistant to radiation damage compared to Ti-6Al-4V with respect to microstructure up to the dose 4 x 10^{21} p/m^2. At the higher doses, the segregation of alloying elements due to irradiation was evident. The microhardness values are found to increase with dose for pure Ti but show a clear decreasing trend for Ti-6Al-4V alloys.

Chapter 5
Conclusion

Chapter 5

5. Conclusion

5.1 Summary

Finite element method has long been used to design and analyze support structures of the superconducting magnets. Use of finite element software is an elaborate task for analyzing the support systems involving large resources of time and memories. In this work, an analytical model is demonstrated for superconducting magnet support links for finding out support forces and coil movement. This model includes thermal and magnetic loads and temperature dependent properties of materials.

In this study, analytical models for thermal and magnetic analysis have been developed for the coil and support links together as a system for superconducting dipole magnet. Detailed analysis has been carried out for a large aperture superferric dipole magnet, being designed for the Energy Buncher of the FAIR project. The dipole magnet has an aperture of ±380 mm horizontal and ±100 mm vertical. The magnetic field uniformity required is $\pm 3 \times 10^{-4,}$ and associated accuracy requirement for placement of the coil is ±1 mm.

The output generated by the analytical model help us to determine the support link forces/stresses and the coil shift under the combined effect of thermal and magnetic loads. The effect for coil shift with cool-down of the coil is calculated analytically and using Finite Element Methods. The result of the coil shift is compared for both cases and found to agree well.

The results of the analysis were applied to optimize the support stiffness for the FAIR dipole magnet, considering the minimization of both the coil shift and the heat load to the coil. The model captured the uncontrollable coil movement in case of less support stiffness than the magnetic stiffness and provided the minimum limit of the stiffness required. It has been found that the optimized support stiffness is 1.5E+07 N/m to keep the maximum coil shift within 0.2 mm, while a 40 mW heat load to the liquid helium. The stresses in the support links beyond allowable limit require adjustment (loosening of support links using adjustment nuts) during cool-down of the coil. Further analysis was also carried out to include the initial coil positioning error in the model and found out its effect on the final position of the coil after cool-down. From this analysis, the limiting alignment requirement of the coil has been found out to be ± 0.2 mm to control the coil-position-error within ± 1 mm, as required to achieve the desired field uniformity.

In case of solenoid magnet, coil shift is not an important parameter for its inherent symmetry in the coil structure, but the interaction between the coil and iron yoke. The K500 superconducting cyclotron at VECC has one horizontal support link shorter in length relative to other two links. This asymmetry in the support system would result in inherent coil shift during cool-down of the coil. Since magnetic force depends on the coil shift, high stresses in support links may lead to its failure. Detail analysis is therefore required even for the solenoid magnets. The analytical model, developed for dipole magnet, was modified for solenoid magnet and detail analysis has been performed. The model was used to analyze the behavior of the coil and support system together under thermal and magnetic loads.

The analytically calculated support forces have been compared with the FEM (ANSYS) results as well as measured data. It has been seen that the analytical model well predicts the support forces, even better than the ANSYS results. The reason for this may be due to the numerical errors in the meshing of such large coil and support system. The coil shift is not measurable in the VECC superconducting cyclotron, and so, the comparison of calculated coil shift with measured data was not possible. The results of coil shift were therefore compared with the FEM (ANSYS) results and found to agree well. The estimation of coil shift in the superconducting magnet is an important requirement, as the magnetic force on the coil increases with coil shift and can lead to failure of the support, if not the coil is carefully centered.

The estimation of coil shift requires to model the effect of magnetic force on the support system. This model includes the Lorentz force on the coil as well as the interaction force between the coil and iron yoke. The support links forces were measured during energization of the magnet as a function of the current in the coil. The results of the analysis and the measured data were plotted and compared with the experimental data. It shows good agreement with the assumed value of coil shift. The coil was moved in steps for its centering, keeping in mind that all the forces will decrease with current for a well-centered coil due to Lorentz force dilation of coil-bobbin assembly. The support forces data during coil centering were stored and were compared with the analytical model results. It has been seen that they agree well with each other. However, the amount of movements tried to be given to the coil by adjusting the support link nuts were not the same as predicted by the analytical model result. The movement given to the support links is modified by the additional stiffness offered by the plumbing lines of the bobbin. Hence, the calculated shift of the coil is not the same as the adjustment of support links done.

During the study of support system for superconducting magnets, it has been found that low thermal conducting, and high strength materials are being used, like CFRP, G10, Ti, Ti alloys, and so on. It has also been found that Ti and its alloys are suitable candidate materials for low-temperature applications. Ti-6Al-4V alloy has found good applications in Aerospace and show very high tensile strength and sufficient elongation at low temperature. The thermal conductivity of Ti-6Al-4V is also lower than stainless steel in the temperature range of 300 K to 20 K. Usability of this alloy in accelerator application has not been studied earlier. The post-irradiation characterization of the Ti and Ti-6Al-4V was thus taken up, using different model-based approaches, to find their suitability in application to support structure in superconducting magnets from the point of irradiation damage. Various levels of proton irradiation were done on pure Ti and Ti-6Al-4V samples. X-ray Diffraction (XRD) data was obtained, and the microstructure was characterized by XRD Line Profile analysis. Microhardness of the unirradiated and irradiated samples has also been investigated. This study showed that Ti-6Al-4V could be considered as a radiation resistant alloy up to an irradiation dose of 4 x 10^{21} p/m^2, which is much higher than that is expected by the support structures of an accelerator during its lifetime (considering 20 years of a lifetime).

5.2 The scope of future work

The design of the support system for superconducting magnets involves detail FEM analysis. The analytical model developed here has the potential to become a tool for the design of support system for superconducting magnets before carrying out detail analysis. In future, design charts may be developed for various kinds of magnets for finding out the initial design parameters for the support system, considering all the thermal and magnetic loads. A computer program may also be tailored to help in designing different support systems for superconducting magnets.

The work can be further extended to ease the coil centering of superconducting magnets by measurement of support forces. The method is expected to help in avoidance of large magnetic forces on the coil as also reducing the efforts during coil centering.

References

[1] R. Ouboter, "Superconductivity: Discoveries during the early years of low temperature research at Leiden 1908-1914," *IEEE Transactions on Magnetics,* vol. 23, no. 2, pp. 355-370, 1987.

[2] L. Rossi and L. Bottura, "Superconducting Magnets for Particle Accelerators," *Reviews of Accelerator Science and Technology,* vol. 5, pp. 51-89, 2012.

[3] T. Whitlatch, C. Curtis, E. Daly, C. Graves, J. Henry, K. Matsumoto, P. Mutton, J. Pitts, J. Preble, W. Sachleben, W. Schneider, S. Slachtouski and M. Wiseman, "Shipping and alignment for the SNS cryomodule," in *Particle Accelerator Conference, 2001. PAC 2001*, Chicago, IL, USA, 2001.

[4] S. Q. Yang, M. A. Green, W. W. Lau, R. S. Senanayake, B. Strauss and H. Witte, "The Cold Mass Support System and the Helium Cooling System for the MICE Focusing Solenoid," *IEEE Transactions on Applied Superconductivity,* vol. 17, no. 2, 2007.

[5] A. Buenaventura, C. Hauviller and B. Skoczen, "MECHANICAL BEHAVIOUR OF THE LHC CRYODIPOLES," in *Seventh European Particle Accelerator Conference (EPAC 2000)*, Vienna, Austria, 2000.

[6] L. Li, W. Qiuliang, Z. Baozhi, Z. Ni, C. Cui and H. Wang, "Theoretical model of a cold mass strap suspension system for superconducting magnets," *IEEE Trans. Appl. Supercond.,* vol. 21, no. 6, pp. 3640-3645, 2011.

[7] R. Niemann, J. Gonczy, K. Mataya and P. Smelser, "An epoxy fiberglass tension member support for superconducting magnet," vol. 24, pp. 283-289, 1978.

[8] K. Zhang, Z. Zhu, H. Z. Ling Zhao, M. Wang, G. Zhang, W. Yao, F. Ning, Z. Wang and X. Zhang, "Cold Mass Support Structure Design of MRI Superconducting Magnet Developed by IHEP," vol. 25, no. 2, 2015.

[9] K. Zhang, Z. Zhu, G. Zhang, Z. Dai and L. Zhao, "Investigation of Adopting Ti-15V-3Cr-3Sn-3Al Tie Rod to Support the Cold Mass of Superconducting Magnet with Strict Alignment Requirements," *IEEE Transactions on Applied Superconductivity,* vol. 26, no. 2, 2016.

[10] M. A. Green and R. O. Bangerter, "Magnet and Cryostat Configurations for a Multi-port Quadrupole Array," *IEEE Transactions of Applied Superconductivity,* vol. 11, no. 1, 2001.

[11] B. Shaughnessy, P. Eccleston, K. Fereday, S. Canfer, H. Nørgaard-Nielsen and N. Jessen, "Thermal conductivity measurement below 40K of the CFRP tubes for the Mid-Infrared Instrument mounting struts," *Cryogenics 47 (2007) 348–352,* vol. 47, pp. 348-352, 2007.

[12] O. P. Anashkin, "Mechanical tests of ATLAS barrel toroid tie rods," *Cryogenics,* vol. 45, no. 7, pp. 469-472, 2005.

[13] B. Levesy, H. Gerwig, F. Kircher and M. Reytie, "Design and Test of the Titanium Alloy Tie Rods for the CMS Coil Suspension System," *IEEE TRANSACTIONS ON APPLIED SUPERCONDUCTIVITY,* vol. 12, no. 1, 2002.

[14] L. Wang, "Design and analysis of a self-centered cold mass support for the

MICE coupling magnet," *IEEE Trans. Appl. Supercond.,* vol. 21, no. 3, pp. 2259-2262, 2011.

[15] M. Lopes, G. Ambrosio, K. E. Badgley, F. Bradascio, J. Brandt, D. Evbota, A. Hocker, M. Lamm, V. Lombardo, J. Miller, T. H. Nicol, R. Kutschke, C. Vellidis, B. Wands and E. Wenk, "Mu2e Transport Solenoid Cold-Mass Alignment," *IEEE TRANSACTIONS ON APPLIED SUPERCONDUCTIVITY,* vol. 27, no. 4, 2017.

[16] R. K. Bhandari, M. Ahammed, P. Bhattacharya, S. Bhattacharya, S. Chattopadhyay, T. K. hattacharya, U. Bhunia, J. Chaudhuri, M. K. Dey, A. Dutta, A. DuttaGupta, C. Mallik, B. Mandal, B. Manna, C. Nandi, G. Pal, S. Roy, S. Saha and P. R. Sarma, "Superconducting magnets for Energy Buncher at FAIR," *Current Science,* vol. 100, no. 5, 2011.

[17] D. Morrissey, "A new high-resolution separator for high-intensity secondary beams," *Nuclear Instruments and Methods in Physics Research Section B,* vol. 126, p. 316, 1997.

[18] H. Sato, T. Kubo, Y. Yano, K. Kusaka, J. Ohnishi, K. Yoneda, Y. Shimizu, T. Motobayashi, H. Otsu, T. Isobe, T. Kobayashi, K. Sekiguchi, T. Nakamura, Y. Kondo, Y. Togano, T. Murakami, T. Tsuchihashi, T. Orikasa and K. Maeta, "Superconducting Dipole Magnet for SAMURAI Spectrometer," *IEEE TRANSACTIONS ON APPLIED SUPERCONDUCTIVITY,* vol. 23, no. 3, 2013.

[19] V. Buchanan, D. Kassner and I. Polk, "THE ISABELLE MAGNET SUPPORT AND ADJUSTMENT SYSTEM," *IEEE Transactions on Nuclear Science,* Vols. NS-26, no. 3, 1979.

[20] G. Jones and E. Christensen, "MAGNET COLD MASS HIGH LOAD SUPPORTS THERMAL RESPONSE AND PERFORMANCE DESIGN CORRELATION," *IEEE TRANSACTIONS ON MAGNETICS,* Vols. MAG-21, no. 2, 1985.

[21] R. Hopkins and D.A.Payne, "Optimized support systems for spaceborne dewars," vol. 27, pp. 209-216, 1987.

[22] T. Hirokawa, "Design of support strap with advanced composite for cryogenic application," *Cryogenics,* vol. 31, no. 4, pp. 288-291, 1991.

[23] P. Kittel, "Comparison of Dewar supports for space applications," *Cryogenics,* vol. 33, no. 4, pp. 429-434, 1993.

[24] R. M. Reimers, R. C. Wolgast and R. M. Yamamoto, "MAGNET COIL SYSTEM FOR A SUPERCONDUCTING SPECTROMETER (HISS)," *IEEE Transactions on Nuclear Science,* Vols. NS-30, no. 4, 1983.

[25] A. Lipski, T. Nicol and R. Richardson, "Alternative design concept for the SSC dipole magnet cryogenic support post," in *Supercollider 3*, 1991.

[26] V.M.Bedakihale, V. Jain, K. S. Babu, K.J.Thomas, B.R.Doshi and Y. Saxena, "Support Structure of Toroidal Field Magnet System of SST-1," *IEEE,* 1998.

[27] F. Alessandria, F. Broggi and M. Todero, "Mechanical Characterization of the Tie Rods for the ATLAS B0 Model Coil," *IEEE TRANSACTIONS ON APPLIED SUPERCONDUCTIVITY,* vol. 12, no. 1, 2002.

[28] C. Mayri, "Suspension System of the Barrel Toroid Cold Mass," *IEEE TRANSACTIONS ON APPLIED SUPERCONDUCTIVITY,* vol. 16, no. 2, 2006.

[29] J. Ohnishi, H. Okuno and M. Nakamura, "Support Structure of Cold-Mass for Superconducting Ring Cyclotron and Electromagnetic Force Measurements With Strain Gauges," *IEEE TRANSACTIONS ON APPLIED SUPERCONDUCTIVITY,* vol. 24, no. 3, 2014.

[30] B. Wang, "Design, development and fabrication for BESIII superconducting muon detector solenoid," *IEEE Trans. Appl. Supercond.,* vol. 15, no. 2, pp. 1263-1266, 2005.

[31] G.Biallas, J. J.E.Finks, B.P.Strauss, M. .Kuchnir, W.B.Hanson, E.Kneip, H. Hinterberger, D.DeWitt and R.Powers, "THE SUPPORT AND CRYOSTAT SYSTEM FOR DOUBLER MAGNETS," *IEEE TRANSACTIONS ON MAGNETICS,* Vols. MAG-15, no. 1, 1979.

[32] S. Q. Yang and M. A. Green, "The Mechanical and Thermal Design for the MICE Focusing Solenoid Magnet System," *IEEE Transactions on Applied Superconductivity,* vol. 15, no. 2, p. 1259, 2005.

[33] S. Q. Yang, M. A. Green, W. W. Lau, R. S. Senanayake, B. Strauss and H. Witte, "The Cold Mass Support System and the Helium Cooling System for the MICE Focusing Solenoi," *LBNL-61384, published in IEEE Transactions on Applied Superconductivity,* vol. 17, no. 2, 2006.

[34] H. Wu, X. Liu, L. Wang, S. Li, X. Guo, H. Pan, F. Xu and M. Green, "Structural design and analysis for a double-band cold mass support of MICE coupling magnet," *Advances in Cryogenic Engineering (MICE Note 277),* vol. 55, 2010.

[35] K. Zhang, Z. Zhu, L. Zhao, Z. Hou, M. Wang, G. Zhang, W. Yao, F. Ning, Z. Wang and X. Zhang, "Cold Mass Support Structure Design of MRI Superconducting Magnet Developed by IHEP," *IEEE Transactions on Applied Superconductivity,* vol. 25, no. 2, 2015.

[36] M. A. Green, J. Ottarson, G. Bollen, S. S. Chouhan, J. DeKamp, D. Lawton, C. Magsig, D. Morrissey, S. Schwarz and A. F. Zeller, "Cold Mass Support System for the MSU," *IEEE TRANSACTIONS ON APPLIED SUPERCONDUCTIVITY, VOL. 26, NO. 4, JUNE 2016,* vol. 26, no. 4, 2016.

[37] E. Marquardt, J. Le and R. Radebaugh, "Cryogenic Material Properties Database," in *11th International Cryocooler Conference*, Keystone, Co, USA, 2000.

[38] A. Zeller, J. DeKamp, J. Wagner and D. Capelli, "Construction and testing of superferric dipoles for the A1900 Fragment Separator," *IEEE transactions on Applied Superconductivity,* vol. 04, 2001.

[39] P. Sarma, A. D. Gupta, C. Nandi, S. Chattopadhyay and G. Pal, "Unconventional Purcell filter in superferric magnets in the Facility for Antiproton and Ion Research,”," *Nuclear Instruments and Methods in Physics Research Section A,* vol. 729, pp. 718-724, 2013.

[40] D. Morrissey, B. Sherrill, M. Steiner, A. Stolz and I. Wiedenhoever, "Commissioning the A1900 projectile fragment separator," *Nuclear*

Instruments and Methods in Physics Research Section B, vol. 204, pp. 97-113, 2003.

[41] T. Kubo, "In-flight RI beam separator BigRIPS at RIKEN and elsewhere in Japan," *Nuclear Instruments and Methods in Physics Research Section B,* vol. 204, pp. 97-113, 2003.

[42] S. Schwarz, G. Bollen, M. Brodeur, S. Chouhan, J. DeKamp, A. Gehring, N. Joshi, C. Magsig, D. Morrissey and R. Ringle, "The NSCL cyclotron gas stopper – Under construction," *Nuclear Instruments and Methods in Physics Research Section B,* vol. 317, pp. 463-467, 2013.

[43] J. Colvin, R. Huson, W. MacKay, Y. Miao, S. Pissanetzky, R. Rocha, G. Shotzman, Y. Xiang and J. Ziegler, "Superferric correction magnets for the SSC," *IEEE Transactions on Magnetics ,* vol. 27, no. 2, 1991.

[44] S. Timoshenko and D. Young, Elements of Strength of Materials, East-West Press Private Limited, 2010.

[45] "ANSYS," ANSYS, Inc., [Online]. Available: www.ansys.com.

[46] "ANSYS Inc. User's Guide".

[47] "Cryogenic Technologies Group, Material properties Index," [Online]. Available: https://www.nist.gov.

[48] J. Holman, Heat Transfer, 2 ed., New Delhi: Tata McGrow-Hill Publishing Company Ltd., 2001.

[49] M. K. Dey, A. D. Gupta, J. Debnath, J. Pradhan, A. Dutta, S. Saha, M. Ahammed, P.Bhattacharjee, U. Bhunia, Z. Naser, S. Paul, J. Chaudhuri, C. Mallik and R.K.Bhandari, "Coil Centering of the Kolkata Superconducting Cyclotron Magnet," in *Proceedings of Eighteenth International Conference on Cyclotrons and Their Applications*, 2007.

[50] L. Wang, H. Wu, L. K. Li, M. A. Green, C. S. Liu, S. Y. Li, X. K. Liu, L. X. Jia and S. P. Virostek, "The Helium Cooling System and Cold Mass Support System for the MICE Coupling Solenoi," *IEEE TRANSACTIONS ON APPLIED SUPERCONDUCTIVITY,* vol. 18, no. 2, 2008.

[51] R. Bhandari and B. Sinha, "SUPERCONDUCTING CYCLOTRON PROJECT AT VECC," in *The first Asian Particle Accelerator Conference (APAC98)*, Tsukuba, Japan, 1998.

[52] B. Sinha and R. K.Bhandari, "STATUS OF THE SUPERCONDUCTING CYCLOTRON PROJECT AT VECC," in *Proceedings of APAC 2004*, Gyeongju, Korea, 2004.

[53] S. Saha, A. D. Gupta and Manir Ahammed, "Cryostat Suspension System Analysis During Cool-Down and its Validation,," *Journal of The Institution of Engineers (India): Series C.*

[54] E. Marquardt, J. Le and R. Radebaugh, "Cryogenic Material Properties Data base," in *11th International Cryocooler Conference*, New York, 2000.

[55] "Standard Internally Gaged Studs (Steel Alloy), ST Series," STRAINSERT, [Online]. Available: https://www.strainsert.com/products/internally-gaged-studs/.

[56] J. W. Kim, "EFFECTS OF VERTICAL MISALIGNMENT OF

SUPERCONDUCTING COILS IN CYCLOTRONS," in *Cyclotrons and Their Applications 2001, Sixteenth International Conference*, 2001.

[57] Y. Iwasa, Case Studies in Superconducting Magnets: Design and Operational Issues, New York and London: Plenum Press, 1994.

[58] J. Pradhan, "Studies of magnetic forces during the energisation of K-500 superconducting magnet," in *IPAC*, 2005.

[59] H. Blosser, D. Lawston and P. Miller, "Studies of stress in the superconducting coil support system," Annual Report, NSCL, MSU,, 1977-1978.

[60] "Sources of Magnetic Fields - MIT, Chapter 9, 9.8 Appendix -1: Magnetic field off the Symmetry Axis of Current Loop," [Online]. Available: http://web.mit.edu/viz/EM/visualizations/coursenotes/modules/guide09.pdf.

[61] C. L. Dym, "Extending Castigliano's Theorems," *Journal of Applied Mechanics,* vol. 77, 2010.

[62] S. Subimal, "Superconducting magnet for K-500 cyclotron at VECC, Kolkata," *Cryogenics,* vol. 49, pp. 235-242, 2009.

[63] P. Miller, D. Johnson, H. Blosser, H. L. D. Poe and G. Stork, "Centering of the Coil and the Cryostat in the K500 Magnet," MSU Report, 1978-1979.

[64] F. Kircher, O. Delferriere, L. Scola, M. Lemke, A. Petrov, K. Sinram, U. Schneekloth, R. Stromhagen, B. Curé and K. Elsener, 340 ILC Technical Design Report: vol. 4, Part V ILD Bibliography LC-DET-2012-081, 2013.

[65] A. FASSÒ, M. SILARI and L. ULRICI, in *Ninth International Conference on Radiation Shielding*, Tsukuba, Japan, 1999.

[66] N. Simas, "Radiation Effects in Material Microstructure (Brookhaven National Laboratory, Upton, New York, USA)," in *ISOPE-2007*, Lisbon, Portugal, 2007.

[67] E. Tabachnikova, V. Bengus, A. Podolskiy, S. Smirnov, K. Csach, J. Miskuf, L. Saitova, I. Semenova and R. Valiev, *Rev. Adv. Mater. Sci.,* vol. 18, pp. 604-607, 2008.

[68] M. Reytier, F. Kircher and B. Levesy, in *Advances in cryogenic engineering: proceedings of the international cryogenic materials conference – ICMC, AIP conference proceedings*, 2002.

[69] M. Barucci, L. Lolli, L. Risegari and G. Ventura, *Cryogenics,* vol. 48, pp. 166-168, 2008.

[70] "Ti alloys," in *ASM Handbook, Vol. 2*, 1979.

[71] G. Kopirin, in *Titanium Alloys in Mechanical Engineering (in Russian)*, Mashinostroenie, Leningrad, 1977.

[72] I. Gorinin, V. Vinokurov, O. Kojevnikov, V. Rybin and I. Yarmolovitch, *Plasma Dev. Operat., 4, 235, 1996.,* vol. 4, p. 235, 1996.

[73] D. Duncan, R. Puigh and E. Operman, *J. Nucl. Mater.,* Vols. 103-104, p. 919, 1981.

[74] A. Kohyama, K. Asaho and N. Igata, *J. Nucl. Mater. 141–143 (1986) 987,* Vols. 141-143, p. 987, 1986.

[75] R. Hasse and C. Hartley, "Irradiation effects on 17–7 PH stainless steel, A-201 carbon steel and Ti–6Al–4V alloy," Report NACA-TM-X-2678, November

1972.
[76] R. Nygren, *J. Nucl. Mater.,* Vols. 85-86, p. 861, 1979.
[77] S. Sastry, "Comparison of titanium alloy Ti–6Al–4V and 5621S microstructure after EBR-II irradiation," ADIP Quarterly Report DOE/ET-0058/ 1, 1978.
[78] A. Amroussia, M. Avilov, C. J. Boehlert, F. Durantel, C. Grygiel, W. Mittig, I. Monnet and Frederique Pellemoine, *Nucl. Instrum. Methods Phys. Res. Sect. B,* vol. 365, pp. 515-521, 2015.
[79] R. Jones and L. Charlot, *J. Nucl. Mater.,* vol. 91, pp. 329-335, 1980.
[80] L. K. Mansur, "Survey of Radiation Effects in Titanium Alloys ORNL/TM2008/137,," Materials Science & Technology Division, for the U. S. Department of Energy under contract DE-AC05-00OR22725, August 28, 2008.
[81] B. Warren, X-Ray Diffraction, Dover Publications, 1990.
[82] B. Warren and B. Averbach, *J. Appl. Phys.,* vol. 21, p. 595, 1950.
[83] T. Ungar, H. Mughrabi, D. Rönnpagel and M. Wilkens, *Acta Metall.,* vol. 32, p. 333, 1984.
[84] I. Groma, T. Ungár and M. Wilkens, *J. Appl. Crystallogr.,* vol. 21, p. 47, 1988.
[85] T. Ungár, I. Groma and M. Wilkens, *J. Appl. Crystallogr. 22 (1989) 26.,* vol. 22, p. 26, 1989.
[86] R. Snyde and J. Fiala, Defects Microstruct. Anal. by Diffraction,, H. Bunge, Ed., New York: Int. Union Crystallogr, Oxford University Press Inc,, 1999.
[87] P. Mukherjee, A. Sarkar, P. Barat, S. Bandyopadhyay, P. Sen and S. Chattopadhyay, *Acta Mater.,* vol. 52, pp. 5687-5696, 2004.
[88] P. Mukherjee, A. Sarkar, M. Bhattacharya, N. Gayathri and P. Barat, *J. Nucl. Mater.,* vol. 395, p. 37, 2009.
[89] P. Mukherjee, P. Barat, A. Sarkar, M. Bhattacharya and N. Gayathri, M. P. Hemsworth, Ed., Nova Science Publishers Inc, 2011, p. 133.
[90] P. Mukherjee, N. Gayathri, P. Chowdhury and M. Mitra, *J. Nucl. Mater.,* vol. 434, pp. 24-30, 2103.
[91] S. Neogy, P. Mukherjee, A. Srivastava, M. Singh, N. Gayathri, A. Sinha, D. Srivastava and G.K. Dey, *J. Alloy. Compd.,* vol. 640, pp. 175-182, 2015.
[92] J. Langford, Defects Microstruct. Anal. by Diffraction, J. F. H. B. R.L. Snyde, Ed., New York: Oxford University Press Inc., 1999, p. 10.
[93] H. Hulst and J. Reesinck, *Astrophys. J,* vol. 106, pp. 121-127, 1947.
[94] J. Langford, *J. Appl. Cryst.,* vol. 11, pp. 10-14, 1978.
[95] G. Williamson and W. Hall, *Acta Metall.,* vol. 1, p. 22, 1953.
[96] R.A. Young (Ed.), The Rietveld Method,, Oxford University Press, 1993.
[97] P. S. L. Lutterotti, *J. Appl. Crystallogr.,* vol. 23, p. 246, 1990.
[98] W. Dollase, *J. Appl. Cryst.,* vol. 19, p. 267, 1986.
[99] J. Ziegler, "SRIM – The Stopping and Range of Ions in Matter, 15th ed.,," 2015. [Online]. Available: http://www.srim.org/.
[100] "XRD Components - Detectors," Bruker, [Online]. Available:

https://www.bruker.com/products/x-ray-diffraction-and-elemental-analysis/x-ray-diffraction/components/xrd-components/detectors.html.

[101] "Hardness Tester," CRASE SRL, [Online]. Available: http://www.crase.com/eng/prodotti/generale/durometri.html.

[102] J. Zubicza, X-ray Line Profile Analysis in Materials Science, IGI Global, 2014.

[103] M. Krivoglaz, Theory of X-ray and Thermal Neutron Scattering by Real Crystals,, NY Plenum press, 1969.

[104] M. Wilkens, Fundamental Aspects of Dislocation Theory 2, J. Simmons, R. d. Wit and R. Bullough, Eds., Washington, DC,: National bureau of Standards, 1970, p. 1195–1221.

[105] A. Borbely and I. Groma, *Appl. Phys. Letts.,* vol. 79, p. 1772, 2001.

[106] D. Balzar and H. Ledbetter, *J. Appl. Cryst. 26 (1993) 97–103.,* vol. 26, pp. 97-103, 1993.

[107] I. Groma, *Phys. Rev. B,* vol. 57, p. 7535, 1998.

[108] Y. Prabhu, K. V. Rao, V. S. S. Kumar and B. S. Kumari, *Int. J. Eng. Adv. Technol. (IJEAT),* vol. 2, p. 268, 2013.

[109] L. Lutterotti, S. Matthies, H.-R. Wenk, A. Schultz and J. R. Jr., *J Appl. Phys.,* vol. 81, p. 594, 1997.

[110] H. Wenk, L. Lutterotti and S. Vogel, *Nucl. Instrum. Methods A,* vol. 515, p. 575, 2003.

[111] G. Was, Fundamentals of Radiation Materials Science,, New York: Srinfer-Berlin Heidelberg, 2007.

[112] D. Plumton, G. Kulcinsk and R. Dodd, *J. Nucl. Mater.,* Vols. 264-274, p. 144, 1987.

[113] P. Wilkes and G. Kulcinski, *J. Nucl. Mater.,* vol. 78, pp. 427-430, 1978.

[114] S. Agarwal, G. Ayrault, D. Potter, A. Taylor and F. N. Jr., *J. Nucl. Mater.,* Vols. 85-86, pp. 653-657, 1979.

[115] S. Sastry, J. O'Neal and J. Davis, in *Titanium '80: Proceedings of the Fourth International Conference on Titanium*, Kyoto, Japan, 1980.

[116] D. Peterson, in *Effects of Radiation on Materials: Eleventh Conference*, 1982.

[117] A. Leineweber, *J. Appl. Crystallogr. 40 (2007) 362–370.,* vol. 40, pp. 362-370, 2007.

[118] A. Leineweber, *Z. Kristallogr.,* vol. 224, pp. 432-445, 2009.

[119] N. Poondla, T. Srivatsan, A. Patnaik and M. Petraroli, *J. Alloy. Compd.,* vol. 486, pp. 162-167, 2009.

Annexure-1: Calculation of system stiffness for dipole magnet

The system stiffness, for any force applied on support #1, is calculated using Castigliano's theorem applying on the model shown below. Since the system is statically indeterminate, support #1 is removed to make it a determinate system. A force F_1 is applied in the support #1 and the reactions at support #2 and #3 is calculated using the force balance equations:

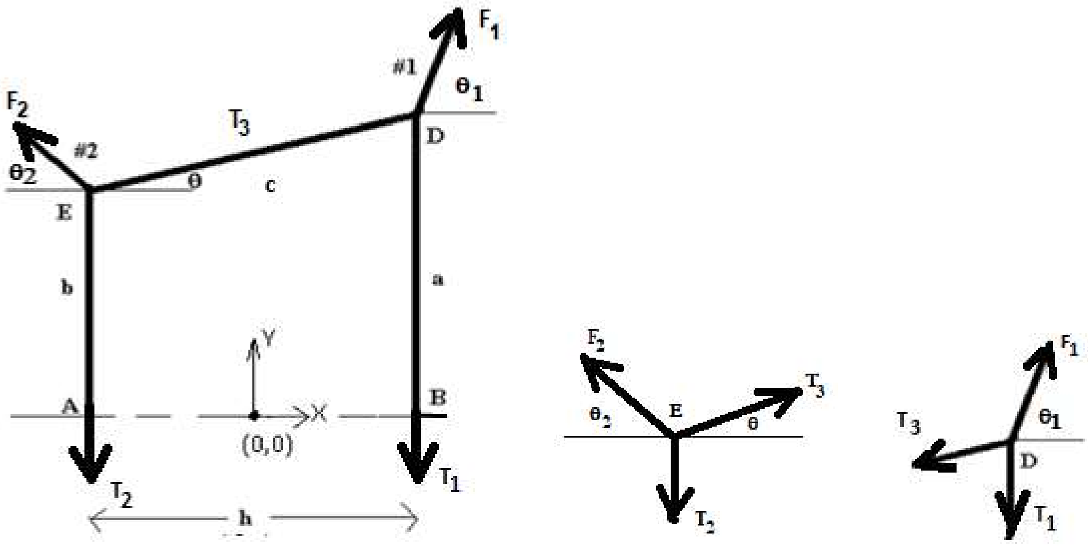

Free body diagram of the support system along with the coil. ¼ symmetry model is taken. F_1 is the applied force, F_2, T_1, T_2 &T_3 are reaction forces.

$$F_2 \cos\theta_2 - T_3 \cos\theta = 0 \quad \dots(1)$$

$$F_1 \cos\theta_1 - T_3 \cos\theta = 0 \quad \dots(2)$$

$$F_2 \sin\theta_2 + T_3 \sin\theta - T_2 = 0 \quad \dots(3)$$

$$F_1 \sin\theta_1 - T_1 - T_3 \sin\theta = 0 \quad \dots(4)$$

Solving equations (1), (2), (3) and (4), we get F_2, T_1, T_2, and T_3 as a function of F_1.

The complementary potential energy of the system is calculated by:

$$U^* = F_2^2 \frac{L_s}{2A_sE_s} + T_1^2 \frac{a}{2A_bE_b} + T_2^2 \frac{b}{2A_bE_b} + T_3^2 \frac{c}{2A_bE_b}$$

where a, b and c are the length of arms of the coil, a = AE, b = BD and c = DE.

Deformation due to force F_1 is given by

$$\frac{\partial U^*}{\partial F_1} = \Delta_1$$

Stiffness offered by the system against the force F_1 is given by:

$$\frac{1}{K_1} = \frac{\Delta_1}{F_1} = \left[\frac{\mathrm{L_s}}{\mathrm{A_s\ E_s}}\right]\left[\frac{\cos\theta_1}{\cos\theta_2}\right]^2$$

$$+ \left[\frac{1}{\mathrm{A_b\ E_b}}\right]\Bigg[\mathrm{a}\,.\left(\sin\theta_1 - \cos\theta_1\,.\frac{\sin\theta}{\cos\theta}\right)^2$$

$$+ \mathrm{b}.\left(\cos\theta_1.\frac{\sin\theta_2}{\cos\theta_2} + \cos\theta_1\,.\frac{\sin\theta}{\cos\theta}\right)^2 + \mathrm{c}.\left(\frac{\cos\theta_1}{\cos\theta}\right)^2\Bigg]$$

And, the analogous way, we can calculate,

$$\frac{1}{K_2} = \frac{\Delta_2}{F_2} = \left[\frac{L_s}{A_s\ E_s}\right]\left[\frac{\cos\theta_2}{cos\theta_1}\right]^2$$

$$+ \left[\frac{1}{A_b\ E_b}\right]\Bigg[a\left(cos\theta_2\,\frac{sin\theta_1}{cos\theta_1} + cos\theta_2\,\frac{sin\theta}{cos\theta}\right)^2$$

$$+ b\left(sin\theta_2 - cos\theta_2\,\frac{sin\theta}{cos\theta}\right)^2 + c\left(\frac{\cos\theta_2}{cos\theta_1}\right)^2\Bigg]$$

Annexure-2: Calculation of stiffness of bobbin against thermal load

The system stiffness, for any force applied on support #1, is calculated using Castigliano's theorem. Because of the three-fold symmetry of the system, the following model is used for it.

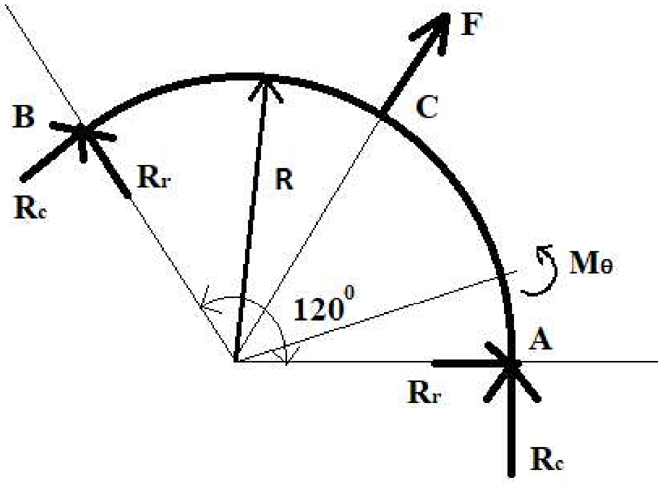

For the above, we can write:

$\sum F_x = 0$ i.e. $R_r - R_r \cos\left(\frac{\pi}{3}\right) + R_c \sin\left(\frac{\pi}{3}\right) + F cos\left(\frac{\pi}{3}\right) = 0 \quad ...(1)$

$M_\theta = R_c\, R\left(1 - \cos\left(\frac{\pi}{3}\right)\right) + R_r\, R sin\left(\frac{\pi}{3}\right)$, where R is the radius of the bobbin.

$$\frac{\partial M_\theta}{\partial R_c} = R\left[\left(1 - \cos\left(\frac{\pi}{3}\right)\right) + \frac{\partial R_r}{\partial R_c} R\sin\left(\frac{\pi}{3}\right)\right] = 0 \quad ...(2)$$

Since there is no movement of point A,

$$\frac{\partial M_\theta}{\partial R_c} = 0$$

Calculate R_c & R_r from equation (1) & (2) as a function of F.

$$U^* = 2\int_0^{\pi/3} \frac{{M_\theta}^2\, R\, d\theta}{2\, E\, I_b} \qquad \ldots(3)$$

Deformation towards the force F is given by:

$\Delta = \partial U^*/\partial F$

Therefore, $K_b = \Delta/F = \frac{2\,R_b^3}{E\,I_b}\int_0^{\frac{\pi}{3}}[R_c(1-\cos\theta) + R_r \sin\theta]^2\, d\theta$

Where,

$$R_c = \frac{\int_0^{\frac{\pi}{3}} (1 - \cos\theta - \sqrt{3}\ \sin\theta)\ \sin\theta\ d\theta}{\int_0^{\frac{\pi}{3}} (1 - \cos\theta - \sqrt{3}\ \sin\theta)^2}$$

$R_r = 1\text{-}\sqrt{3}\ R_c$

Annexure-3: Calculation of dilation of the bobbin under the Lorentz force

The model shown below is used to calculate the dilation of the bobbin is Figure (a). The axis convention is shown in Figure (b), while θ is the azimuthal direction of the coil.

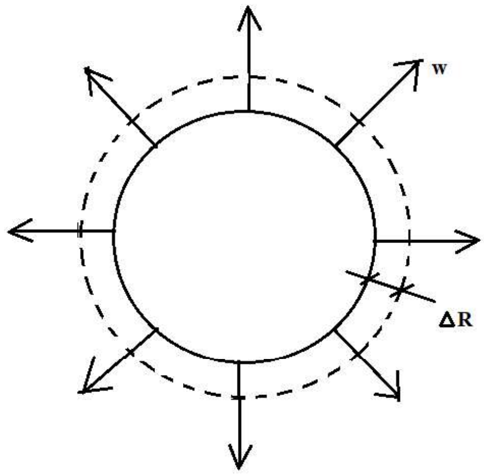

(a)

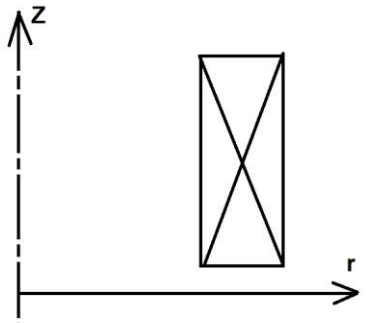

(b)

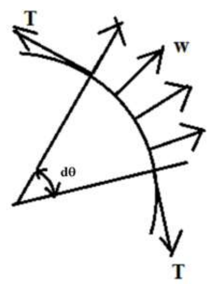

(c)

The radial force on the unit circumference of the coil can be calculated by summing the radial forces ($J_\theta \times B_z$) over the cross-section of the coil and results in the following equation:

$$w = J_\theta \int_r \int_z B_z \, dr \, dz$$

From figure (c), we can write the force balance equation as follows:

$$2\,T\,sin\left(\frac{d\theta}{2}\right) = w\,R\,d\theta$$

For, θ is small, $\sin\left(\frac{d\theta}{2}\right) = \frac{d\theta}{2}$

So, $T = w\,R$,

Stress, σ = T/A = E ε

So, Strain,

$$\varepsilon = \frac{\Delta R}{R} = \frac{T}{A\,E} = \frac{wR}{AE}$$

Therefore, $\Delta R = \frac{w\,R^2}{A\,E}$ … (1)

Annexure-4: Equilibrium equations for coil under magnetic force

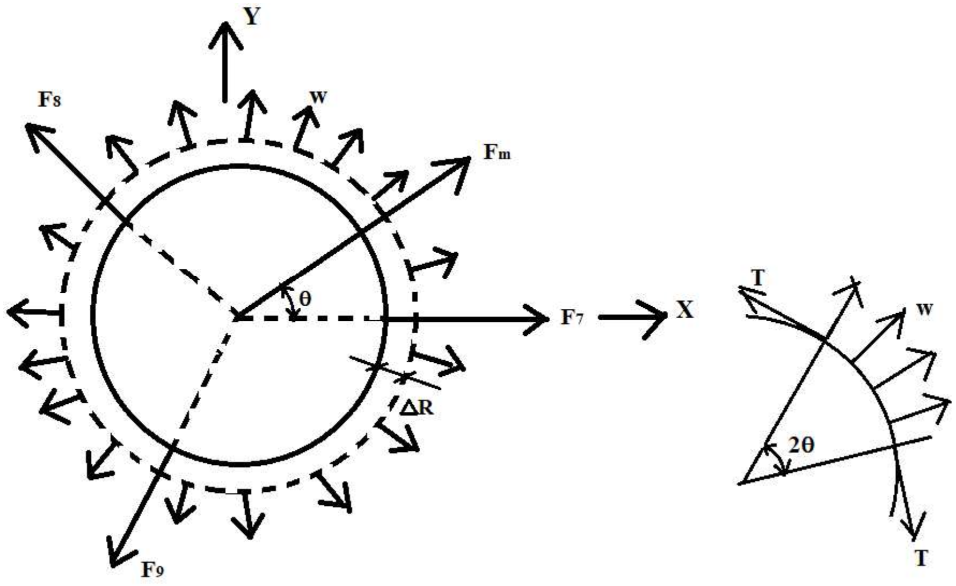

(a) (b)

(a) Model for calculating support force due to magnetic force, (b) Part section of the bobbin under the Lorentz force

Force balance equations for X and Y-directions are as below:

$\Sigma Fx = 0$; so,

$$F_7 - F_8 \cos\left(\frac{\pi}{3}\right) - F_9 \cos\left(\frac{\pi}{3}\right) + F_m \cos(\theta) = 0 \quad \dots (1)$$

$\Sigma F_y = 0$; so,

$$F_8 \sin\left(\frac{\pi}{3}\right) - F_9 \sin\left(\frac{\pi}{3}\right) + F_m \sin(\theta) = 0 \quad \dots (2)$$

The complementary potential energy of the system, $U^* = \frac{{F_7}^2}{2\,K_7} + \frac{{F_8}^2}{2\,K_8} + \frac{{F_9}^2}{2\,K_9} + \frac{T^2 .2\pi R}{2AE}$

$$\frac{\partial U^*}{\partial F_7} = \frac{F_7}{K_7} + \frac{F_8}{K_8} \cdot \frac{\partial F_8}{\partial F_7} + \frac{F_9}{K_9} \cdot \frac{\partial F_9}{\partial F_7} + \frac{3.T.\frac{2\pi}{3}.R}{AE} . \frac{\partial T}{\partial F_7} \quad \dots .(3)$$

Again, for the equilibrium of any 1/3rd section of the coil, the following equation is true,

$$w\left(\frac{2\pi R}{3}\right) = F_7$$

i.e.

$$\frac{2\pi T}{3} = F_7$$

Therefore,

$$\frac{\partial T}{\partial F_7} = \frac{3}{2\pi}$$

…. (4)

It is assumed that the forces F_7, F_8, F_9 at 120° are in equilibrium, it must be that:

$F_7 = F_8 = F_9$

Hence,

$\frac{\partial F_8}{\partial F_7} = 1$ and $\frac{\partial F_9}{\partial F_7} = 1$ …. (5)

Since $T = wR$, … (6)

Hence, from equation (3), (4), (5) and (6) we can write:

$$\frac{\partial U}{\partial F_7} = \frac{F_7}{K_7} + \frac{F_8}{K_8} \cdot \frac{\partial F_8}{\partial F_7} + \frac{F_9}{K_9} \cdot \frac{\partial F_9}{\partial F_7} + \frac{3.w.R^2}{AE}$$

Again, since, $\frac{wR^2}{AE} = \Delta R$, and $\frac{\partial \mathrm{U}}{\partial \mathrm{F}_7} = 0$

Also, from Annexure-3 equation (1), $\frac{wR^2}{\mathrm{A}E} = \Delta R$

$0 = \frac{F_7}{K_7} + \frac{F_8}{K_8} + \frac{F_9}{K_9} + 3.\Delta R$ …. (7)

It may be noted that the value of $\frac{\partial \mathrm{U}^*}{\partial \mathrm{F}_7}$ is zero for the minimization of the complementary potential energy [61].

Annexure-5: Analysis of a three parallel spring system

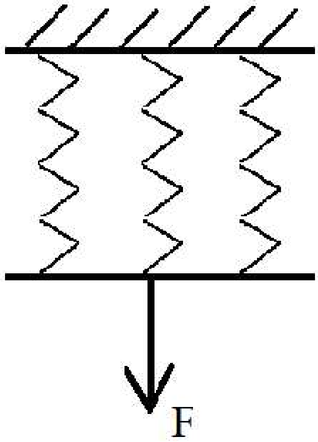

Method (1) by solving the force and deformation balance equations
We can write: $\sum F = 0$, so

$$F = F_1 + F_2 + F_3$$

… (1)

Now, deformation of the springs is equal and is assumed as δ, so

$$\delta = \frac{F_1}{K_1} = \frac{F_2}{K_2} = \frac{F_3}{K_3}$$

(2) & (3)

Therefore, equation (1), (2) and (3) can be solved to obtain F_1, F_2, F_3.

Method (2) minimization of the complementary potential energy of the system

The complementary strain energy of the system can be written as:

$$U^* = \frac{F_1^2}{2K_1} + \frac{F_2^2}{2K_2} + \frac{(F - F_1 - F_2)^2}{2K_3}$$

Now, for minimizing U, we can write as:

$$\frac{\partial U^*}{\partial F_1} = 0$$

i.e. $\left(\frac{K_3}{K_1} + 1\right) F_1 + F_2 = F$

… (4)

Again, we can also write:

$$\frac{\partial U^*}{\partial F_2} = 0$$

$$\text{i.e. } F_1 + \left(\frac{K_3}{K_2} + 1\right) F_2 = F \qquad \ldots (5)$$

We can therefore solve equations (4) and (5) to get the value of F_1, F_2 and $F_3 = F - F_1 - F_2$.

(3) by minimizing the deformation of the system:

This method is described by Clive L. Dym [61] in his paper. The ratio of distribution of the forces in springs have been taken as r_1, r_2 and $1 - r_1 - r_2$.

The complimentary strain energy of the system can, therefore, be written as:

$$U = \frac{r_1^2 F^2}{2K_1} + \frac{r_2^2 F^2}{2K_2} + \frac{(1 - r_1 - r_2)^2 F^2}{2K_3}$$

Deformation δ can be written as:

$$\delta = \frac{\partial U}{\partial r_1} = \left[\frac{r_1^2}{K_1} + \frac{r_2^2}{K_2} + \frac{r_3^2}{K_3}\right] F$$

Now, for minimization of deformation, we can write:

$$\frac{\partial \delta}{\partial r_1} = 0$$

$$\text{i.e. } \left(\frac{K_3}{K_1} + 1\right) r_1 + r_2 = 1 \qquad \ldots (6)$$

We can again write:

$$\frac{\partial \delta}{\partial r_2} = 0$$

$$\text{i.e. } r_1 + \left(\frac{K_3}{K_2} + 1\right) r_2 = 1 \qquad \ldots (7)$$

Equations (6) and (7) can be solved and found out r_1, r_2 and $r_3 = 1 - r_1 - r_2$.

Force is then calculated as: $F_1 = r_1 F$, $F_2 = r_2 F$ and $F_3 = r_3 F$.